Fabrication & Analysis of a-Si:H/μc-Si:H Tandem Solar Cell on Flexible Aluminium Substrates

Govind Padmakumar

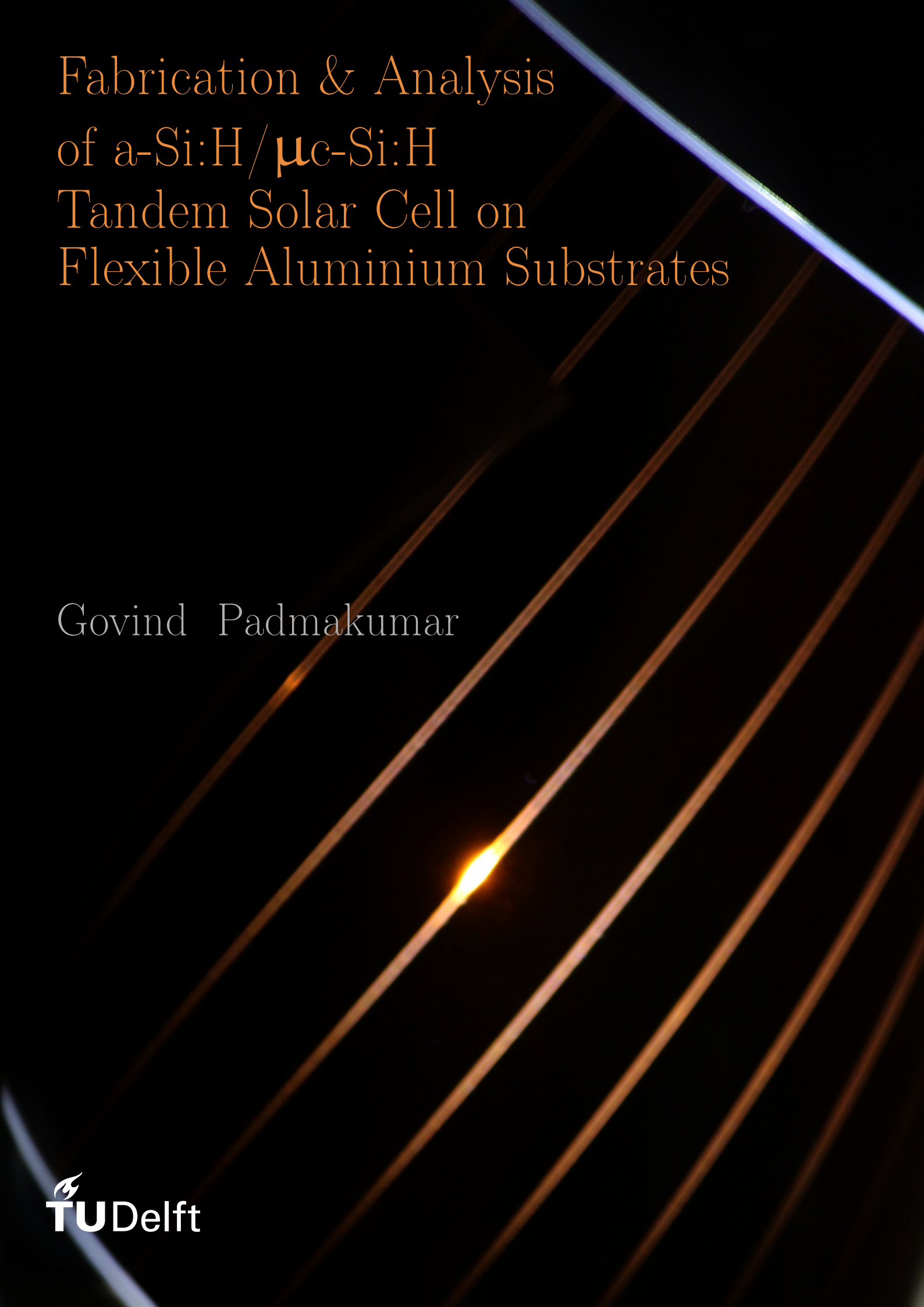

TU Delft

Fabrication and Analysis of a-Si:H/μc-Si:H Tandem Solar Cell on Flexible Al Substrates

A FlamingoPV project

by

Govind Padmakumar

to obtain the degree of

Master of Science
in Sustainable Energy Technology

at the Delft University of Technology,
to be defended publicly on Monday August 30, 2021 at 03:00 PM.

Student number:	5007984	
Thesis committee:	Prof. dr. A. H. M Smets,	TU Delft, ESE- PVMD, Supervisor
	Dr. ir. R. Santbergen,	TU Delft, ESE- PVMD, Assistant Professor
	Dr. ir. B. Gholizad,	TU Delft, ESE- DCES, Assistant Professor
	Dr. G. Limodio,	TU Delft, ESE- PVMD, Supervisor
	Dr. C. .M Ruiz Tobon,	TU Delft, ESE- PVMD

Cover image : Sunshine Through the Interconnection of a Flexible Solar Module.
(Photo by Author)

TU Delft PVMD Delft University of Technology HyET Solar Flexible light weight solar modules EKL Else Kooi Laboratory

" Nature's imagination far surpasses our own,
as we have seen from the other theories,
which are subtle and deep."

RICHARD P. FEYNMAN
The Character of Physical Law

Abstract

Our world is on its way to re-engineer the daily life based on renewable clean energy. And this multilateral attempt to combat environmental and climate change has its focus perfectly poised to embrace the infinite energy source - solar energy as an alternative. Thin-film photovoltaic technology also referred to as second-generation technology is an alternative family of solar technology in the market which holds rich market prospects such as potential advantages of cost-effective substrates, low transportation-installation costs due to its lightweight property and the possibility of direct integration in building materials. HyET solar is focusing its production on Roll-to-Roll manufacturing of thin films. The utilisation of R2R production with efficient deposition in substrate configuration, and the serial interconnections of cells done during production can bring down the cost of production and contribute to manufacturing flexible solar cells on polymers. The thin-film solar energy technology is looking at a possible re-entry to the market with these advantages.

Integrating the micromorph configuration into this technology is challenging. To start we have taken two base models and tried to fabricate tandem samples on the aluminium substrate. These substrates are temporary foils with modulated surface texturing implemented on them for better light utilization. The initial lab-scale samples yielded less than 35% of the total. The lab-scale samples showed highly defective $\mu c - Si : H$ subcells. An investigation on the layers used in the samples was conducted and it suggested conclusively that the $\mu c - SiO_x$ n layers with low activation energies were the main reason for the very low shunt resistances in the cells.

The power of optoelectronic modelling is taken advantage of to improve the performances is done. This study resulted in a model of optimised efficiency of 12.2%. A study on doping of the tunnelling recombination junctions suggested that with poorly doped layers, the objective of TRJ to facilitate tunnelling recombination at the junction is not satisfied and ultimately affect the cell behaviour forming a reverse biased n-p junction. The use of a highly reflective intermediate reflective layer for the tandems is detrimental to the bottom cell performance. But at the same time, a reflective behaviour in the TRJ p-doped layer, when using a p-doped $\mu c - SiO_x$ layer fabricated at 3.2 sccm CO2 flow rate, the reflection is moderate and can be proved beneficial resulting in a thinner top cell. The possibility of modelling to predict the performance, out of standard test conditions suggests a drop in the open-circuit voltage of our cell by 4.9mV per Kelvin increase and a fall in the efficiency by 0.058% per Kelvin.

In summary, the tandem flexible solar cells once overcome the challenges in fabrications it can facilitate cheap, high-efficiency modules. The simulations on this same structure point towards several potential spaces for the micromorph configuration for improvement within itself and certainly a bright future ahead of us powered by thin-film flexible tandem solar cells.

Acknowledgement

It was not an easy decision for me to break free and take up a new challenge to do a masters in TU Delft. And at the end of these two years, it is a dream come true moment for me. I thank the PVMD group for the opportunity they provided me to pursue my study in the vicinity of cutting-edge resources and brilliant researchers to collaborate with.

First of all, I would like to thank Prof.Dr. Arno Smets for the great teacher and motivator you are. It has been an honour to work with you and I see your question "Have you done anything to save humanity today?" as a very relevant one and I am sure that my answers will be affirmative on every single day of my life.

I express my sincere gratitude for Boss Dr. Gian Luca Limodio, you are the best supervisor any student can wish for. Thank you for guiding me throughout the project and giving me the freedom and space to experiment. Thanks to Dr. Carlos Ruiz Tobon for all your help on modelling throughout the project. I express my sincere gratitude to Dr. Davide Bartesaghi and Dr. Edward Hamers for letting me be a part of HyET Solar. I am extremely thankful for the guidance you gave me and the critical examination of my work.

My deepest appreciation goes to Thierry de Vrijer for his valuable suggestions throughout the project, Dr Rudi Santbergen for his help with GenPro4 simulations , Martijn Tijssen and Stefaan Heirman for taking the time to help me with the measurements and equipments.

I would also like to thank my country and the taxpayers of India for the resources they provided me with, to embed the prerequisites which made me capable of doing this Masters program successfully.

In addition, I would like to mention Fadhil and Aditya for sharing valuable knowledge important thesis work. Also my fellow office-mates - Aswathy and Anirudh for the cherished moments during the nine months duration of our thesis.

A special mention to the special people in my life - Aravind, Liju, Radhika, Malavika and Ganesh for being a part of my journey. This would never have been easy without you. Also, I thank Devika for the support you have given me and to A.George for the crazy discussions and conversations which kept me going.

And above all I thank my parents and my sister, words are not enough to express the love you shower over me. I value the efforts that you people have put to see me happy and pursue my dreams. I dedicate the work to you.

Govind Padmakumar
Delft, August 2021

Contents

List of Figures

List of Tables

1 Introduction

The term industrial revolution is a succinct catchphrase to describe a historical period of technological advancements and innovations. This movement began in Britain in the 18^{th} century and has continued all the way till today. In the late 1900s, after more than a century and a half of industrialization, along with fossil fuel use and clear-felling of forests, the world recognized the need for a multilateral action to combat environmental and climate change. The carbon-rich fuels burnt over this period has drastically increased the amount of Carbon dioxide, the major contributor to the greenhouse effect[1] in the earth's atmosphere. The following temperature rise has touched approximately 1°C by 2017 compared to pre-industrial times[2] which urgently demand a widespread shift to cleaner forms of energy.

Paris climate conference (COP21) in December 2015 clearly embarked long term goal to limit the global average temperature increase to 2°C, while pursuing the efforts to limit it below 1.5°C [3]. The agreement puts forward the obligations of developed countries to support developing countries attain climate-resilient clean energy futures. Variety of renewable energy forms needed to be explored and exploited to achieve this target agreed upon by the Paris convention. Solar and wind power are the front-runners in this carbon neutrality target of 2050: figure 1.2.

The estimated contribution by modern renewable energy in the total final energy consumption(TFEC) has only reached 11.2% in 2019 compared to 8.7% in 2009. The fossil fuels still make a dominant contribution of 80.2% which barely changed over a decade (refer to figure1.1) due to economic and efficiency reasons. 250 GW of new renewable energy were added to global total energy production by end of 2020 which raised the total renewable global production to 2588GW [4]. Solar installations solely contributed 57% of this value. Extensive funding and researches in the field of solar technology together with economic policies are fueling the growth of photovoltaic(PV) industries.

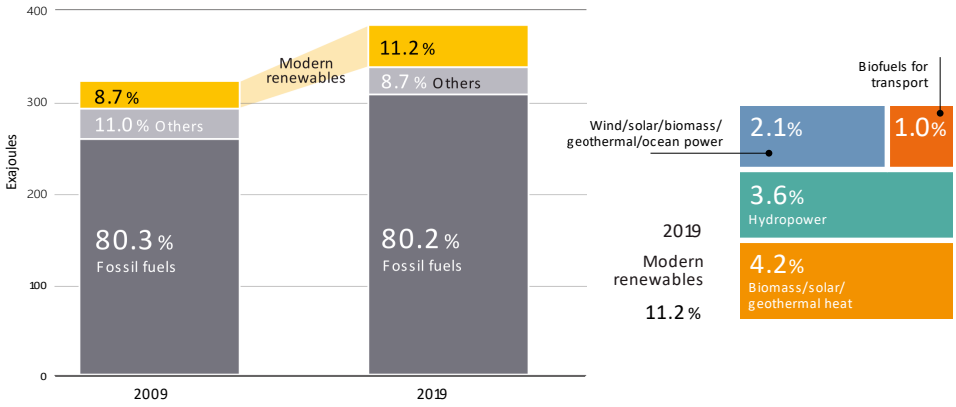

Figure 1.1: Estimated Renewable Share of Total Final Energy Consumption, 2009 and 2019 [4]

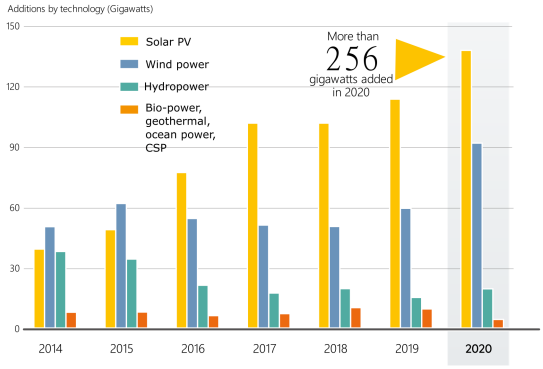

Figure 1.2: Annual Additions of Renewable Power Capacity, by Technology and Total, 2014-2020 [4]

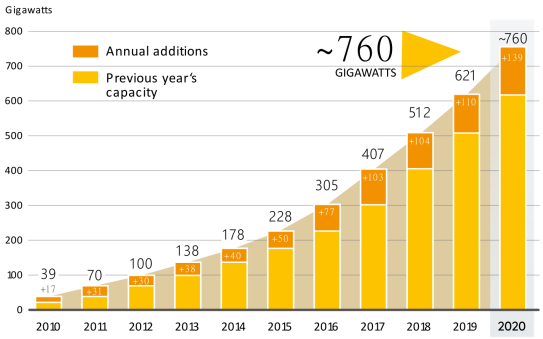

Figure 1.3: Solar PV Global Capacity and Annual Additions, 2010-2020 [4]

1.1. Thin-film photovoltaics

Solar energy holds a pivotal role in the current transition phase in the energy sector. An addition of 139GW in 2020 made the total production to 760 GW marking a consistent growth of the sector over the previous decade as seen in the figure1.3. These numbers include different forms of installations from floating PV panels to building-integrated photovoltaics (BIPV) and a wide range of technologies from crystalline silicon to thin-film solar cells.

Thin-film photovoltaic technology also referred to as *second-generation* technology is an alternative family of technology in the market. 'Thin film' in contrast to 'thick film' can be defined according to Chopra *et al.* [5] as a material "created *ab initio* by the random nucleation their grotheir processes of individually condensing/reacting atomic/ionic/molecular species on a substrate. The structural, chemical, metallurgical and physical properties of such a material are strongly dependent on a large number of deposition parameters and may also be thickness dependent". This definition gives room for a number of deposition techniques for the production namely, plasma, evaporation methods, sputtering techniques etc. Also the family of cells may vary from a few nanometer to micrometer thickness and clearly be better identified by deposition techniques over the thickness criteria [6]. The final morphology and electrical-optical properties of these cells are very heavily dependent on its production techniques.

Thin-film PV modules overtake the first generation cells in their market prospects such as potential advantages of the possibility of continuous roll-to-roll processing, cost-effective substrates, low transportation-installation costs due to lightweight and the possibility of direct integration in building materials. Despite these favourable properties, thin-film PV is on a decline in the market share for the last few years as reported in 2014 with 8% in contrast to 19% in 2009 [7]. These are a consequence of the decrease in crystalline silicon costs and rising efficiencies of crystalline silicon technologies, while on the contrary thin-film silicon solar cells (TFSC) technology is facing challenges of stable efficiency and complexity of production processes [6]. Yet, with the decreasing trends in market shares, it should be realized that TFSC technologies may not replace the crystalline silicon from the market but shall give a huge edge in the sunbelt countries which exhibit high temperatures and diffused light conditions. And it shall be highlighted that the thin-film photovoltaic modules with better temperature coefficient and ideal power conversion in adverse climatic conditions can out-power crystalline silicon in particular aspects[7].

A possible re-entry to the market for thin-film silicon technologies shall be via the roll-to-roll (R2R) fabrication technique consequently reducing production costs. The utilisation of R2R production with efficient deposition in substrate configuration, and the serial interconnections of cells done during production can bring down the cost of production and contribute to manufacturing flexible solar cells on polymers [8].

1.2. Flamingo PV

Flexible Lightweight Advanced Materials in Next Generation of PV (Flamingo PV) is a joint venture of HyET Solar, a subsidiary company of HyET (High yield Energy Technologies) Group and TU Delft for the production of flexible high-efficiency solar cells. The project is aimed at attaining an efficiency >12% and lifetime

expectations >35% for the product.

Hyet produces lightweight and flexible thin-film silicon solar cells using long Aluminium foil substrates over a roll-to-roll production line[9]. The process is further explained in the section 1.3. This manufacturing process is aimed to result in maximum added value and full quality control during production stages. Thin-film amorphous silicon and microcrystalline silicon cells are encapsulated by water-resistant lightweight flexible polymer, providing an extended lifetime. The final product has a thickness < 0.5mm, and surface density around 0.6 kg/m^2. Thus the production techniques developed by HyET has been able to produce their modules from abundant non-toxic materials at an energy payback time of less than a year[10].

The Flamingo PV project aims to achieve the following goals[11] :

1. Lab-scale flexible a-Si:H/nc-Si:H PV cell (5cm^2) and module (5 x 5 cm^2 with 13% stabilized module efficiency.

2. Roll-to-roll produced modules of 30x30 cm2 of 12% aperture area stabilized efficiency with 80% production yield.

3. Industry standard lifetime (> 80% initial performance) convincingly proven for lifetime > 35 years.

4. Design and cost model for bottom cell PECVD tool with CAPEX < 0.2 €/W_p.

5. Lab-scale flexible a-Si:H/nc-Si:H/nc-Si:H PV cell (5cm^2) and module (5 x 5 cm^2) with 14% stabilized module efficiency.

The combination of these deliverables will result in a PV product that will be competitive with state-of-the-art c-Si modules for large scale power plants and will have the potential to dominate the BIPV market[11]. This thesis is done within the framework of this project to achieve the above deliverables and addresses the questions stated in the following section.

1.3. Roll-to-roll(R2R) processing at HyET solar

HyET Solar uses a roll-to-roll production technique that uses a temporary aluminium substrate and consequently taking away the transparency requirements of the substrate foils. The production method was developed by the Helianthos consortium [12] in 1998, at that time consisting of Akzo Nobel, Delft University, Eindhoven University, Utrecht University and TNO. This procedure uses an aluminium foil that is later etched away in multiple steps to complete the production. The carrier function for this flexible foil is then satisfied by polymer adhered to the solar cells [13]. In this way, this procedure allows superstrate configuration even though the substrate used is not transparent material.

Flexible module manufacturing faces challenges from suitable front contacts which are temperature compatible and cost-effective combined with monolithic series connectivity[13]. As illustrated in the figure 1.4, the roll-to-roll production is done on an aluminium substrate where the transparent conductive oxide (TCO) deposition is the first step and this substrate aluminium foil is removed at the final step. Such an R2R process makes it possible to make very long (up to kilometres) solar cells completely automated[14]. With this production method, HyET embraces the advantages such as low silicon utilisation, low-cost high rate Transparent conducting oxide (TCO), large-area silicon deposition, monolithic series connection [13]. The fabrication steps are demonstrated in schematic form in the image 1.4.

HyET solar (then Helianthos) has also investigated the feasibility of micromorph structure on flexible aluminium substrates in the past [15] and could successfully use the temporary superstrate concept for a-Si:H/µcSi:H tandem solar cells. In this thesis, we are focused on the configurations of flexible lab-scale modules.

1.4. Thesis objectives

The thesis aids to the deliverable 1 of the Flamingo PV project 1.2, i.e., to produce a lab-scale tandem solar cell with amorphous/micro-crystalline silicon of (5 cm^2) area and a stabilized module efficiency of 13%. As a part of reaching this goal, this conducted study takes two paths, namely fabrication and modelling. As an initial step, it is extremely important to fabricate solar cells samples to identify the technical and physical challenges en-route. Lab-scale samples of micromorph tandems are made and characterised in this research. Also, to overtake the bottlenecks in fabrication the potential of optoelectrical models is exploited. The real-world performance study is indispensable for any product and we utilize the model to predict these performances.

The main objectives of this thesis are :

i *Fabricate micromorph tandem solar cells with modulated surface texturing on temporary aluminium substrates:* this includes studying the texturing conformality, texture transfer over the fabrication steps and characterisation of the tandem cells.

ii *Investigate on possible challenges in fabrication and proposals to tackle them:* by fabricating solar cell samples of different specifications, thus obtaining a realistic data set for study and draw conclusions.

iii *Creating an optoelectronic model of the micromorph tandem solar cell and maximise the performance :* Study on the impact of absorber layer thicknesses and tandem recombination junction thickness/doping on tandem solar cell performance.

iv *Study the optical / electrical specifications of TRJ layers and after-effects of their fabrication conditions:* This includes the detailed scrutiny on the activation energy of TRJ layers and utilising TRJ layers for intermediate reflection via. variation of oxygen content.

v *Predict out-of-standard conditions and degradation effect on the micromorph tandem solar cell:* by using calibrated multi-junction models to replicate out of standard condition performance - temperature, red/blue spectral response, and stabilised performance mimicking light soaking experiments.

1.5. Outline of report

This report is a continuous journey through the conducted study aimed at full filling the above objectives.

The chapter 2 introduces the underlying principles in optics, semiconductors and photovoltaic technology. This chapter covers the idea of thin films and modelling, which are the main focus areas of this work.

The chapter 3 lays down the fabrication side of a thin-film solar cell and the techniques used to characterise photovoltaic devices. The chapter also lays down the preliminary challenges faced and potential room for improvements.

The chapter 4 discusses the optoelectronic model of tandem solar cells developed from calibrated models. This chapter introduces the texturing developed for Flamingo PV and encapsulation concepts. Tandem recombination junction and performance outside standard conditions are discussed in this chapter along with a preliminary model for incorporating light soaking into the model.

The chapter 5 concludes the study with suggestions for future works and outlooks from the conducted study.

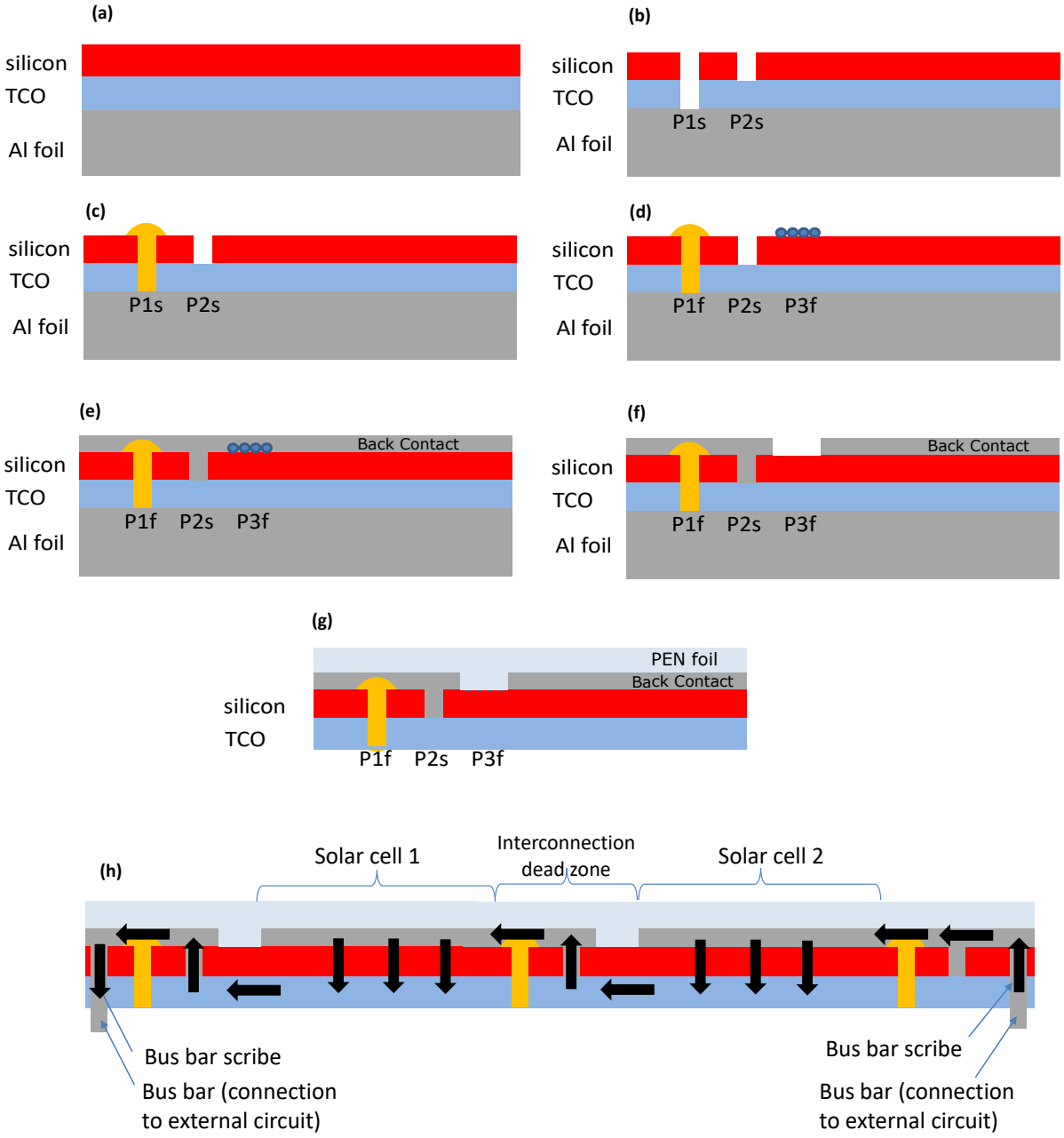

Figure 1.4: The R2R intermediate processes at HyET shown schematically: **(a)** The aluminium foil is deposited with TCO - $SnO_2 : F$ is used as the TCO as it is more resistant to moist and acidic environments compared to ZnO:Al. On top of this, the p-i-n silicon layers are deposited with RF Plasma enhanced chemical vapour deposition (PECVD). **(b)** As the next step, laser scribes are done to define the cell areas denoted as P1S and P2S in the figures. **(c)** The laser scribe P1Sis filled with a non-conductive ink to isolate the active layers. **(d)** A lift-off ink is dispensed in this step which is aimed at cell definition at a later stage and avoiding further scribing. **(e)** Back contact is sputtered using DC magnetron sputtering. Aluminium doped zinc oxide (AZO) and aluminium are sputtered. **(f)** Opening of P3f comprises this step to isolate back contact. **(g)** Wet chemical etching is used to remove the aluminium foil substrate, the plastic foil take over the role of the carrier. A polymer encapsulation is made at the top. **(h)** The final product with bus-bar incorporated and the electrical path.
Images from HyET solar internal documents [16].

2
Fundamentals

The underlying principles required to explain the functioning of a solar cell and fundamental ideas required to understand this thesis are explained in this chapter. This section introduces the very basic ideas on which this work is done, for more detailed ideas and explanations on solar energy conversions and applications, refer to part II and Part III of the book, *Solar Energy: The Physics and Engineering of Photovoltaic Conversion, Technologies and Systems. UIT Cambridge Ltd, 2016*[17].

2.0.1. Light

To explain the different phenomena and concepts of photovoltaics, the *wave-particle* dual nature of light needs to be considered. This is the property that light behaves both as a particle and a wave in itself. The particle or packet of energy of light termed photons was first proposed by M. plank in 1900[18] and later used by A. Einstein ('light quantum' as he called it) to explain the *photoelectric effect* [19] discovered by H. Hertz in 1887 as a byproduct of his experimental demonstration of *electromagnetic theory* of light[20].

Energy and momentum of a photon moving with frequency ν and wavelength λ is given by :

$$E_{ph} = h\nu \qquad and \qquad p_{ph} = \frac{h}{\lambda} \tag{2.1}$$

2.0.2. Semiconductor

Semiconductors are materials having conductivity between those of metals and insulators[18]. Elemental semiconductor entities are found in group IV of the periodic table and the compound semiconductor materials are often formed by combining group III and group V elements. The materials and classification will be discussed in detail in section 2.3

2.0.3. Interaction Of light with semiconductor

When light is incident on a semiconductor a certain fraction of light is reflected and the remaining light transmitted. Some transmitted power is absorbed within the semiconductor to excite electrons from an occupied low energy state to another unoccupied higher energy state. The conduction band E_c is largely unoccupied, and separated from the heavily occupied conduction band by several forbidden energy levels, forming the bandgap. This energy separating the two bands is called band gap energy notated as E_g[21]. Refer to images 2.1 and 2.2.

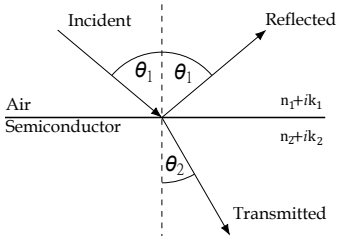

Figure 2.1: Reflected and transmitted fractions of incident light. Inspired by [22]

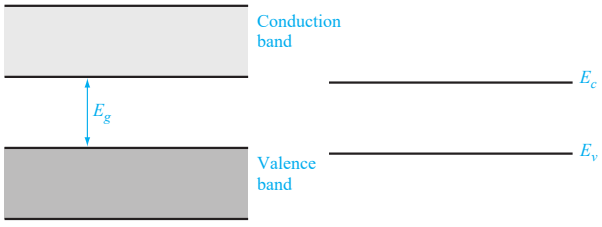

Figure 2.2: The basic energy band diagram and widely used simplified line representation of the energy diagram. Inspired by [18].

2.1. Solar Energy

As mentioned in the section 2.0.3the semiconductor absorbs a part of the light entering the material. So to harvest the Sun's radiation energy, it is very important to study the solar spectrum. The surface temperature of the sun is about 6000K. The characterisation of available sunlight can be done considering the atmosphere it traversed before reaching the earth surface. The spectrum outside the atmosphere is known as AM0, as zero atmospheres is traversed. The irradiance at AM0 is $1361 W/m^2$ [17].

To investigate the performance of solar cells a set of *standard test conditions*(STC) are defined, this is characterized by AM1.5 spectrum and irradiance of $1000 W/m^2$ at a cell temperature of 25°C. The power generated by a photovoltaic (PV) module at STC is expressed in the unit watt peak,W_p.

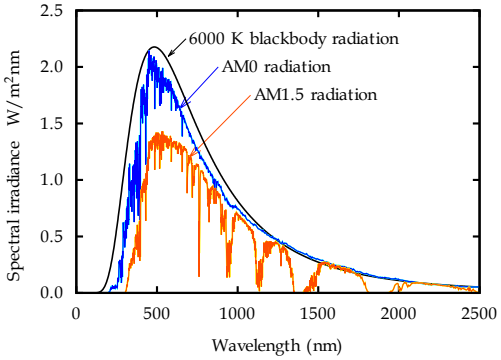

Figure 2.3: Different solar spectra: the black-body spectrum of a black-body at 6000 K, the extraterrestrial AM0 spectrum and the AM1.5 spectrum. Inspired by [17]

2.1.1. Solar energy conversion

The *photovoltaic effect* is the basic working principle of a solar cell. This phenomenon refers to the generation of a potential difference at the junction of two materials when exposed to electromagnetic radiation[17]. This generated electric potential can be further converted to useful work.

The energy conversion in a solar cell has the following three steps in order,

1. **Absorption of photon and generation of charge carriers:** On collision with the material, a photon only gets absorbed, if the energy of the photon can excite an electron from the conduction band to the valance band of the material. This difference between conduction and valance band is called the Bandgap of the material. Once the electron is excited it leaves behind a void, which behaves as if it is positively charged and is called a hole. If the absorbed energy is higher than the bandgap energy the remaining energy is thermalised as shown in the figure 2.4.

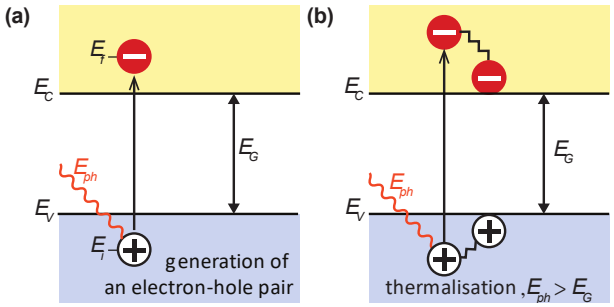

Figure 2.4: (a)Generation of electron hole pair on absorption of photon with energy $E_p h$, (b) Extra energy thermalised when $E_{ph} > E_g$. Inspired by [17]

2. **Separation of photo-generated charge carriers:** The electron-hole pair is generated, has a very high chance to recombine. Therefore they need to be separated using any suitable mechanism to successfully utilize them for useful work.

3. **Collection of charge carriers:** The separated charge carriers need to be collected using metal contacts and channelled to an external circuit to perform electric work. This completes the process of chemical energy conversion to electric energy. The maximum possible attainable efficiency for this is thermodynamically limited to 86% and 67% for concentrated and non-concentrated sunlight[23]. A summary of the process is shown in figure 2.5

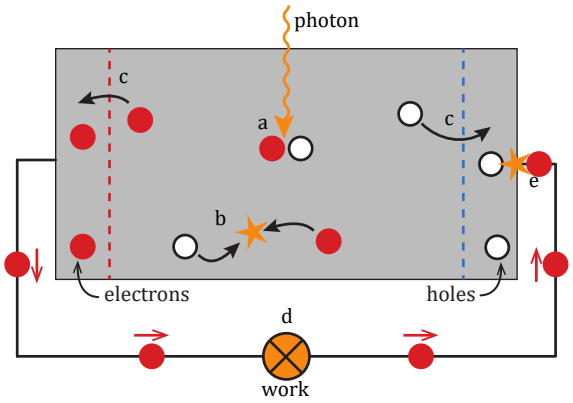

Figure 2.5: (a)absorption of photon to generate electron hole pair. (b)recombination. (c)collection of electron and hole (d)Work done in electric circuit (e)electron recombination with holes. Inspired by[17]

2.2. Optics

As stated in the section 2.0.3, a part of the electromagnetic radiation is reflected at the interface, and the remaining power is transmitted. Also, a fraction of the light photons is absorbed by the semiconductor out of the total transmitted amount. The laws governing these physical phenomena are overviewed in this section.

2.2.1. Optics of absorptive media

The amount of light is transmitted through the medium 2 propagates at an angle θ_2 as shown in the figure 2.1 obeying *Snell's law* $n_1 sin(\theta_1) = n_2 sin(\theta_2)$. The optical properties of an absorptive medium is decided by the complex electric permittivity $\tilde{\epsilon}$ [17].

$$\tilde{\epsilon} = \epsilon' + i\epsilon'' \tag{2.2}$$

And this gives rise to the complex entity called *index of refraction* $\tilde{n}$, defined as $\sqrt{\tilde{\epsilon}}$.

$$\tilde{n} = \sqrt{\tilde{\epsilon}} = n + i\kappa \tag{2.3}$$

The value κ denotes the imaginary part of the refractive index called the *extinction coefficient* [21]. The transmitted light is attenuated as it penetrates through the semiconductor and the absorption rate is proportional to the intensity (photon flux) at a specific wavelength. This is given by the *Lambert-Beer Law* [24].

$$I(z) = I_0 \exp(-\alpha z) \tag{2.4}$$

$$where, \alpha = \frac{4\pi\kappa}{\lambda_0}$$

The coefficient α in the equation 2.4 is the *absorption coefficient* for light propagating in the z-direction. This also gives rise to another entity to quantify the absorptivity at a certain wavelength, the *penetration depth* δ_p defined as the depth at which the intensity decays to $1/e$ of the initial value[17].

$$\delta_p = \frac{1}{\alpha} \tag{2.5}$$

This states the dependence of absorption on frequency, making a very absorptive material at one wavelength nearly transparent at the other. In the case of solar cells to ensure maximum spectral utilisation, the cell needs to be absorptive over the whole range of frequencies.

2.2.2. Reflection at interface

At the interface of two media, a part of the light is reflected at an angle as shown in the figure 2.1, the angle of reflection is found to be equal to the angle of incoming light, θ_1. Solving Maxwell's equation's for an electromagnetic wave at the boundary gives the reflection and transmission amplitudes of respective waves. These coefficients, *Fresnel coefficients* are given by the equations 2.6 and 2.7 for parallel and perpendicular polarization respectively[22].

$$R_{\parallel} = \left| \frac{\tilde{n}_1 \cos(\theta_2) - \tilde{n}_2 \cos(\theta_1)}{\tilde{n}_1 \cos(\theta_2) + \tilde{n}_2 \cos(\theta_1)} \right|^2 \tag{2.6}$$

$$R_{\perp} = \left| \frac{\tilde{n}_1 \cos(\theta_1) - \tilde{n}_2 \cos(\theta_2)}{\tilde{n}_1 \cos(\theta_1) + \tilde{n}_2 \cos(\theta_2)} \right|^2 \tag{2.7}$$

For unpolarized light the reflectivity R, is mean values of the two polarizations, $R = \frac{R_{\parallel}+R_{\perp}}{2}$. The equations are formed assuming the media is non-absorptive on either side of the interface[17].

2.3. Semiconductor physics

Concepts of semiconductor physics are very important to interpret the foundation ideas of solar cells. This section looks into different important terms and principles in solid-state physics. A semiconductor is defined in section 2.0.2 and here, crystalline silicon is taken as an example in the following topics. The band structure of amorphous silicon material is outlined in 2.4.

2.3.1. Density of states

According to Würfel extitet. al [23], the distribution of the electrons over the states must satisfy three conditions :

1. According to the Pauli exclusion principle[25] for particles with non-integral spin, there can never be more than one particle in the same quantum state. This applies for electrons, with a spin $\hbar/2$, in contrast to photons, which have a spin $\hbar$[26].
2. The occupation of the states depends only on the energy.
3. The occupation of the states must lead to a minimum in free energy $F = E - TS$, where T is the temperature and S is the entropy of the state.

When the atoms are in an isolated state, the energy values of electrons are discrete with definite separations. As the atoms are brought very close to each other to only a few Å, they start to interact and split the identical energy levels into as many different values as several atoms in the solid [23] (figure : 2.6). This results in new energy bands which are extremely close to each other so that they appear to form a continuum. These regions are called the bands, shown in figure 2.2.

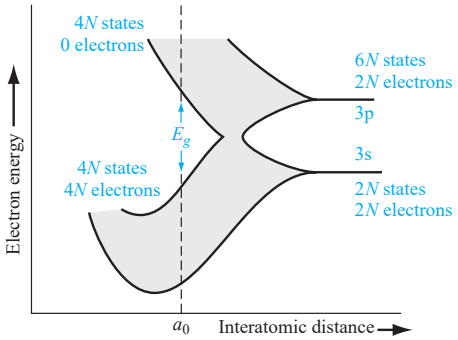

Figure 2.6: The splitting of the 3s and 3p states of silicon into the allowed and forbidden energy bands.Inspired by [18]

Electrical conduction in semiconductors: The silicon crystal at zero Kelvin is shown in figure 2.7 (a). When the temperature increases the electron breaks the covalent bond to leave a positively charged "empty state" called a *hole*. The subsequent images (b) and (c) show a two-dimensional representation of a temperature increase and the conceptual representation of electron and hole occupancy in the bands. The representation is inspired from [18]

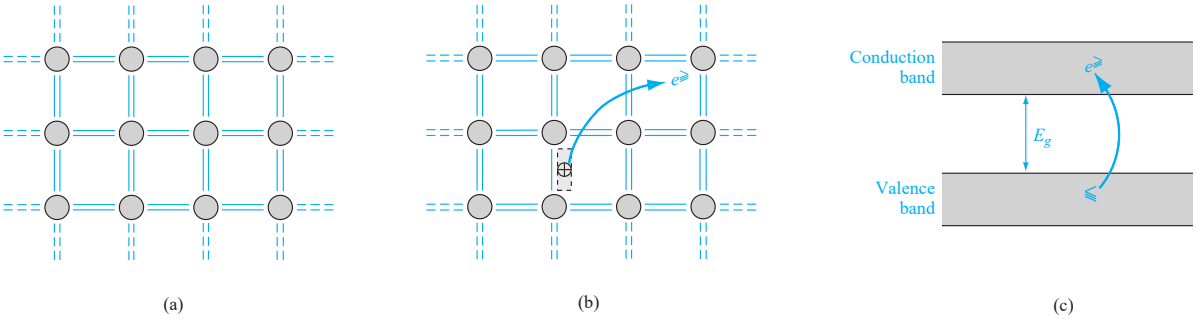

Figure 2.7: (a) 2D crystal structure at 0K. (b) Free electron leaving a positive hole in the lattice. (c) Line diagram of the electron and hole pair created. All images inspired by [18]

2.3.2. Doping

Doping is the process of replacing lattice atoms with an impurity atom of a higher or lower valency. The thermal energy available at 300K is sufficient enough to create an ionised dopant atom [17], adding charge carrying entities (holes or electrons) to the semiconductor. Doping done with a higher valance atoms (termed *Donors*) give rise to an *n-doped* material and a lower valency element atoms (*acceptors*) introduced makes a semiconductor *p-doped*. Insertion of these acceptor or donor atoms into crystalline silicon also introduces new allowed levels into the forbidden gap.

Fermi level: " The Fermi energy is the electrochemical potential of the electrons in a material and in this way it represents the averaged energy of electrons in the material "[17]. For an *intrinsic semiconductor* (zero doping), the Fermi energy level E_{Fi} lies close to the mid-gap value but it is not exactly at half of the energy gap due to varying effective densities of states in the valance and conduction bands[23].

The introduction of p-dopants adds allowed energy levels E_a closer to the valance band and N-dopants add E_d closer to the conduction band. This also results in a shift of the Fermi energy levels towards respective bands as shown in the figure 2.8. At an ideal point of 0K, the Fermi energy is at midway E_c and E_d for the n-type and midway between E_a and E_v for the p-type materials [18]. The concept of Fermi level is significant in analysing semiconductor junctions and devices, at equilibrium state the Fermi level is constant throughout a system [18].

In a p type semiconductor the Fermi level is $E_{Fp} = E_V + kT \ln \frac{N_V}{N_A}$, where N_V and N_A are the values of valance band concentration and acceptor concentration respectively. For an n type material the Fermi level is given as, $E_{Fn} = E_C - kT \ln \frac{N_C}{N_D}$, where N_D is the value of donor concentration and N_C is the conduction band concentration value in intrinsic state.

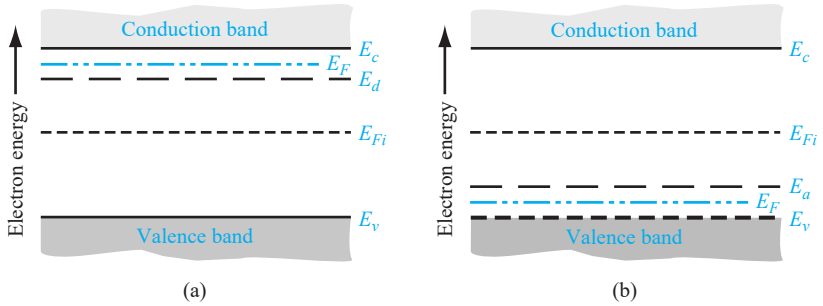

Figure 2.8: New allowed levels and Fermi levels of (a) n-type, (b) p-type semiconductors at 0K. Inspired by [18]

Semiconductor junctions: The image 2.9 (a) shows a p-n junction, which is a single crystal doped with donor doped on one side and the other side doped with acceptor atoms. Figure 2.9 (c) shows the forces that take part in the formation of a p-n junction. The gradient in hole and electrons concentration for each side results in the diffusion across the *metallurgical junction*. This causes the region close to the metallurgical junction to become electrically charged and to become depleted of mobile charge carriers. This region is

called the space-charge region of the depletion region.

This electrically charged region develop an electric field opposite to the direction of diffusion of electrons (from n to p) and holes (from p to n), this direction of the resultant electric field is depicted in figure 2.9 (c).

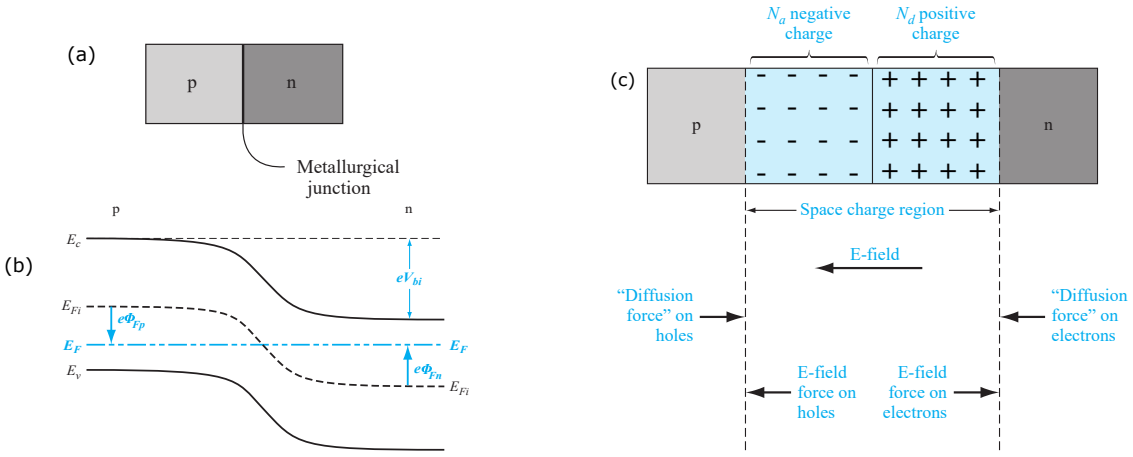

Figure 2.9: (a) a single crystal doped by acceptor and donor atoms forming a p-n junction. (b) Energy band diagram of a p-n junction in equilibrium. (c) The forces resulting in the motion of charge carriers across the metallurgical junction. Inspired by [18]

2.3.3. Direct and indirect bandgap

In a three dimensional space, the distance between atoms vary and also and as a result, the electrons encounter different potential patterns in different directions[18]. The significance of these variations is described in this section.

Direct Bandgap: For a direct bandgap semiconductor, the highest energy level of the valance band is vertically aligned with the lowest energy level of the conduction band [17]. With the two bands aligned the transition from valance energy level to conduction band can happen with the absorption of photon γ with energy value hv. The direct bandgap and transition are depicted in two dimensions in figure 2.10 (a).

Indirect Bandgap: In the case of indirect bandgap materials, the wave vector orientation of the highest valance band energy and lowest conduction band energy is not exact and is mismatched by a momentum value. In such cases, the photons with energy well above the forbidden gap are required for the direct transition of an electron from valance to conduction band [21]. For Lower energy photons, it is possible to excite an electron with a momentum change [17]. Every transition obeys the energy conservation and momentum conservation laws. As given in the equation 2.1, the value of momentum in a photon is very less (h/λ). The change in momentum imparted by a photon is not adequate to facilitate the transition and the excitation is only possible with the help of a three-step process including, the annihilation of a *phonon*. A phonon Γ can be seen as a quantum of "fundamental particle" of lattice vibration. Due to the large mass of the atoms, phonons with small energies, have a large momentum [23]. This kind of transition is represented in two dimensions in 2.10 (b).

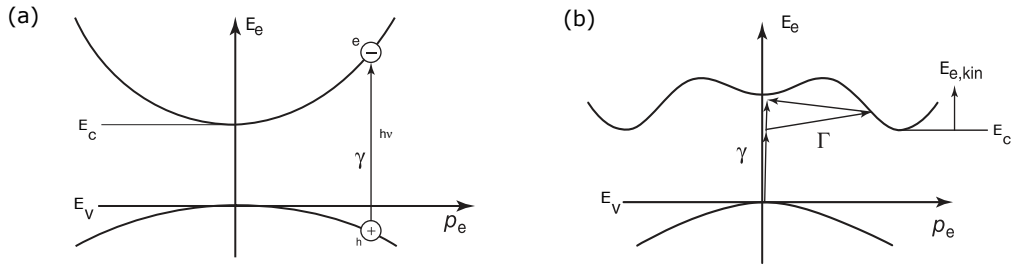

Figure 2.10: (a) Transition in direct band gap absorbing photon γ energy, (b) transition in indirect band gap absorbing photon γ and phonon Γ. Inspired by [23]

.

2.4. Band structure of hydrogenated amorphous silicon (a:Si:H)

Amorphous materials are materials with lattice disorder i.e., the materials lack long-range order with no periodic repetition. This difference is shown in 2.11 (a) and (b). The absence of long-range order in such materials essentially results in free bonds of silicon atoms leading to *"dangling bonds"*. The hydrogen passivation method strictly reduces the dangling bonds from $10^{25} - 10^{26}$ to $10^{21} - 10^{22}$. Hydrogen passivation of dangling bonds can be seen in figure 2.11 (b).

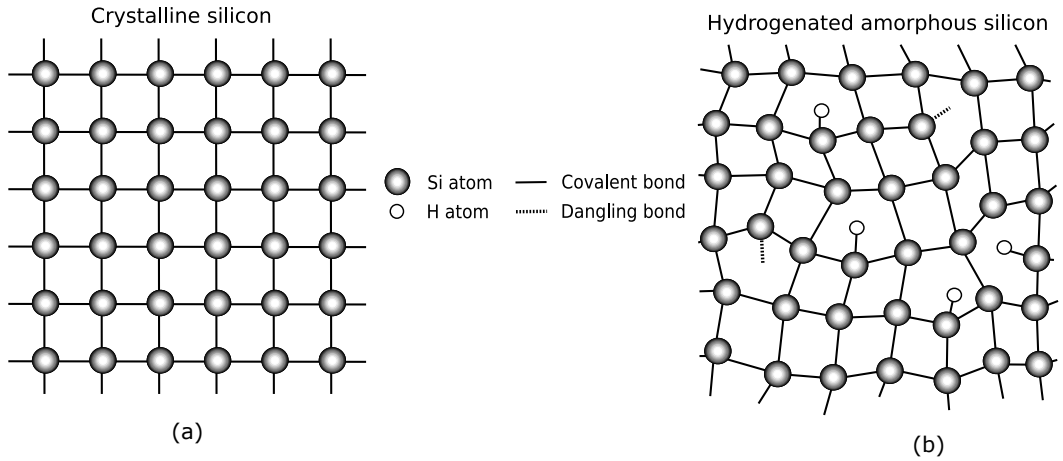

Figure 2.11: Schematic drawing of the lattice of (a) crystalline silicon; (b) hydrogenated amorphous silicon. Inspired by [23]

.

The local order present in amorphous semiconductors is sufficient to define electronic band states, but the random nature over long ranges influence electron behaviour in valance and conduction band. This random potential fluctuation gives rise to so-called *Anderson localization* [27] causing wave functions on both sides of the band referred to as band tails. Added on to this tails, dangling bonds and lattice vacancies give rise to more localised states, depicted in the picture 2.12. Due to the localized nature of these states, the carrier mobilities are much lower compared to the non localised states. These states have a sharp edge and carriers is assumed to have a free motion through the non-local states. These sharp dividing points are referred to as mobility gap which is the amorphous analogous quantity for bandgap. Ec and Ev are represented as the conduction and valance band edges respectively.

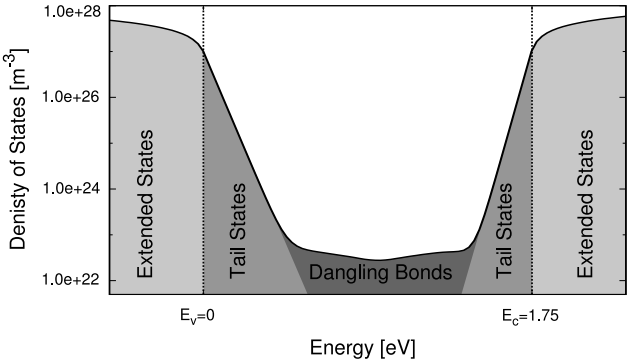

Figure 2.12: Schematic representation of the density of states in a-Si:H.
The shown mobility gap is 1.75eV, a typical value of a-Si:H material.

2.5. Performance of solar cells

The performance of a cell is characterised with the help of Quantum efficiency of the cell and other external solar cell parameters namely, peak power P_{max}, short circuit current density J_{sc}, open circuit voltage V_{oc}, and fill factor FF. These parameters are introduced below and are depicted with help of an illuminated JV curve in the image 2.13.

2.5.1. I-V curve and equivalent circuit model

The electrical performance of a solar cell is often recorded as an I-V curve and the parameters derived from the curve is used as performance indicators. The figure 2.13 represents the exponential relationship given by the *Shockley equation* expressed as:

$$I = I_0 \left[e^{\frac{qV}{nk_B T}} - 1 \right] \tag{2.8}$$

where I is the current, I_0 is the reverse saturation current, q the elementary charge, V the voltage, k_B the Boltzmann constant and T the temperature in kelvin. The ideality factor, n is normally a value between 1 and 2 and is determined by the type of recombination that is dominant in the used material[17].

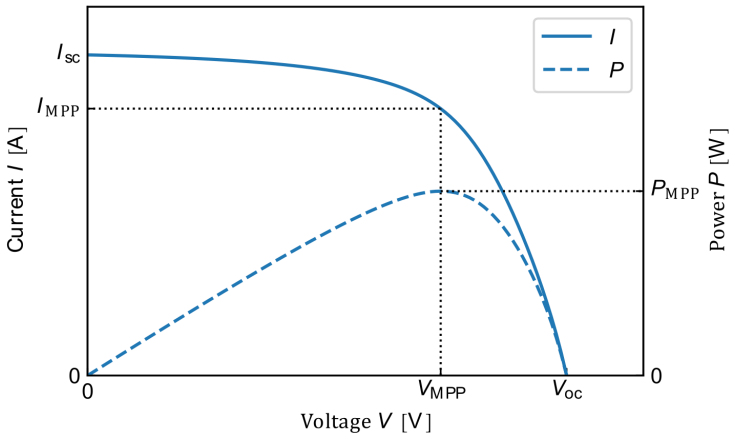

Figure 2.13: J-V characteristics of a p-n junction under illumination.Inspired by [17]

.

Maximum power point, P_{max} : The value of the maximum amount of power at which a solar cell can be operated. The point is characterized by V_{mpp} and J_{mpp} as the corresponding voltage and current density value in the figure 2.13.

Open circuit voltage, V_{oc} : The maximum voltage that a solar cell can deliver is characterised by the open-circuit voltage. The parameter V_{oc} is an indication of recombination in the cell[17].

Short circuit current density, J_{sc} : The maximum amount of current deliverable by a solar cell is given by J_{sc}. The value of J_{sc} is heavily dependent on the photo-generated current of the cell and thereby the optical properties of a cell, like absorption of active layers and reflection[17].

Fill factor, FF : The fill factor of a solar cell is the ratio of the maximum power output of the cell to the product of V_{oc} and J_{sc} [28].

A single diode model of a solar cell has the current source parallel to the diode and is the easy approach to represent a PV cell, relating its final output and current generated in the cell[29]. This is given in the diagram 2.14. The photogenerated current in the solar cell is represented as the current source, I_{ph}. The inclusion of series resistance (R_s) accounts for the resistances of contact, parallel resistance (R_{sh}) include the alternate current paths inside the cell rising from manufacturing (or deposition) defects [30]. The current-voltage relationship accounting for these resistances gives an implicit relationship given by

$$I = I_{ph} - I_0 \left[e^{\frac{q(V+IR_S)}{nk_B T}} - 1 \right] - \frac{V + IR_s}{R_{sh}} \tag{2.9}$$

This relation gives the I, V combinations at which the solar cell can operate with a power delivered represented as P, given by-product of I and V at the point.

The conversion efficiency of a solar cell, η representing the fraction of electrical energy generated to input energy is given by the equation 2.10, assuming the standard irradiance of AM1.5 spectrum, 1000 W/m^2 and temperature of 25°C.

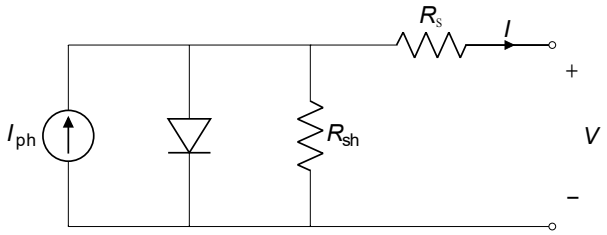

Figure 2.14: Equivalent circuit model of a solar cell. Inspired by [17]

$$\eta = \frac{V_{MPP} I_{MPP}}{P_{in}} = \frac{V_{oc} I_{sc} FF}{P_{in}} \tag{2.10}$$

Ohmic Contact
The metal-semiconductor junction with very negligible resistance, and no voltage drop resulting in zero effect on the device performance. The contact is ideally improved directly with an increase in doping level of the semiconductor when *quantum tunnelling* will dominate the transport mechanism over *thermionic emission* [18].

2.5.2. External quantum efficiency (EQE :

The parameter EQE marks the fraction of amount of collected electron - hole pair generated to the number of photons of the incident light. EQE of a cell at a particular wavelength λ is given by formula 2.12,

$$EQE(\lambda) = \frac{I_{ph}(\lambda)}{e\phi_{ph}(\lambda)} \tag{2.11}$$

Under short circuit conditions, The EQE shall be integrated over the photon flux to obtain the short circuit current I_{sc} :

$$I_{sc} = \int_0^\infty EQE(\lambda)\Phi(\lambda)d\lambda \tag{2.12}$$

2.6. Losses and recombination mechanisms

According to Smets *et.al.*, the solar cell performance is limited by losses mainly [17]

1. **Non-absorption of long wavelengths :** the absorption of photons is limited by the energy gap of a semiconductor. Photons with wavelengths corresponding to energy less than the bandgap, E_g is not able to excite an electron and hence not absorbed by the solar cell.

2. **Thermalisation of excess absorbed energy :** The electrons and holes tend to occupy the bottom of the conduction band and the top of the valance band. When photons with energy higher than E_g is absorbed and excess energy is released to the lattice in the form of thermal energy (seen in the figure 2.4).

3. **Total reflection losses :** As already mentioned in the section 2.2, at the interface of a media a portion of the light is reflected and only the remaining light is available for absorption.

4. **Recombination losses :** The photo-generated charge carriers are subject to recombination losses. The recombination of charge carriers either happen in the bulk, at the interfaces and/or junction surfaces. This recombination phenomenon is a result of material properties forming the junction which will be discussed in detail in upcoming sections.

Recombination: The process by which the light generated electron-hole pair concentration, decay back to their equilibrium value at dark is termed recombination [21]. This recombination also leads to a loss of generated charge carriers before collection. These possible mechanisms are overviewed in the next short topics.

1. **Radiative Recombination :** This is the reverse of the absorption process explained in the section 2.1.1. This type of recombination mechanism is prominent in direct bandgap semiconductors as the indirect bandgap semiconductors require.

2. **Auger Recombination** This type of recombination including three particles (two electrons and one hole or two holes and one electron as illustrated in figure). Instead of radiation emission, the energy is transferred to a third particle and later relaxes back to its original state emitting phonons.

3. **Shockley-Read-Hall Recombination** Shockley-Read-Hall Recombination is the mechanism of a single electron trap recombination developed by Hall [31] and Schokley and Reed [32]. Net recombination is a result of two capture and two emissions phenomenon. This happens in a localised energy state when a hole occupied state capture an electron or electron occupied state capture a hole [17].

Surface Recombination: Apart from the above-mentioned bulk recombination mechanisms the semiconductor has surface recombination phenomena arising from the unpaired valance band electrons alias *dangling bonds*, which occurs at the surface of the material. These materials terminated at surfaces act as recombination sites for carrier charges. For pure semiconductors, the surface recombination phenomena can dominate bulk recombination [17].

2.6.1. Shockley - Queisser limit

Theoretical efficiency limit of single-junction solar cells, considering the spectral mismatch losses and thermalization losses are given by Shockley - Queisser (SQ) limit. The major loss mechanisms that are taken into account in the figure 2.16, other losses referred to in the image account for voltage losses due to thermal radiation and fill factor losses. The highest efficiency is dependent on the spectrum and it is important to note that the SQ limit illustrated in the figure 2.15 is under the assumption that only radiative recombination is present. For the materials of the solar cell with dominant non-radiative recombination mechanisms (eg. Auger recombination mechanism in indirect bandgap materials), the SQ limit is not directly applicable.

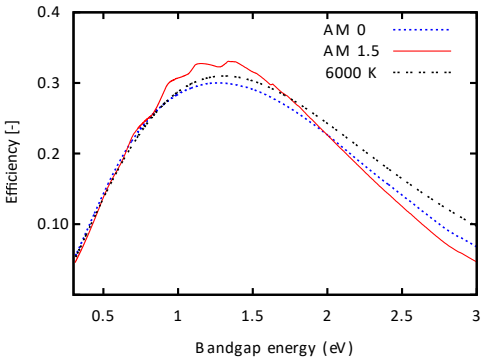

Figure 2.15: The Shockley-Queisser efficiency limit for the black body spectrum at 6000 K, and the AM0 and AM1.5 solar spectra. Inspired by [17]

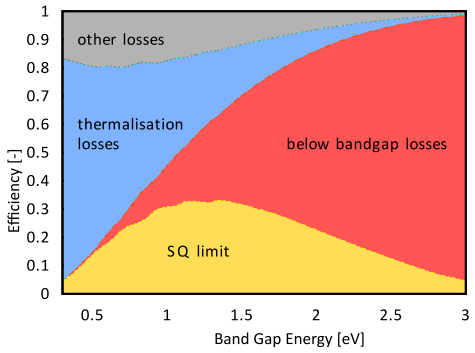

Figure 2.16: The major loss mechanisms in the Shockley-Queisser limit (Considering AM 1.5 Spectrum). Inspired by [17]

2.7. Thin film solar cells and modules

Thin-film solar cells exhibit mechanical advantages from flexibility and lightness and also abundant materials can be used [33]. Tandem solar cells can be beneficial in low energy payback times [34] due to low material usage and terms of less fabrication heat input.

Considering the fabrication aspects the making of thin-film modules are different from crystalline silicon cells, unlike the crystalline cells the modules of a thin film cannot be separated from each other [5]. The processes followed in thin-film module manufacturing for interconnecting them can be illustrated in the figure 2.17 and 1.4described in detail in3.5.4.

2.8. Micromorph configuration tandem solar cells

The multi-junction solar cells concept is the idea of depositing one absorber layer over the other to maximise spectral splitting. The layer materials are determined according to the bandgap properties and absorption coefficients. The top absorber layer constitutes the higher bandgap materials absorbing low wavelength light and the bottom layer is aimed at high wavelength spectral absorption. The dual-junction cell has an efficiency which is a function of the spectral absorption thereby the energy gap of individual cells, work of F.

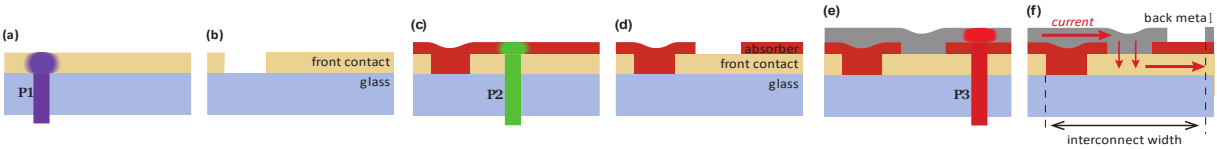

Figure 2.17: Schematic of creating an interconnect in thin-film module. The processes are in order from (a) to (f). Inspired by [17]

Meillaud *et.al.* on solar cell efficiency limits suggests that a combination of a-Si:H/µc-Si:H is best for tandem solar cells [35]. The optical absorption of these materials is shown in the figure 2.18. As a part of Flamingo PV, this tandem micro morph (a-Si:H/µc-Si:H) structure is discussed in the following sections.

The top layer of a micro morph structure is an intrinsic a-Si:H absorber layer with a bandgap of 1.75 eV, which would result in absorption of light below 700 nm wavelength. The bottom subcell of a micro morph structure is intrinsic µc-Si:H absorber layer with a bandgap of approximately 1.12 eV responding to wavelengths of light below 1100 nm (the layer structure is depicted in the figure 2.21).This approach gives option to minimise the light-induced degradation due to the *Staebler Wronski effect* (SWE) (section : 3.2.2) by using thinner cells of a-Si [33]. Also the absorber layer thickness decrease cause a proportional increase in electric field. Fabrication of micromorph cells and the material characteristics of its layers are discussed in detail in chapter 3.

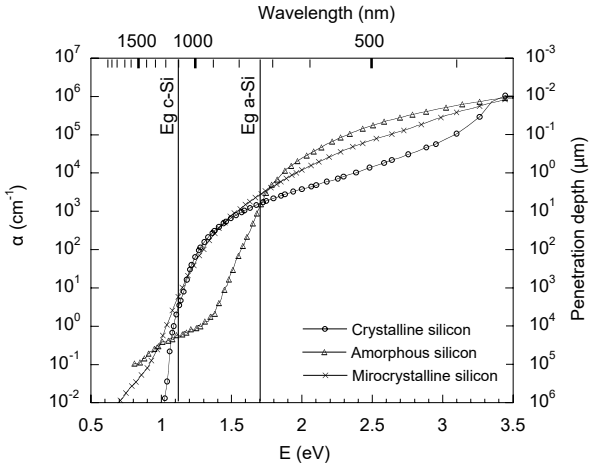

Figure 2.18: Absorption coefficient (α), penetration depth (d_{pen}), as a function of wavelength (λ) and photon energy ($h\nu$) of incident light for different thin film materials. Adapted from [6].

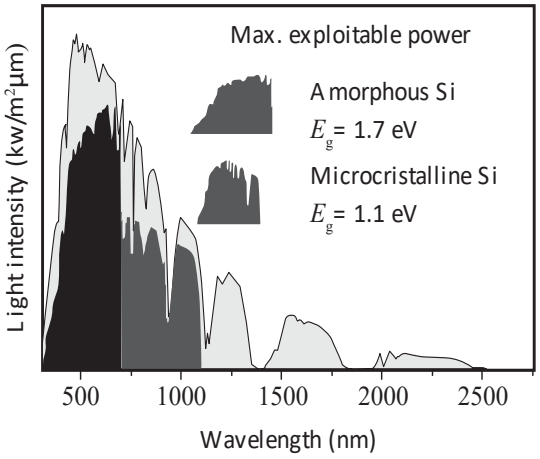

Figure 2.19: Solar spectrum compared with the maximum power that can be generated using amorphous and microcrystalline silicon. Inspired by [36]

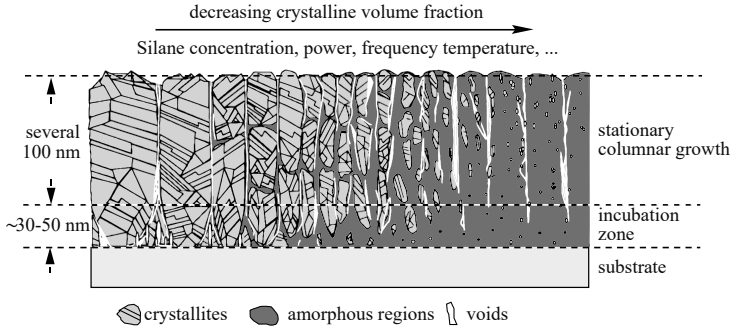

Figure 2.20: Schematic view of the structure of $upmu$c-Si:H ranging from highly crystalline on the left to amorphous on the right - a cross-section view on a foreign substrate. Image courtesy: Shah, A. (2010). Thin-film silicon solar cells [36].

A tandem cell is two *pin* cells stacked one over the other each consisting of one active absorber layer each. When delivering power to the external circuit the electrons generated in the top cell is collected at the *n*-layer

of the top cell and the holes generated in the bottom cell move towards the internal *p*-layer. These generated carriers recombine in the middle *np* junction, the TRJ (refer to the image 2.21. This condition is the forward biased state of a TRJ.

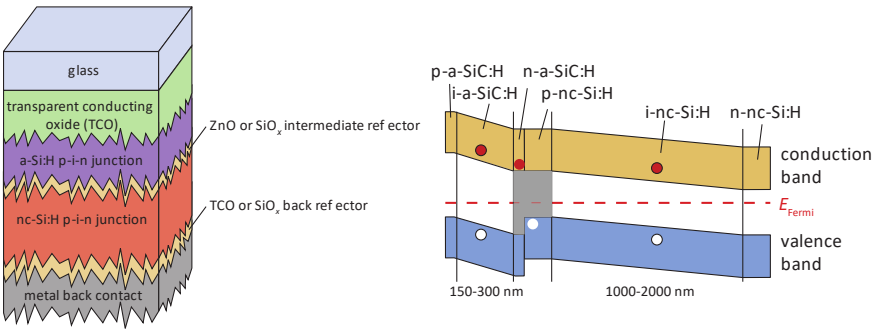

Figure 2.21: Micro morph configuration Tandem solar cells and their band diagram. The area represented in grey shows the Tandem Recombination Junction. Inspired by [17].

TRJ has a significant role in determining the FF and V_{oc} of the tandem cell. Provided the TRJ has no voltage loss across the V_{oc} of a tandem cell is the sum of the V_{oc}-s of an individual cell. Such a loss-free addition is accomplished when the majority carrier quasi-Fermi levels in the doped layers of TRJ-s have approximately the same value [37] leading to zero internal bias across the TRJ. Refer figure 2.22

TRJ is supposed to conduct the generated current with a very low bias voltage. A "poor" quality TRJ behaves like a series resistance [37] which requires non-negligible internal bias voltage subsequently bringing down the FF value and the conversion efficiency.

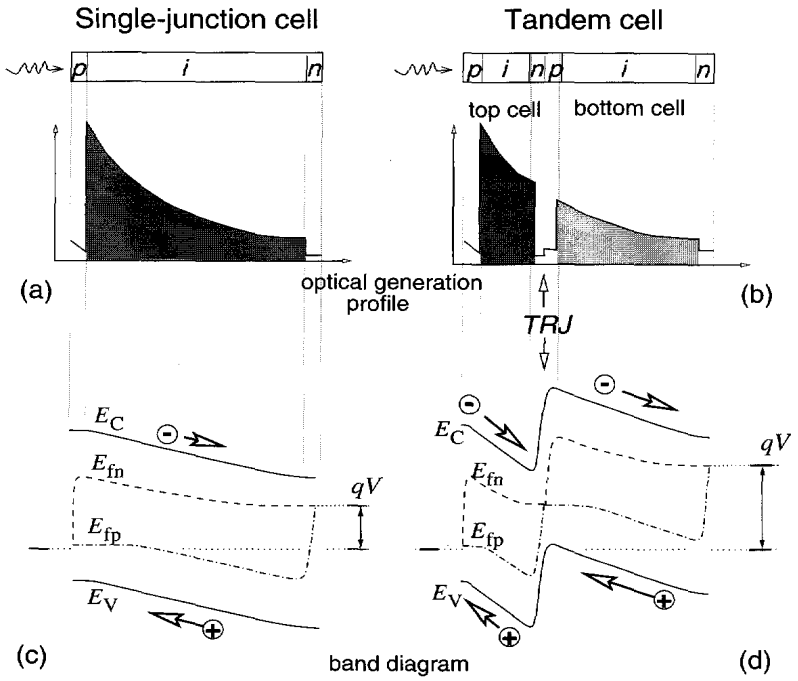

Figure 2.22: Generation profiles : (a) single junction (b) tandem. Band diagrams of : (c) single junction and (d) tandem in power generation state.[37].

The most probable transport mechanisms in the TRJ is as shown in the figure2.23. The figure shows the mechanism of tunnelling in this case, if there is a high electric field across the TRJ the barrier is very thin and carriers can easily penetrate through.

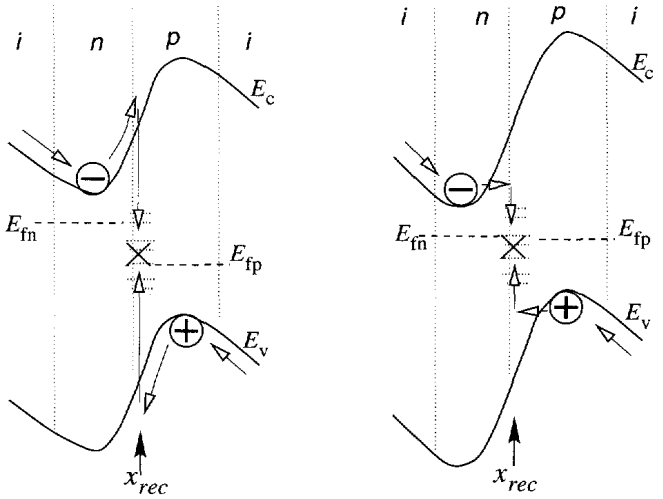

Figure 2.23: Schematic diagrams representing the carrier transport to the recombination junction through extended valance and conduction band and tunnelling respectively [37].

2.8.1. Current matching

When we assume that the electron-hole pairs generated in the absorber layers contribute to the J_{sc}, a maximum short circuit current is attained when the number of photon absorption in both the layers are equal. Otherwise, it will lead to a mismatch, resulting in a current limited situation dictated by the cell which absorbed the lowest amount of photons. Also. in this case a forward 'self' bias voltage is developed across the excess carrier holding sub-cell subsequently resulting in their recombination [37]. Thus, as a first-order approximation, we can conclude that in a current matched state the J_{sc} of the tandem cell is half the total value of total absorption by the cell. The current is reduced to half at a gain of voltage, which reduces the power losses due to TCO losses by a factor of 4.

2.9. Introduction to Opto-Electronic modelling

For the improvement and fabrication of high-efficiency solar cells, numerical simulation has become a very important tool worldwide. Technology computer-aided design (TCAD) tools were created to develop and optimize semiconductor process technologies and devices. These modelling techniques are significant in getting insights into the physical operation of a device [38]. Modelling helps to predict the performance of solar devices without the real fabrication of cells. This approach of modelling a cell is particularly helpful in time-consuming and material consuming experiments such as optimisation of performances which otherwise will need hours of deposition time and many fabrication steps. The TCADs can be one two or three dimensional in their nature to simulate electrical thermal and optical characteristics.

Advanced Semiconductor Analysis (ASA) is a semiconductor simulation program developed by Delft University of Technology[39] for the modelling of amorphous and crystalline silicon devices. ASA is a one dimensional (1-D) device simulator that can occupy multiple layers, replicate wide bandgap materials, describe complete DOS as a function of energy and calculate defect state distribution.

2.9.1. Thin-film modelling

Thin-film solar cells made of amorphous and polycrystalline materials - for example, hydrogenated amorphous silicon (a-Si:H) and hydrogenated microcrystalline silicon (μc-Si:H) in micromorph configuration - requires advanced optical solvers and need detailed physical models implemented to describe their specific electronic properties [38]. The optical and electrical modelling aspects of thin-film modelling are discussed in the chapter 4 considering ASA.

3

Device Fabrication and Material Characterisation

This chapter focuses on fabrication and materials aspects of micromorph silicon devices for experimental study. An overview of the process flows is given in the figure 3.1. These processes are discussed in detail and preliminary study on texturing and fabricated cells are done in this chapter. Initially, the deposition and characterisation techniques used for manufacturing the cells are described. Section 3.5 and 3.6 recounts the fabrication steps and texturing properties. In the succeeding topics, the chapter discusses the issues and yield of this procedure. The chapter concludes with an alternative structure and observations.

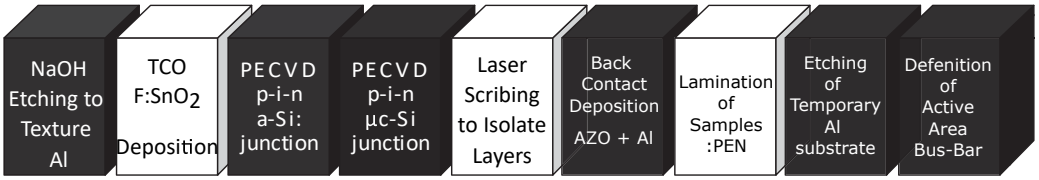

Figure 3.1: Diagram flow for the making of thin-film silicon modules based on a-Si:H and µc-Si:H.

3.1. Deposition techniques

The manufacturing of thin-film silicon devices includes multiple deposition techniques like plasma-enhanced chemical vapour deposition(PECVD) and Magnetron sputtering. The following section discusses the technical end of deposition techniques and process conditions for micromorph samples depositions.

3.2. Plasma enhanced chemical vapour deposition (PECVD)

A pure form of silicon for thin-film devices can be deposited using vacuum techniques. Plasma is the ionised gas state which is macroscopically neutral [40]. The technique uses precursor gases that are ionised by an electric field using RF power electrodes. The substrate holder is often heated to 200°C and placed between the plates, which is schematically shown in the image 3.2. While the plasma bulk is neutral in nature, there exists a space charge region - the sheath boundary[40]. This occurs between the substrate and the plasma as in the figure 3.3. The sheath acts as a selective cover, it accelerates the positive ions to the substrate while helps to confine the electrons, negative ions and powders inside the plasma[40]. Moreover, the sheath allows the diffusion of neutral radicals also through the boundary to the substrate. This concept is illustrated with the help of the diagram in the figure 3.3.

For both amorphous and nanocrystalline silicon, Silane and hydrogen gas are used as precursor gases. Once Silane gas is injected into the chamber, the Si_xH_y type of radicals are generated in the plasma chamber. The SiH_2, SiH, SiH_3 are the main radicals formed in the reactions and among these the SiH_3 with the longest lifetime and thereby the highest concentration in the chamber[42]. These deposited materials can be either amorphous - without specific order or of nano(micro)crystalline nature with crystallites of silicon possessing diameters 1µm or less[36] depending on deposition conditions and Silane (SiH_4) flow rates. The image 3.4 is the popular model to explain aSi:H and µcSi:H growth adapted from [40].

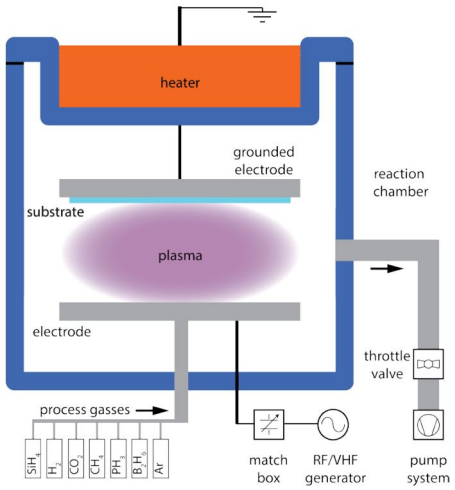

Figure 3.2: Schematic diagram of a plasma enhanced chemical vapor deposition reactor. Adapted from[17][41]

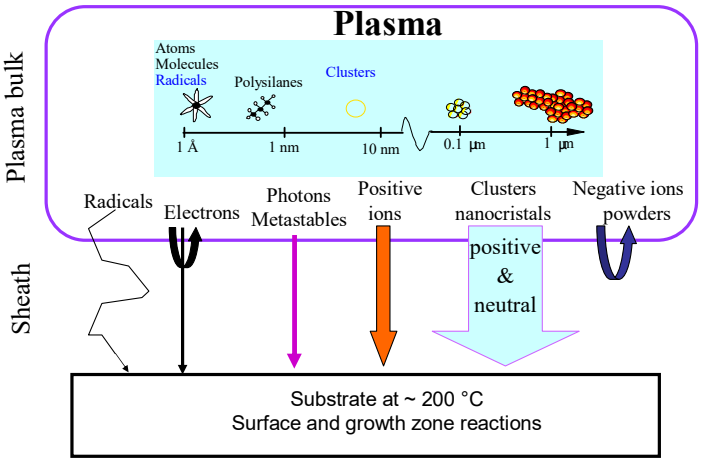

Figure 3.3: Reactive species in the plasma and their selectivity through the sheath. Adapted from [40]

Amigo cluster tool

Samples deposited for this thesis are prepared in a cluster tool from Elettrorava called AMIGO with 6 chambers for silicon deposition. Chambers in AMIGO are dedicated to p-doped, n-doped, intrinsic a-Si:H, intrinsic µc-Si:H depositions. Apart from these, AMIGO has two other chambers - one for special silicon alloys like silicon carbides and nitrides and one chamber for sputtering AZO.

3.2.1. Amorphous silicon deposition

SiH_3 is the important radical responsible for a-Si:H film growth. The radical has two possible interactions : incoming SiH_3 detaching the hydrogen bond from the surface thus forming SiH_4, leaving behind a dangling bond or incoming SiH_3 interacting with the so formed dangling bond, forming a Si-Si bond thus contributing to film growth [40].

3.2.2. Light-induced degradation (Staebler-Wronski effect)

The amorphous silicon layer when exposed to light, exhibits a decrease in performance. This degradation effect is called the Staebler-Wronski effect (SWE). When the layer is treated at a temperature state of 150°C for a few hours or even higher temperature (250°C) for a few minutes can reverse this effect. This treatment results in an effective "passivation" or "healing" - the state similar to a state before SWE. According to A.Shah [36] the only existing two methods to prevent/counter act the SWE are, (i) an increase in the deposition temperature [43]; and (ii) *hydrogen dilution*, which is the deposition technique of depositing amorphous silicon layers from a mixture of silane and hydrogen [44], [45].

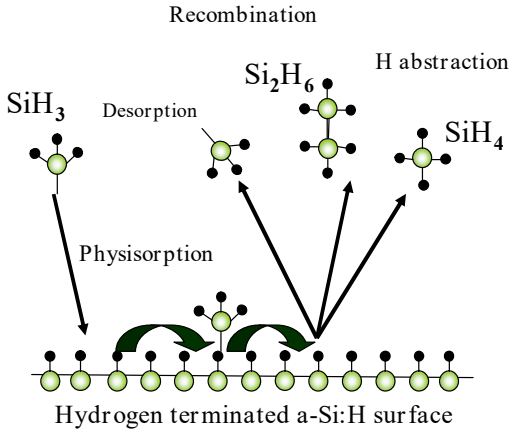

Figure 3.4: Representation of a-Si:H growth based on SiH_3 radicals. NB Atomic hydrogen is ignored. .Adapted from [40]

3.2.3. Micro crystalline silicon deposition

Device grade microcrystalline silicon is a material that can be fabricated using PECVD using Silane (SiH_4) and Hydrogen(H_4) gases in a process similar to a-Si:H deposition. But the role of Hydrogen atoms is more prominent in the epitaxial-like growth of nanocrystalline silicon material. Probably the energy barrier between the amorphous and crystalline phases is overcome by the energy released by the recombination of hydrogen in the silicon network (poorly interconnected state)[40].The (SiH_3) hence deposited is bonded in a more favourable energy state and results in an ordered growth thereby acting as nucleation sites for aforementioned epitaxial-like growth [40].

µc-Si:H is a mixed-phase material composed of silicon nanocrystals that facilitate charge carrier generation and mobility. These nanocrystals are embedded and passivated in a-Si:H matrix [36] as depicted in figure 2.20. The material properties of nano-crystalline silicon strongly depend on deposition conditions. The material is almost unaffected by light-induced degradation or charge injection to absorber layers (the Staebler-Wronski effect).

3.2.4. Deposition parameters

The quality of deposition is determined by different parameters of deposition. With an increase in power, the electric field split the gases and ion formation is increased subsequently resulting in a high deposition rate. But at the same time raised ion motion results in more bombardment of ions with the thin film deposition which is potentially damaging. This issue can be resolved with increasing excitation frequency which can, in turn, result in a diminished sheath boundary and reduced excitation of ions[46].

Substrate temperature directly affects the defect states in the deposited layer as it determines the bonding of SiH_3 at the surface of the layers, which in turn influence the defect concentration through surface reaction rates. Pressure maintained in the chamber determines the inelastic collisions, diminishing the momentum of the ions in the plasma which has direct impacts on both optical and electrical properties of the silicon layers deposited[40]. The inflow of gases for deposition determines the number of entities to be ionised (whether surplus or deficit) and thus determine the phase of the material that is deposited. It shall be noted that the increase in power is not sufficient to increase the deposition rate but also require an increase in silane flow, which will, in turn, regulate the type of material deposited[40]. Thus the parameters are interdependent and demand fine-tuning to achieve device grade deposition.

3.3. RF Magnetron sputtering

Sputtering is a physical vapour deposition (PVD) technique that has no chemical reactions involved. This is a popular technique for depositing TCOs (indium tin oxide and aluminium-doped zinc oxide) due to its comparatively high deposition rate and scalability [40]. An RF generator applies an alternating field in the chamber which ionises the inert gas - Argon (in the case depicted in 3.5). This generated positive Argon ions hit the target displacing the atoms from the target surface. These entities are later deposited on the substrate[41].

The *Magnetron* sputtering approach applies a magnetic field perpendicular to the electric field to confine the electron to the electrode surface. The process needs careful attention in tuning the parameters to impart good electrical properties to the deposited layers as high ion bombardment can potentially damage the layers degrading the quality [47].

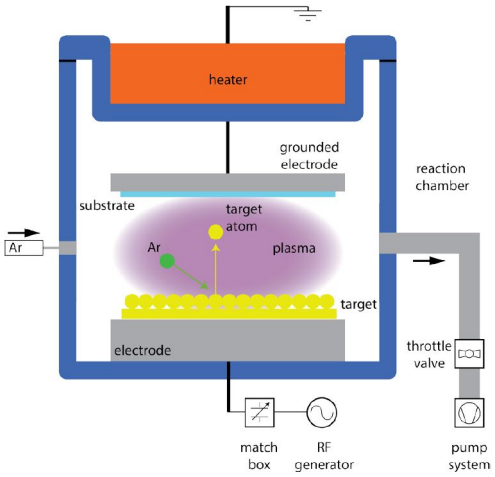

Figure 3.5: Schematic diagram of a physical vapor deposition sputtering. Adapted from[17][41]

3.4. Characterisation techniques

This section introduces the characterisation techniques of the samples fabricated as a part of the thesis. Solar cell characterisation is done using an array of different techniques such as dark/illuminated J-V, dark conductivity, activation energy measurement and ellipsometry. Each technique has its own advantages, applicability and disadvantages. Ellipsometry can only be used for non textured flat glass. Ellipsometry and confocal microscopy are non-destructive while Scanning electron microscopy (SEM) is a destructive testing method as the sample need to be cut to specific sizes. The activation energy measurement similarly requires contact layer deposition for characterisation. This study primarily utilises SEM, J-V and confocal microscopy.

3.4.1. Current-Voltage (I-V) characteristics measurement

For this thesis to identify illuminated and dark mode current-voltage characteristics of the fabricated cell, a WACOM - class AAA solar simulator is used. The simulator uses Xenon and Halogen lamps to replicate the AM1.5G spectrum. The stage is kept at 25°C throughout the measurement. Red range wavelength spectrum is imitated using Halogen (600nm-1500nm) and Xenon lamp produces the blue wavelength range from 350nm to 600nm.

3.4.2. Scanning Electron Microscopy (SEM)

SEM is a method to observe the features of nanometer order which are smaller than the wavelength of light. SEM uses an electron stream with a smaller wavelength for microscopy. The electron beam is bombarded on the surface to produce a secondary electron stream which is utilized to create an image. Scanning electron microscopy is a destructive method for samples of significant size (like the samples of 10cm X 10cm deposited for studies in this thesis). It also faces some limitations in resolution in finished samples of flexible cells due to glue interaction with accelerated electrons.

3.4.3. Confocal microscopy

This optical microscopy technique is used to make surface profiles in this thesis. Laser light is focused on a point on the sample. The main components are pinholes, objective lens, dichromatic mirrors and laser shown in the figure 3.6. It passes through a collimator and is reflected on a dichromatic mirror to the objective lens. The beam sweeps over the area to build the image. The reflected light traces through the objective lens and mirror and it is detected by high sensitive photomultipliers[48].

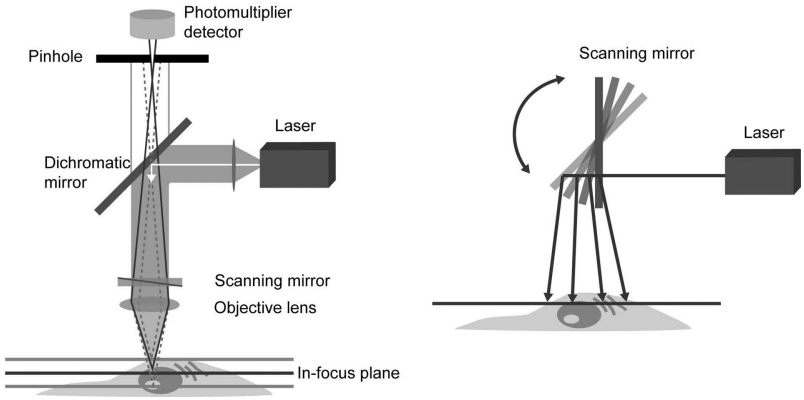

Figure 3.6: Schematic diagram of a Components of a confocal microscope. Adapted from[48]

3.5. Fabrication Of flexible tandem device on aluminium substrates

All lab-scale depositions used for this thesis were completed on 10cm X 10cm aluminium foils. These Aluminium foils had an approximate thickness of 100 microns with texturing. Transparent conducting oxide used is a fluorine-doped tin oxide (ZnO:F). The steps in the making of a lab-scale device are discussed in this section in order.

3.5.1. Textured aluminium substrates: FLAM01

The unique methodology followed in HyET as described in the section 1.3 allows texturing of temporary aluminium substrates, to be transferred to the solar modules to make use of light scattering[14]. The texturing used in industry will be referred to as *factory baseline* from now on. The pictures of baseline texturing are included in images 3.7 and 3.8. The baseline texturing is characterised by RMS roughness (σ_{RMS}) = 28.4 nm, auto-correlation length (L_c) = 497 nm, and aspect ratio (σ_{RMS}/L_c) = 0.057 [49].

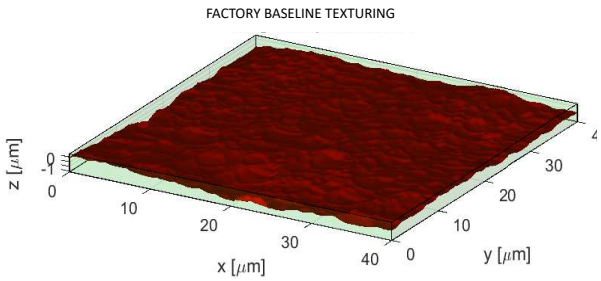

Figure 3.7: Baseline texturing of Aluminium + FTO used in industry. Generated by GenPro4, AFM data measured by D.Rajagopal[49]

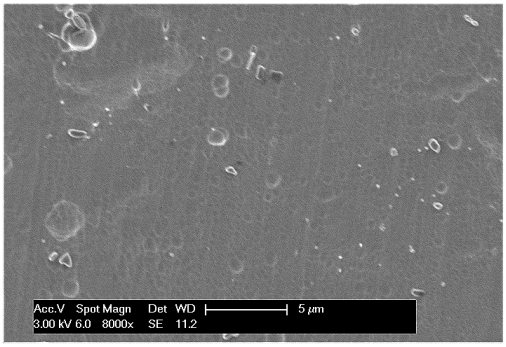

Figure 3.8: Baseline texturing of Aluminium used in industry. SEM image by D.Rajagopal[49].

As a part of Flamingo PV project a new texturing was developed by D.Rajagopal in 2020 with auto-correlation length (L_c) = 2270 nm, Aspect ratio (σ_{RMS}/L_c) = 0.1223. It was reported that the sample showed a broader AID curve compared to factory baseline and higher reflectance haze (76%) [49]. This texturing is named *FLAM01* (as further used in this report). This method results in a 95-micron thick foil starting from 110-micron aluminium, but in the R2R machine, it is difficult to attain the best texturing with this specified thickness reduction. To overcome this limitation a new version of texturing technique is under development for which thicker initial foils are used for etching - the *FLAM02* [50].

On comparing the images 3.8 and 3.10, a noticeable change in the appearance of crater radius is observed. FLAM01 has craters with sizes comparable to the red wavelength range of the spectrum, enhancing respective scattering.

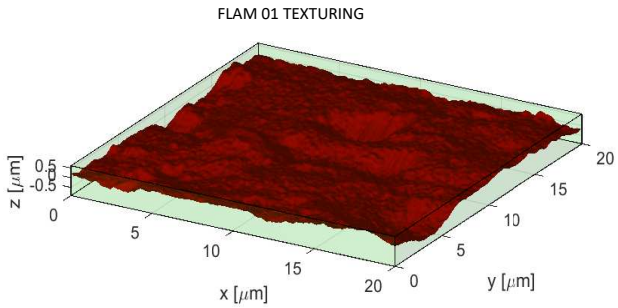

Figure 3.9: FLAM01 texturing of Aluminium + FTO used. Generated by GenPro4, AFM data measured by D.Rajagopal[49]

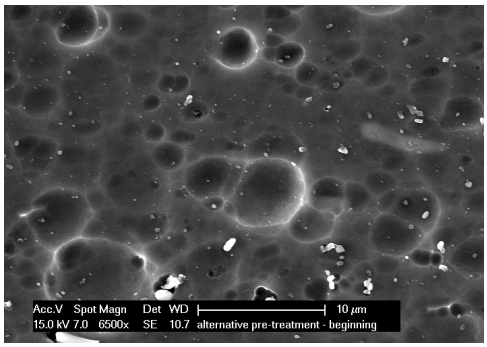

Figure 3.10: FLAM01 texturing of Aluminium used in industry. SEM image by D.Rajagopal[49].

FLAM 01 is prepared in the lab and later optimised for R2R processing of the aluminium rolls. The procedure includes etching the Al foils for 1.8 minutes at a temperature of 50°C in a 1.42M solution of NaOH diluted in water. Later, the foils are cleaned in a 1% phosphoric acid (H_3PO_4) diluted in water, at the same temperature. This is needed for the removal of the etching residues. Finally, the substrates are dried with a N_2 gun [49].

3.5.2. Deposition of TCO

Fluorine-doped tin oxide (FTO) - $SnO_2:F$ is deposited using atmospheric pressure chemical vapour deposition (APCVD) on aluminium foil. For this TCO layer, the deposition is happening at 500°C temperature. The TCO requires a precise study for making high-efficiency solar modules, the deposition rate and deposition thickness needs unique optimisations for each substrate material and substrate texturing. An optimised thickness is pre-determined in the industry as 700 nm for TCO for baseline texturing. This same thickness is also used for FLAM01 during this thesis. But this thickness needs to be re-assessed and re-optimised in the future since the crater depth and size is varying heavily in the new texturing.

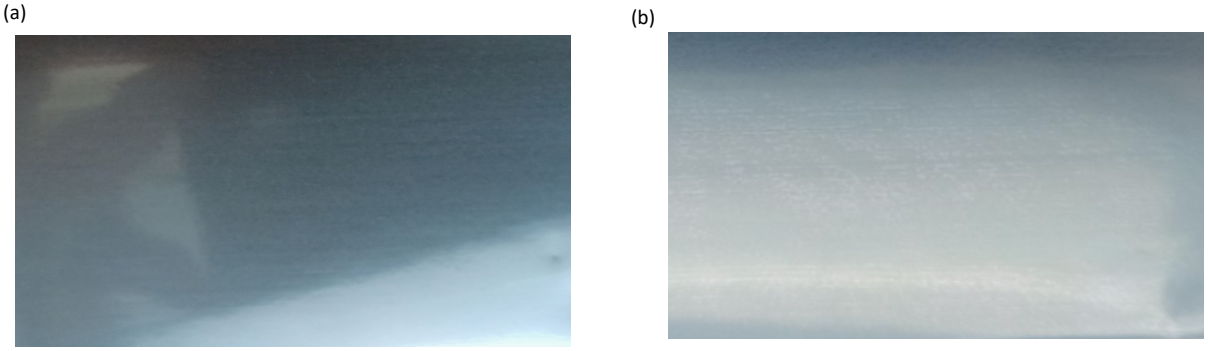

Figure 3.11: Al+FTO for deposition. (a) Baseline textured Aluminium with FTO. (b) FLAM 01 textured Aluminium + FTO. Baseline aluminium is shinier with naked eye, FLAM01 has a higher haze.

3.5.3. Deposition of silicon stacks

The silicon stacks are deposited using the cluster tool AMIGO (refer to section 3.2). The aluminium foils with texturing and 700 nm TCO deposited on it needs to be cleaned before being loaded to the machine. The foils are cleaned in ultrasonic baths of acetone and then in isopropyl alcohol (IPA). The foils are dried using N2.

Each deposition chamber (DPC) has different deposition functionalities depending on precursor gas flows. DPC1 has B_2H_6 as precursor gas while DPC2 has PH_3 inlets which make them suitable for p-doped and n-doped silicon layer depositions respectively. DPC3 and DPC4 are used for intrinsic depositions of amorphous silicon and nanocrystalline silicon in that order. The machine uses carbon dioxide inflows which makes silicon oxide layer depositions possible. The first layer deposited is in chamber 6, which is the sputtering chamber. This chamber preheats the sample for 1800 seconds and then deposit a buffer layer of AZO. The

sputtering of AZO is done at Radio Frequency (RF) 13.56 MHz and a temperature of 300°C. The next layer depositions are silicon layers, the p-i-n stacks forming the top and bottom cells. Top cell a-Si:H is deposited at RF, while the intrinsic nanocrystalline layers are deposited at a very high frequency (VHF) of 40.68 MHz for the bottom cell.

The area of electrodes used is 12 cm X 12 cm. The substrate is mounted on the grounded electrode (top electrode), and the gas inlet is on the bottom electrode. The electrode has multiple holes for gas inflow to cause uniform flow and stable plasma. The important parameters used for the study of micromorph configuration are found in the table3.1. It shall be noted that the similar doped layers used for TRJ may have various flow rates when compared to other p or n-doped layers in order to facilitate re-combinations.

Table 3.1: Deposition conditions of the layers used in the fabrication of a-Si:H and μc-Si:H cells. The values are taken from the standard recipes defined for the AMIGO cluster tool. The used values are the standard recipes for the machine.
B_2H_6** = B_2H_6/H_2(200ppm), PH_3** = PH_3/H_2

Layer	Power [W]	Pressure [mbar]	T[°C]	Gas	Flow rate [sccm]
AZO	300	2.6	300	Ar	20
$\mu c - SiO_x(p)$	12	2.2	300	SiH_4 B_2H_6* CO_2 H_2	0.8 20 2.3 170
a-Si:H (i)	2.8	0.7	300	SiH_4 H_2	40 0
$\mu c - SiO_x(n)$	11	1.6	300	SiH_4 PH_3** CO_2 H_2	1 1.2 2 170
$\mu c - SiO_x(p)$	12	2.2	300	SiH_4 B_2H_6* CO_2 H_2	0.8 60 1.6 170
μcSi : H (i)	40	4	180	SiH_4 H_2	3.5 120
$\mu c - SiO_x(n)$	11	1.6	300	SiH_4 PH_3* CO_2 H_2	1.0 1.2 1.6 170
a-Si:H (n)	4	0.6	300	SiH_4 PH_3* CO_2	40 11 0

3.5.4. Cell definition : Laser scribing

Laser scribes are used to partition the cells and define the active areas for each sample. This procedure is schematically represented under the section 2.7. Each sample readily requires three scribes. to do this : firstly, to cut through all the layers from FTO to the bottom silicon layer - P1 scribe. Secondly, a laser scribe to cut through the silicon layers only - P2 scribe, and the third scribe to break back contact's continuity - P3 scribe. But the lab samples made for this thesis does not require the second scribe as it requires no interconnection.

Also, aimed at reducing the number of scribes, breaking back contact continuity is achieved using the lift-off ink method which does not require lasers. In effect, only one scribe is made with a laser that cuts through the sample which in turn is filled with a non-conductive ink dispensed into the scribe.

Figure 3.12: Appearance of Silicon deposited on the aluminium using AMIGO.

Figure 3.13: Appearance of cells after scribing. The thin lines are laser scribe and dark lines are lift off ink.

3.5.5. Deposition of back contact

Back contact sputtering has two layers associated with it, one is the AZO layer deposited at 80 nm thickness and the next layer is 300 nm of aluminium. The aluminium deposited also acts as a reflective layer. Both the layers are deposited using magnetron sputtering. The AZO layer at the back is deposited with RF at a power of 407W and an argon flow rate of 40 sccm. The aluminium layer is DC sputtered at an argon flow rate of 19 sccm.

Removal of Aluminium - the P3 scribe : A portion of the deposited aluminium layer needs to be removed to isolate the cells. This process is done by brushing the sputtered area with a tissue dipped in IPA. The rough texture of lift-off ink can easily remove the aluminium depositions in a straight line and provide the required electrical discontinuity.

3.5.6. Solar cell carrier

The permanent carrier of the solar cell adheres to the sample with the help of glue on the sputtered side. The material polyethylene naphthalate (PEN) is used for this purpose. This material provides flexibility for the cell and ensures backside encapsulation for the cell. The process is completed with a press.

3.5.7. Etching of aluminium

Once the solar cell is transferred to PEN, the temporary aluminium can be etched away in the next step. NaOH 1.2M at 70 degrees is used for this purpose. The etching is done in two different steps. As the first step, we etch approximately 80 microns of the foil, from the initial material thickness of 100 microns. The thin sample's etched side is cleaned using 0.1M H_3PO_4 and water at 60°C.

The next step is curing the glue in an epoxy oven at 170°C for 20 minutes. The secondary etching process is done to define the active area and bus bar. The area from where aluminium is etched off forms the active area. To define the bus bars insulation tapes are pasted on the required area, leaving behind aluminium stripes acting as bus bars.

3.5.8. Encapsulation - ETFE/GLUE

The solar cell is encapsulated with ethylene tetrafluoroethylene (ETFE) with the help of glue. These layers are necessary to protect silicon encapsulants from the environment. The top side encapsulates consists of 4 layers, ETFE-glue-ETFE-glue in that order and this process is expected to increase the efficiency of the solar cell. Observing historical data of HyET modules, it is observed that this encapsulation step results in an

approximate increase of 5% in total spectral response. The measured refractive index value of ETFE is 1.43 with negligible absorptive behaviour.

3.5.9. Finished cell

The cells finished as part of this thesis are of different active areas namely 2.5cm^2, 0.81cm^2, 0.36cm^2.

Such a finished cell of area 2.5cm^2 is shown in the figure 3.14. In the image, the scribe P1 can be seen on the left and the bus bar on this side is the back connected metal. The other side of the active area is the P3 scribe which marks the back contact isolation and the aluminium on the side is the front contact of the cell. This sample is not encapsulated. The electrical layers, bus bar connections and scribes are schematically shown in 3.15.

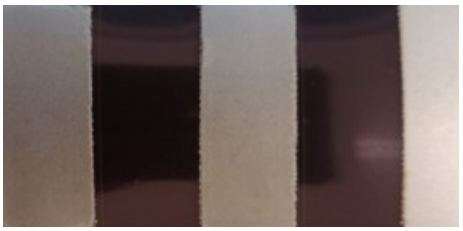

Figure 3.14: The cell after substrate etching. Area of solar cell: 2.5 cm^2. The protected area in the etching forms bus bar.

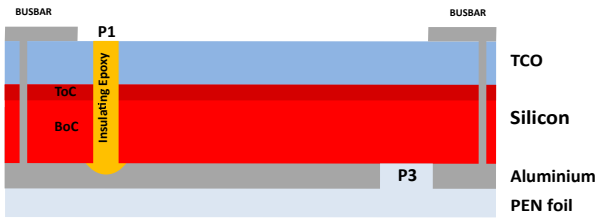

Figure 3.15: Electrical connection and scribe inside the cell

3.5.10. Alternate method

The laser scribing step includes multiple variables in itself, for example, laser power, insulating ink dispensing (which by itself is prone to multiple variations like the viscosity of ink, needle motion etc.) and time for ink curing under the UV light. The power for scribing is decided with the help of visual inspection of the camera captures. The laser wavelength used for scribing is closely associated with the texture present at the interface due to likely scattering. This technique has been under suspicion to create shunts and imperfect openings of the depositions. This possibility for erroneous scribes was studied and discussed in the section 3.8.2. So, to overcome these limitations, a new method of lab-scale fabrication is introduced at HyET, in which the samples are made using masks for sputtering, followed by gluing copper back contacts to replace the scribing step. This sample has two different active areas of 81mm^2 and 36mm^2, resulting in 20 cells per sample. The active area definition and copper contacts are legible from the backside view of the sample in the figure 3.16. The electrical layers, bus bar connections and copper contact after avoiding scribes are schematically shown in 3.17.

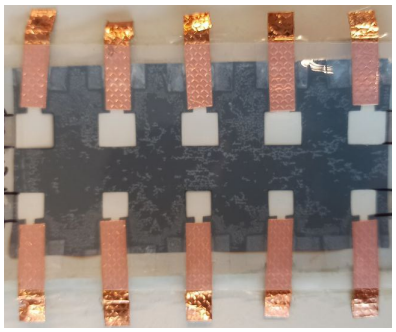

Figure 3.16: The cell after substrate etching. Area of solar cell: 0.81cm^2, 0.36cm^2.

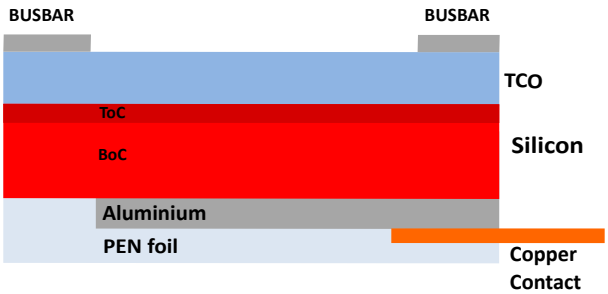

Figure 3.17: Electrical connection and copper contact for the cells to avoid scribes

Currently, there exists an issue with measuring the illuminated performance of these cells due to contact issues. So for this reason the JV parameters of these cells are missing from this report. These type of samples requires sandpaper cleaning of their copper stripes before measurement to make good contact. The copper contacts have a black color deposition after final etching. This new version of lab cells and their processing methods are still under examination.

3.6. Texturing : conformality and foil-cell transfer

FLAM 01 texturing shows appreciable behaviour in light scattering towards the red side of the spectrum as illustrated in the works by D.Rajagopal [49]. While undergoing the fabrication steps, intermediate steps (FTO deposition, buffer layer sputtering, chemical etching at the end) can alter the innate behaviour of the textures and can result in an inefficient transfer to the cell.

3.6.1. Study on conformality of texturing

It is essential to study the conformality of the texturing, in the sense of whether it can be carried over to deposited layers. Though it seems obvious that the texturing fades away with multiple layer depositions, this section takes a look at the texturing imparted by the micromorph sample through the layers after deposition of both the subcells. The part of the thesis is carried out using SEM and confocal microscopy techniques.
Figure 3.18 and 3.19 shows the texturing of FLAM01 foil surface under SEM and confocal microscope. These modulated surface textures gain the bigger craters from aluminium textures (FLAM01) and fine texturing superposed on these craters from the natural textures of FTO depositions.

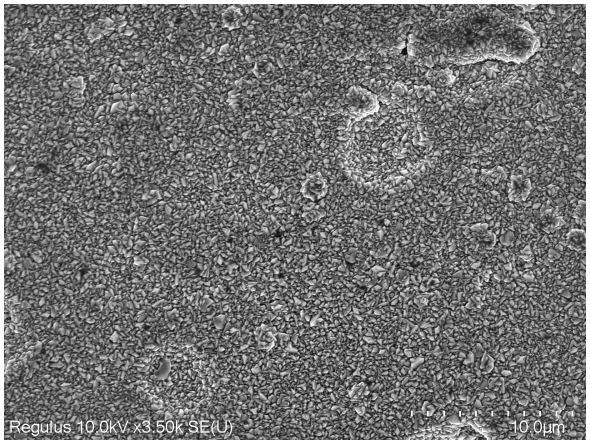

Figure 3.18: FLAM 01 foils deposited with FTO 700nm, image generated by scanning electron microscope.

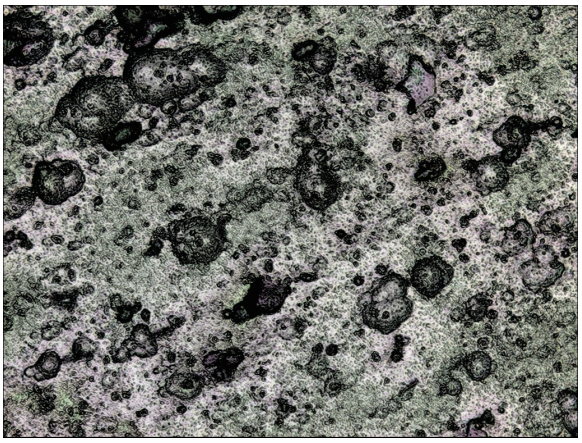

Figure 3.19: Flam 01 foils deposited with FTO 700nm, image generated on confocal microscope.

Figure 3.20 and 3.21 shows the images of microscope deposition on FLAM01 foil on SEM and confocal microscope. The sample viewed has 200nm a-Si:H and 2000nm µcSi:H. Visual inspection of the laser+optical image generated by a confocal microscope strengthens the idea that texture is visible on the surface after deposition. The big craters are carried over and do not fade away completely. The "mushroom shapes" are the nanocrystalline growth and the white spot in this SEM image is the carried over crater similar to the crater in the SEM image of FLAM01 (Figure 3.18). The surface roughness values are recorded in the table 3.2.

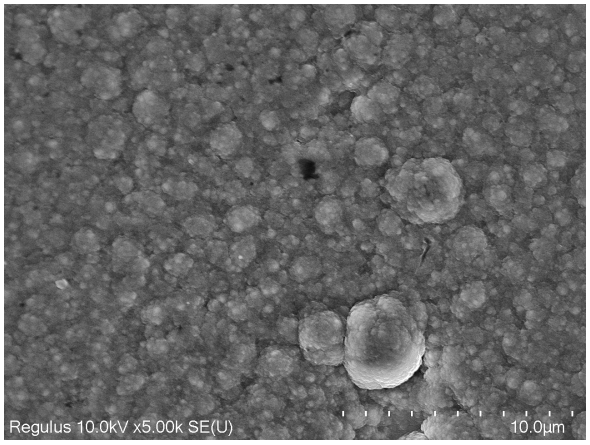

Figure 3.20: Surface after a-Si:H/µcSi:H deposition: SEM image

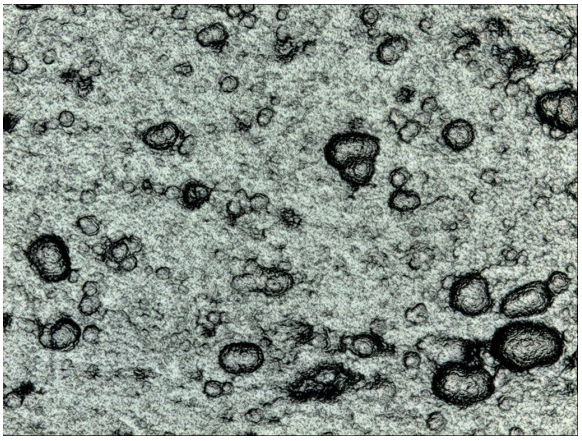

Figure 3.21: Surface after a-Si:H/µcSi:H deposition: laser+optical image by confocal microscope

Table 3.2: Analysis of surfaces using Confocal microscopy and measured characteristics for depositions.

Sample	Average Roughness	Max height	Aspect Ratio	Mean Peak Value	Correlation Length	Area size
	µm	µm	~	mm^{-1}	µm	µm
FLAM01+TCO	0.292	8.420	0.085	2407.474	3.427	30166.404
Deposition - 200/1500	0.259	7.860	0.078	2363.240	3.327	30166.404
Deposition - 250/2000	0.228	8.704	0.061	2149.845	3.759	30166.404

The TCO deposited is 700 nm for the readings. The average roughness, mean peak value and aspect ratio is seen to decrease over the deposition while the maximum height can be seen as a deposition property and seen as increasing with bottom cell deposition thickness.

3.6.2. Texturing transfer from temporary substrate to finished cells

During the production technique described in section 3.5 it is evident that a final solar cell sample texturing depends on the TCO deposition rate and its thickness. A texturing comparison between the FLAM01 on aluminium foil and FLAM01 on a completed measurable state device is done. This case and the images with measurements are done with help of SEM and confocal microscope.

Figure 3.22 and 3.24 are the captured images of the surface of a finished cell. The relevant comparison for carrying over of texture in this study is between FLAM01 aluminium without FTO and Finished cell. This is because the micro texturing caused by FTO is at the interface of FTO and silicon. The larger diameter present on textured Aluminium is carried over as visible bumps on the cell surface.

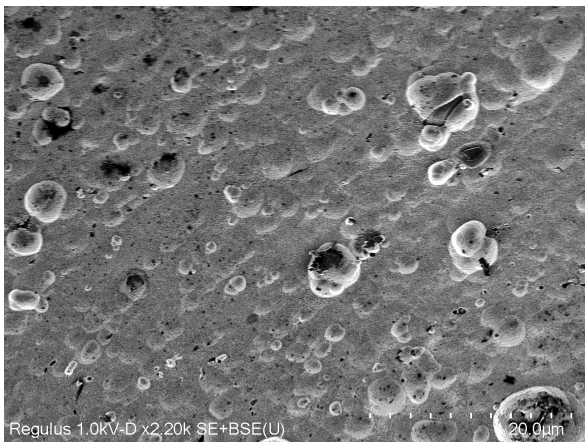

Figure 3.22: Finished cells texturing under SEM

The visually inspected cells and FLAM01 image suggests that the texturing is carried over to the cell surface. Observed characteristic properties from the table 3.3 suggest a fall in roughness values, which may be due to the FTO deposition optimisation essential for texturing with bigger craters.

Table 3.3: Analysis of surfaces using Confocal microscopy and measured characteristics for texturing analysis on finished cell.

Sample	Average Roughness	Max height	Aspect Ratio	Mean Peak Value	Correlation Length	Area size
	µm	µm	~	mm^{-1}	µm	µm
FLAM01	0.255	6.131	0.096	2563.102	2.659	30166.404
Cell 1	0.204	5.343	0.085	1083.537	2.397	30166.404
Cell 2	0.196	4.839	0.089	1841.731	2.211	30166.404

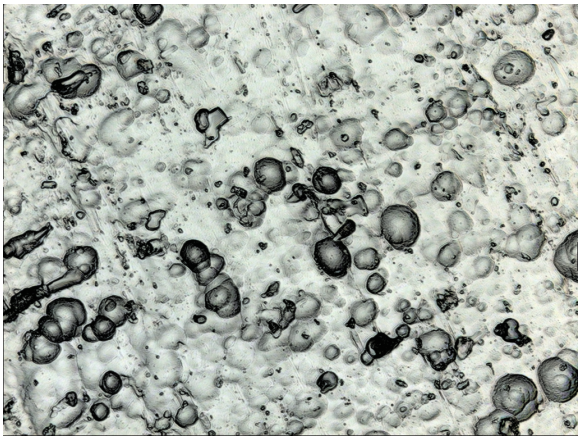

Figure 3.23: FLAM01 texturing: laser + optical image from confocal microscope

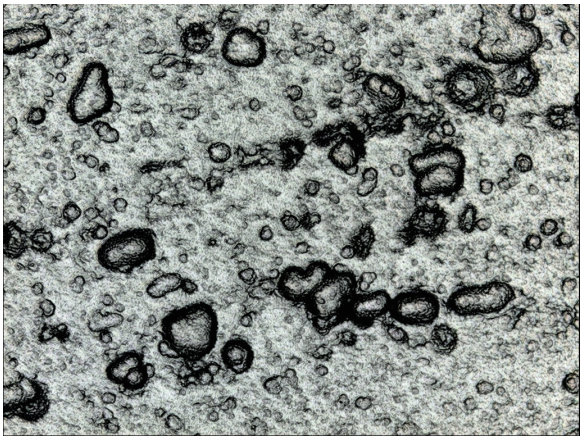

Figure 3.24: Finished cells texturing : laser + optical image from confocal microscope

3.7. Experiments on tandems - FLAM01 texture

At this end of the thesis, we discuss the fabrication results of micromorph tandems on FLAM01 textured aluminium. To investigate methods of improvement on the performance of micromorph tandems on FLAM01 texture, the following structure is adopted.

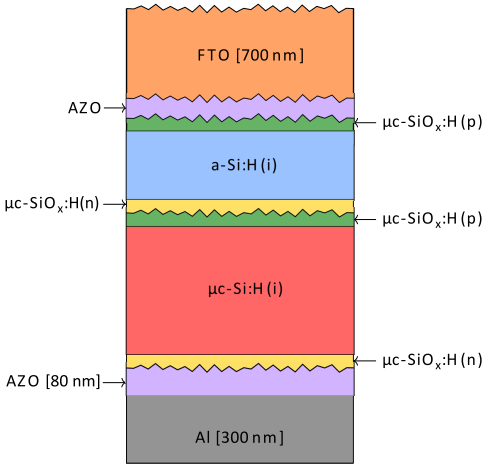

Figure 3.25: Fabricated model FLAM01 tandems

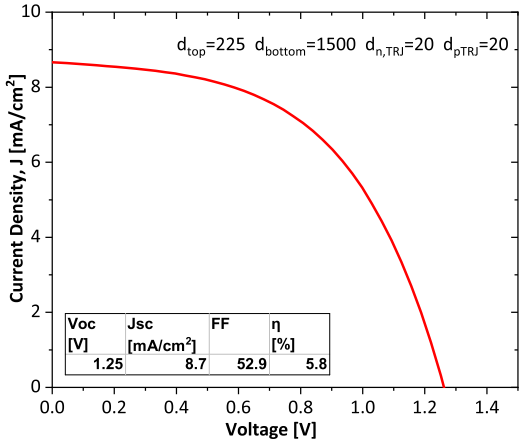

Figure 3.26: JV of micrimorph tandems :d_{top}= 250nm and d_{bottom} = 2000nm.

The FTO layer on top is 700nm thick, AZO layers deposited accounts for 20 nm and act as a buffer layer. The p and n-doped layers for top cell and bottom cell are µcSi : O_x material. a-Si:H is the top cell absorber and µcSi:H is the bottom subcell absorber. The thicknesses of electrical layers of the cell are not specified in the image as it is changed in the experiments. The p-µcSi : O_x layers are aimed for better band bending properties [51]. The nanocrystalline silicon oxide TRJ layers can result in the good optical performance of the cells and shall be heavily doped to facilitate more defects and recombinations [52]. The bottom cell model is similar to the nanocrystalline single-junction cells developed by H.Tan et al.[53]. Seed layers were used for the nanocrystalline deposition intended at good crystalline growth. This is based on previous work by S.B.Nawaratne [54]. The AZO layer of 80 nm is the buffer layer at the bottom and Aluminium forms the back contact. The SEM images of deposited samples and the finished cells are included in this section. The finished cell can only be observed under low resolution as the sample has adhesive glue which interferes with the images at high electron beam acceleration. The deposition has Aluminium and TCO at the bottom. The a-Si:H top cell is visible in a darker shade near the TCO. The top subcell is below the bottom subcell layer in the image due to our substrate etching method. The observed deposition is a 250nm top and 2000nm bottom cell.

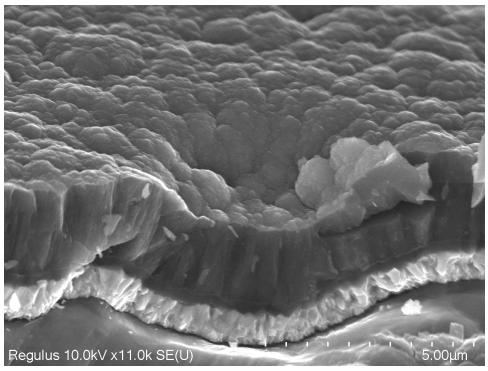

Figure 3.27: SEM image of a deposited tandem cell.

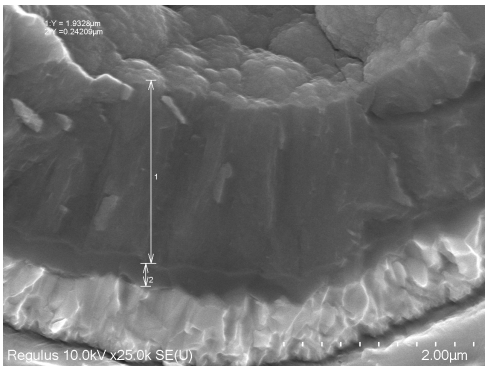

Figure 3.28: Zoomed in image : :d_{top}= 250nm and d_{bottom} = 2000nm

Each deposited sample for the above configuration leads to eight cells fabricated under the same deposition and fabrication conditions. To optimise the performance through experimental methods, such 8 cells were fabricated and studied for each sample during our thesis. An illuminated JV curve of a preliminary cell is given in the figure 3.26. We can see that the cell has a low fill factor, a moderate J_{sc} value and high series resistance. To improve its performance, the following experiments were conducted :

1. **To optimise TRJ thickness:** tandem junctions of thickness combinations from 10nm to 30nm for each top and bottom were deposited and completed into solar cells, with constant top absorber 250nm and constant bottom absorber thickness.
2. **Current matching:** for absorber thickness optimisation cells were deposited with top cell thickness varying from 150nm to 275nm with 25 nm steps for 2000 nm bottom cell.
3. **To investigate the role of contact layers:** Tandem solar cells with bottom cell n layer thicknesses varying from 10 nm to 30 nm and top cell p layer thickness from 10nm to 25 nm with a step size of 5 nm were fabricated.

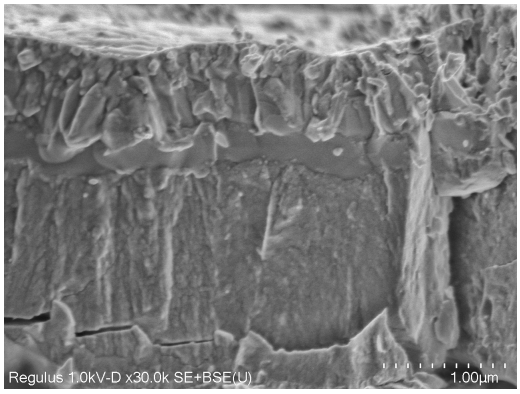

Figure 3.29: SEM image of a tandem cell after all processes. The resolution is low due to the low electron acceleration used. TCO on top.

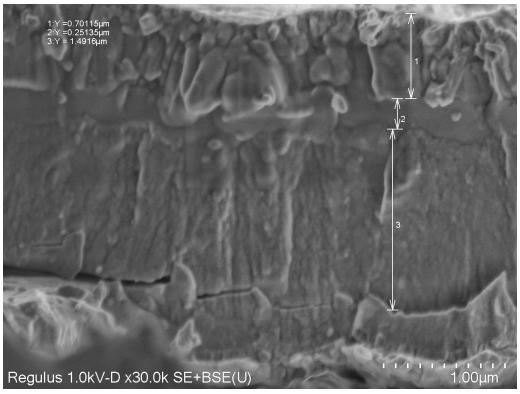

Figure 3.30: Measured thickness of tandem cell after all processes. The resolution is low due to low electron acceleration.

For instance, the resulting graphs from the TRJ thickness optimisation, the raw data for these studies are added as appendix F in this thesis. The results from the TRJ thickness experiment is plotted in figure 3.31 and 3.32. None of the cells fabricated had high performances as seen from the efficiency values plotted in 3.33. The best values for all parameters are obtained for one sample. But the fabricated cells have faced repeatability issues and electrical shunts. A majority of cells were *shunted* and thereby the data obtained from the cells could not give enough sample size to make solid conclusions. Thus the designed experiments could not provide a solid idea of the best combinations. The issues of these cells fabricated for different experiments

are investigated in section3.7.1.

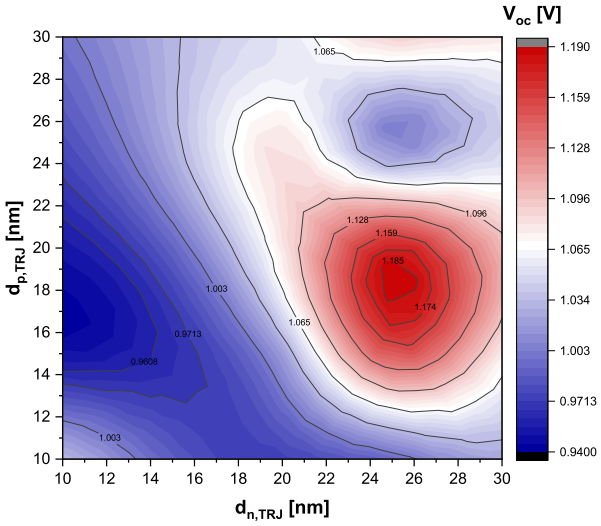

Figure 3.31: The V_{oc} plot for TRJ thickness combinations.

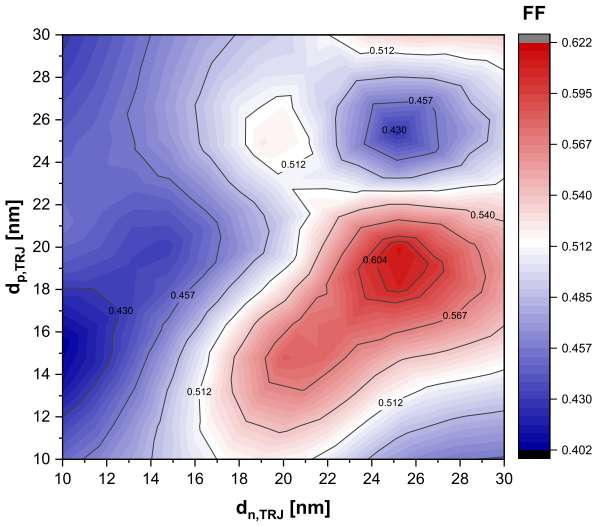

Figure 3.32: The FF plot for TRJ thickness combinations.

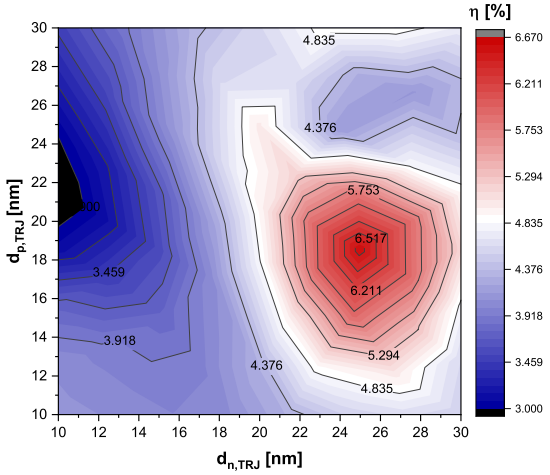

Figure 3.33: The efficiency plot for TRJ thickness combinations.

The fabricated cells with this deposited structure for all three experiments have resulted in a quite low percentage of cells that show *diode behaviour* and due to the large scatter in the experimental data, the above three designed experiments did not result in any conclusive results. This issue with yield is discussed from now on.

3.7.1. Yield

At this part of the thesis, we investigate the issue of low yield for micromorph depositions on aluminium. The deposition structure and procedures followed in cell finishing needs further studies. The final numbers resulting from previously discussed experiments are tabulated in the table 3.4.

The yield is less than 35% and the issue of shunts is prominent enough to hamper further studies and optimisations on this model. The observed shunts in the samples include localised shunting too in which the bottom subcell was seen as current leaking. As a part of the thesis nanocrystalline single-junction cells were also manufactured which turned out to be heavily defective. The cells measured under the light showed a very low V_{oc} as well as FF. These readings are entered in the table 3.5. These values of bottom $\mu c - Si:H$ subcells when added to typically observed a-Si:H subcell V_{oc} values in the range of 0.75 V to 0.85 V, roughly adds up to the observed poor performance tandem V_{oc} values. More than a coincidence this can be considered

Table 3.4: Resultant yield of initial experiments

Sample	No. of Samples	No. of Cells	Diode Behaviour	Yield [%]
Absorber combinations	18	104	25	25
TRJ combinations	22	176	56	32
Contact layer	9	72	21	29

as an indication of a defect prone bottom cell bringing down the performance of tandems. Similar studies by I.Lombardero *et.al.* [55] on multi junction modules with sub cell shunts issues also suggests that , these shunts are often evident at bias voltage corresponding to sum of all non defected cell V_{oc}s [55].

Table 3.5: The comparison of low-performance micromorph tandems and defective µcSi : H single-junction cells.

aSi:H/µcSi:H:H			µcSi:H:H		
V_{oc}[V]	J_{sc}[mA/cm^2]	FF	V_{oc}[V]	J_{sc}[mA/cm^2]	FF
0.89	7.43	0.349	0.151	10.56	0.301
0.95	10.09	0.402	0.163	8.49	0.284
0.936	9.77	0.384	0.212	9.5	0.323
0.813	9.66	0.353	0.181	9.68	0.32
0.906	9.84	0.398	0.214	11.08	0.343
0.811	9.83	0.339	0.209	10.98	0.34

3.7.2. Totally shunted cells

Completely shunted cells are easier to identify with the help of dark JV measurements. These cells are represented in the figure 3.35. On a linear scale, these cells deviate from the diode behavioural curve and tend to move towards the ohmic behaviour. The cells shown to represent this issue are three cells each from two different samples of the absorber combination experiment mentioned in 3.7. All three samples have poor behaviour in dark with the shunt resistance too low and thus affecting the performance of these cells.

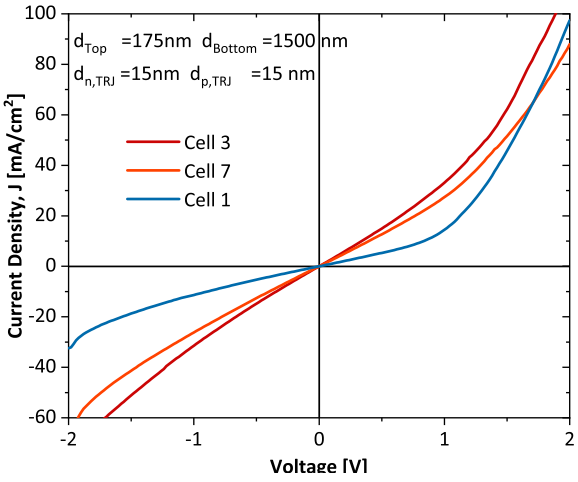

Figure 3.34: Dark JV characteristics shunted cells - linear scale.

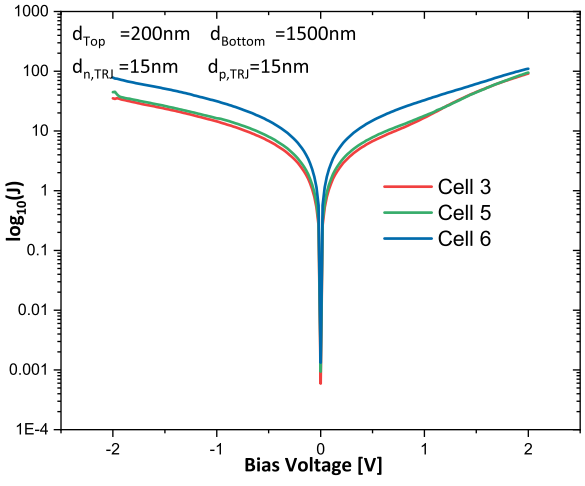

Figure 3.35: Dark JV characteristics of shunted cells : semi-log scale.

3.7.3. Partial (sub-cell) shunts

The basic thumb rules of identifying shunts from single-junction cells shall go wrong in analysing multi-junction solar cells if the cell is in partially shunted condition [55]. Partial or localised shunting can be observed when a subcell is current leaking. The variable intensity measurements (VIM)[56] of EQE can be used to identify the quality of electrical behaviour of subcells. The EQE readings are taken under no bias light, to test this for our cells. The no bias EQE has an expected very low response at a blue wavelength which will be limited by the bottom cell response. Also, it will take an approximated zero value in the IR region of the

spectrum where the cell is top subcell current limited. This results in an "intersection" profile for tandem solar cells ideally [57]. A similar profile of good micromorph tandem is shown in the figure 3.37.

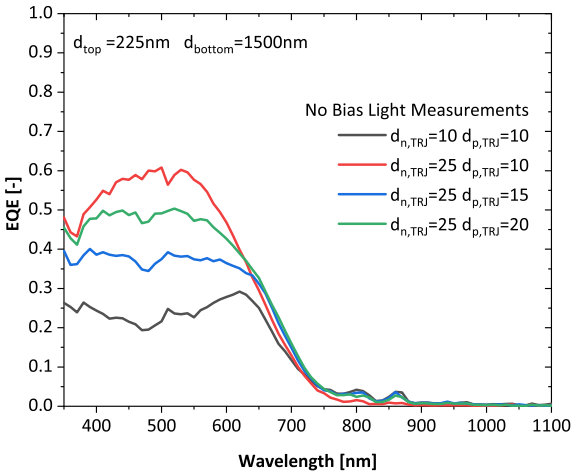

Figure 3.36: Observed EQE curve for the tandem samples at dark

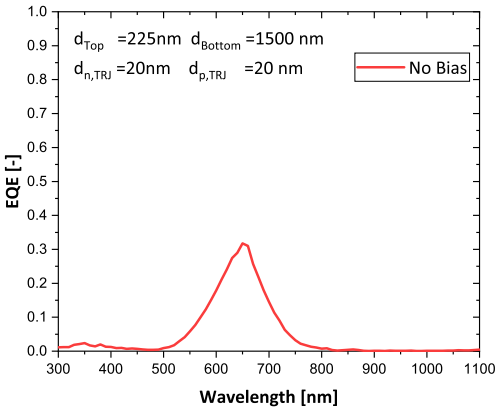

Figure 3.37: Desired EQE output at no bias light applied state

In the dark EQE plots shown in the figure 3.36, the response of the tandem cell in the blue region of the spectrum shall point towards a current leaking bottom cell, which means the µcSi:H subcell is of poor quality in this case. It can be noted from the graphs that the thickness of the p layer and n layer at TRJ is a determining factor for the current leakage, with an increase in p or n-doped layer the current leakage in the bottom cell is seen to increase. These kinds of shunts were reported previously for tandem micromorph cells by J. Löffler et al. which was tackled by introducing an n-doped double layer in TRJ, comprising of a-Si(n) and nc – SiO_x(n) layers [57]. But the deposition in such a case was nip-nip in contrast to our pin-pin order. Due to the time constraints of this work, the mentioned idea was not experimented on our micromorph tandems to study the intermediate a-Si(n) layer's effect on bottom cell shunts.

3.8. Total shunts - An investigation on scribes

Scribes are intended to isolate the active areas and define electrical circuits in the cell. The primary suspects of shunts in our structure are the scribes - the P1 and the P3, these cases shall be addressed here in this section.

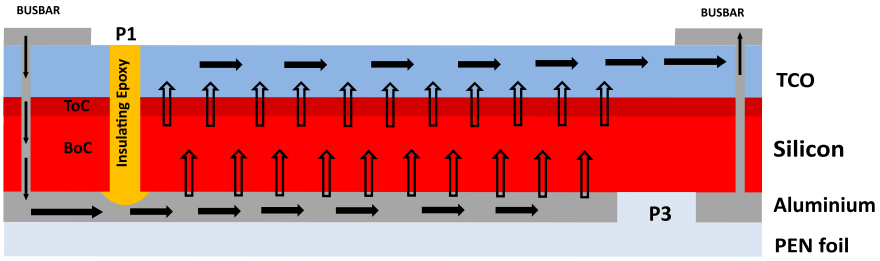

Figure 3.38: Ideal path for the flow of current

In the figure 3.38, the direction shown is the ideal electrical path that we expect in our fabricated cells. If the cell deviates from perfect scribes, it can result in two kinds of alternate electrically closed paths. *Case 1*: Issue at the back contact of the cell arising from P3 scribe. *Case 2*: Issue with P1 scribe an alternate path through TCO at the top of the cell. Both these cases are discussed in detail in the next two sections.

3.8.1. Case 1 : Partially opened scribe

For the P1 scribe, the laser scribing power used is not standardised for tandems and can result in a parallel electrical path in cases where the power used for scribing is not enough to fully open the deposited layers.

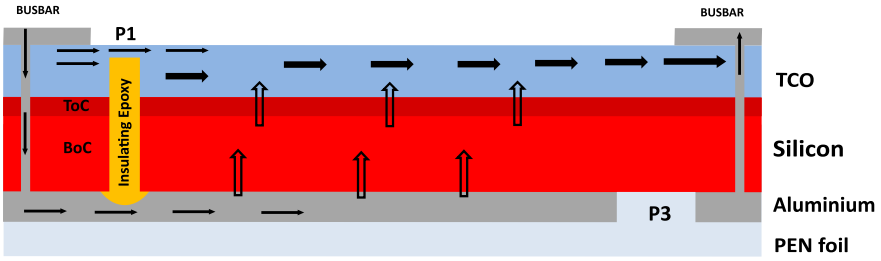

Figure 3.39: Possible alternate electric path if the P1 scribe is not completely open.

So, we designed an experiment to scrutinise the scribe openings. Instead of directly observing the epoxy filled scribe, we make an alternate scribe without ink on our sample. The sample considered for this experiment was with a top cell thickness of 200nm and a bottom cell thickness of 2000nm. This scribe without ink is over etched to remove the aluminium sputtered as back contact.

The sample was observed after this under a microscope. If the scribes are fully open, the back contact is completely removed through these scribes. This observed image with a backlight is given in the image 3.40. With backlight illumination, light passing through the scribe P1 means that the scribe is completely open and cannot cause shunts. Based on this, it can be concluded that for the shunted cells we considered, the laser power was enough to fully open the TCO. But the possibility of excess power and any possible issues cannot be ruled out using this experiment.

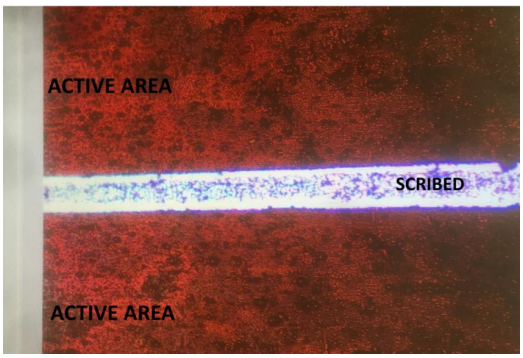

Figure 3.40: Laser scribe observed under microscope after aluminium removal.

3.8.2. Case 2 : Bypassing of the scribe

The hypothesis for defects associated with the P3 scribe is the possibility of bypassing the scribe gap, due to lateral conductivity of the deposited layer. This hypothesis is put under test in the upcoming sections. The P3 scribe is not laser-powered, but it is created using lift-off ink as mentioned in the section 3.5.5. The P3 has a gap of 35 microns. The desirable electrical circuit for our solar cell configuration and the alternate possible path is represented in the figures 3.38 and 3.41 respectively. Here the suspected lateral conductivity arises from the n-doped layer of the bottom cell which is very close to the AZO-Al bottom contact. The possible circuit diagram is shown with arrows in the image given.

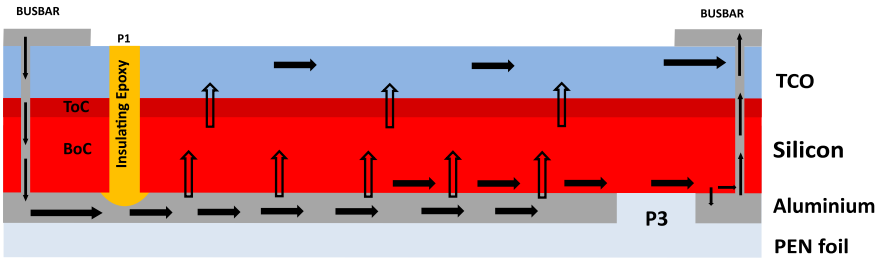

Figure 3.41: Possible parallel path for current flow in the cell with help of laterally conducting n-doped µcSi : O_x layer

3.9. Characterisation of n-doped layers

In order to verify this hypothesis, n-doped layers of nanocrystalline silicon oxide and amorphous silicon are put under test. The deposited tandems discussed up to this point has $\mu cSi:O_x$ as the n-doped layer of the bottom cell. This material shall be assessed for lateral conductivity to identify whether a parallel path for current is possible in our cells. The activation energy of the layer is measured using temperature-conductivity measurements. This is given by the relation,

$$\sigma(T) = \sigma_0(T)\exp\left(-\frac{E_a}{K_B T}\right) \tag{3.1}$$

3.9.1. n-doped $nc-SiO_x$

An n-doped $nc-SiO_x$ layer under the same conditions of n bottom cell were deposited on glass to measure the activation energy. The deposited layer had a thickness of 98.87nm as determined from ellipsometry. The linear fit of the data points from the graph results in activation energy of E_a = 60.9 meV. The activation energy value of 60.9 meV is too low and implies that the layer is laterally conductive enough to cause a parallel path across the P3 scribe. The P3 scribe has a gap of 35 microns across which this material can conduct. To see the alternative for this problem, the amorphous n layer E_a is measured.

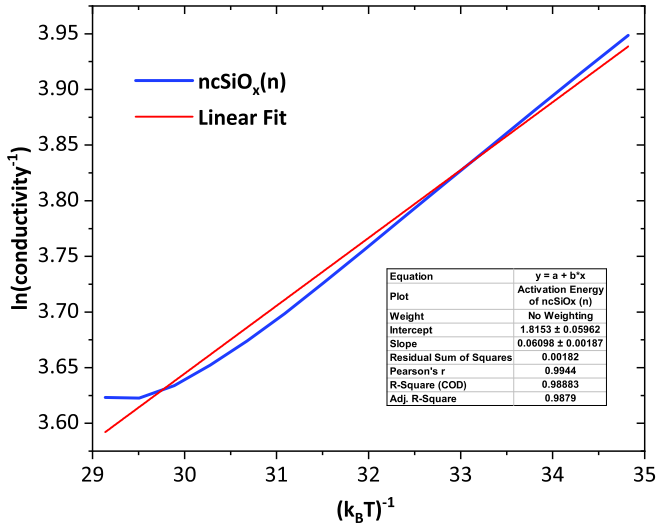

Figure 3.42: $\mu cSiO_x$(n) activation energy measurement

The n-doped $\mu cSiO_x$ layer is also present in the tandem recombination junction of our cells potentially causing lateral conduction in TRJ. The graph in the figure 3.36 which points to a leakage dependency on thicknesses (thereby a dependency on cross-section area) can also strengthen this hypothesis. This case is quite similar to the shunting issues observed with tandems when Zinc Oxide layers were used as intermediate reflectance layers.

3.9.2. n-doped $a-Si:H$

The deposition conditions for the a-Si:H(n) layer is as given in the table 3.1. The deposition was done on corning glass with a determined thickness (using ellipsometry) of 129.6 nm. The activation energy measurements were done on the same sample and conductivity was plotted against temperature as given in the figure 3.42. The linear fit for this graph had a slope of to obtain a value of 329 meV.

From this discussion, we conclude that the lateral conductivity of n layers can have an effect on the cell behaviour and can result in complete shunting of the cell. Also the activation energy values of $a-Si$ n-doped layers suggest that the material can be used as an alternative. In our model now we change the n-doped layers from $\mu c-SiO_x$ to $a-Si:H$ and investigate the yield.

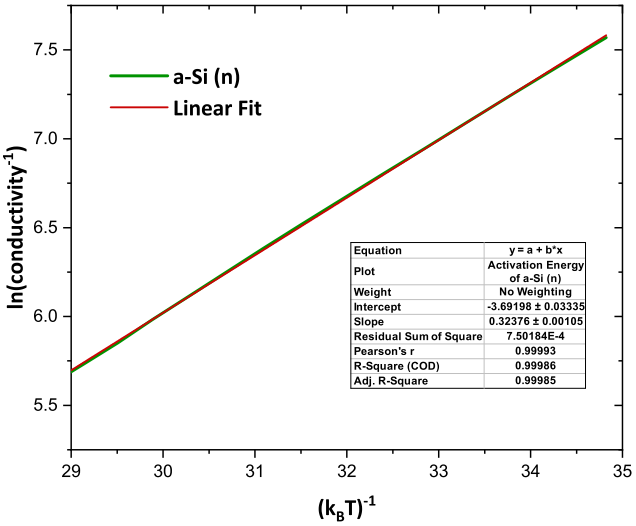

Figure 3.43: a-Si:H(n) activation energy measurement

3.10. Performance of tandem cells with a-Si(n) contact layer

With the observations of low activation energy of nc – SiO_x(n), new samples were fabricated using a – Si(n) as the substitute. The new version of processes mentioned in the section 3.5.10 was used for this.

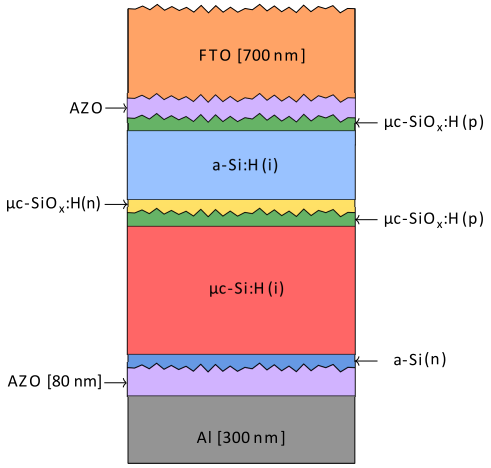

Figure 3.44: Tandem cell configuration with thick bottom n layer

The first deposited sample of these tandems had a – Si bottom n layer 80 nm thick. The depositions comprised top cell absorber = 200 nm, bottom cell absorber = 1500nm, TRJ thicknesses with n layer=20 nm and p layer=20 nm (refer to 3.44). Further Experiments on thin a-Si(n) bottom layers were conducted by reducing the thickness from 80nm to 40 nm and 30nm.

80 nm thick bottom cell n layer : Out of the 20 cells fabricated from the sample, 13 cells were not shunted and showing diode behaviour. Also, five of the samples were purely ohmic in nature and on close inspection it showed a mistake in placing the sputtering back contact masks and the back contact was in contact with the deposition aluminium foil edge. And thus in effect, the samples yielded 13/15 properly sputtered samples.

40 nm thick bottom cell n layer : Out of the 20 cells fabricated from the sample 16/20 cells were not shunted on dark measurement after sputtering.

30 nm thick bottom cell n layer : The sample with 30 nm thickness n layer for bottom cell, The dark JV

measurement is plotted in the below graph 3.45. For 80nm a-Si:H(n) we observe a high value of shunt resistance and thus the good cells. For a 40nm a-Si:H(n) cells We see a slight shift to the negative bias voltage compared to the other cell.

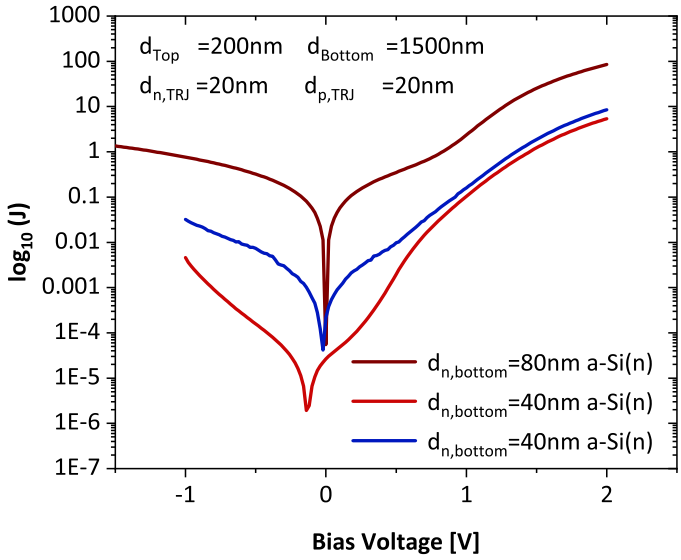

Figure 3.45: Dark curves of thick bottom cell n layer

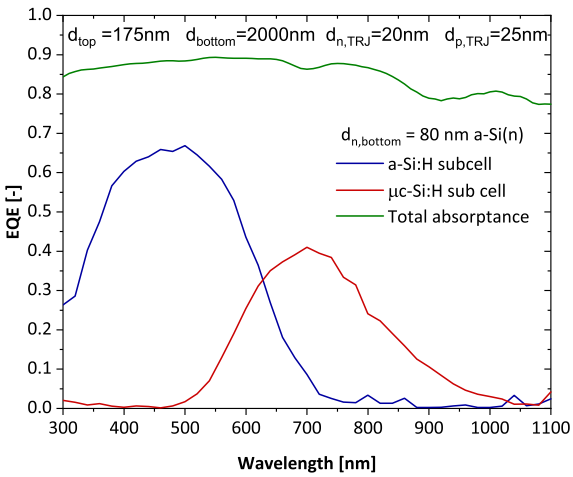

Figure 3.46: EQE cell 1 sample: 80nm thick bottom cell n layer

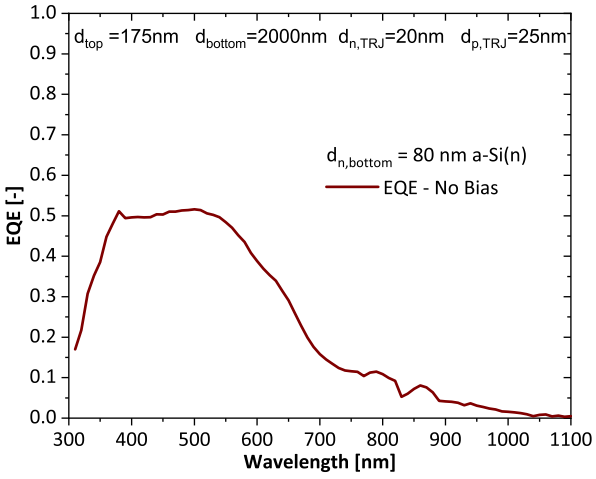

Figure 3.47: No bias EQE of cell #12 sample: 80nm thick bottom cell n layer

The figure 3.46 gives the spectral response of the micromorph tandem cells. Cell 7 and cell 12 of the same sample is observed to be partially shunted. Though the yield has improved, the change in the bottom n layer a-Si cell does not help to overcome the partial shunting issue of the samples. The graph in 3.49 represents the no bias light EQE measured of cell 12. This lays down the possibility of both good and partially shunted cells coexisting in the same sample

The absorption of the measured sample is plotted in green colour in the figure 3.46, the absorption shows a very high value in the case even in the IR side of the spectrum. This abnormality is investigated and the defects with the sputtering method are brought to the picture. A short description of this situation is in the following section.

3.10.1. Bottom sub cell with n-aSi:H layer

Since the bottom μcSi : H subcells fabricated at the initial part of the thesis showed a very poor yield and performance, we decided to test these parameters with t an n-doped a-Si layer of 40nm. This fabrication resulted in 2 diode behaviour cells out of the 20 sputtered. The EQE response of non shunted cells is recorded below.

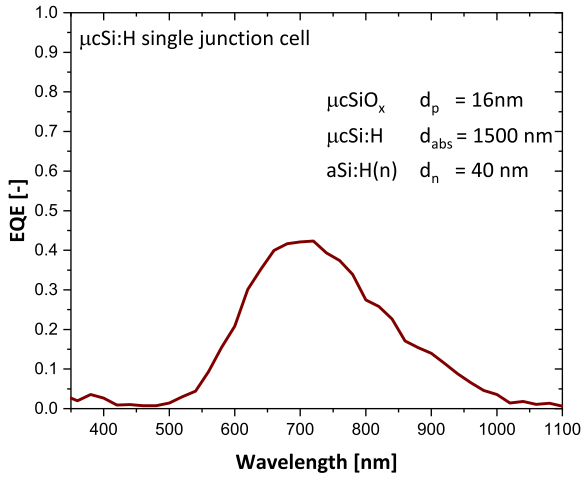

Figure 3.48: EQE of single junction μcSi : H cell, sample: 80nm thick bottom cell n layer

The EQE peak of 0.45 is quite low for a μcSi : H single-junction cells. This is again similar to the tandem solar cells bottom cell EQE in the preceding section. This shall again point towards the issue of sputtering as discussed in the next section 3.10.2. The a-Si(n) layer could not solve the yield issue with bottom subcells when fabricated separately.

3.10.2. Issue with sputtering

Magnetron sputtering of AZO and Aluminium is done on aluminium with TCO and adhered to PEN foil. As the next step, the aluminium is etched away and the sputtered layers are observed visually. The visual inspection shows a black deposition. The exceptionally high absorption values are attributed to the dirty black deposition of back contact. This can also be viewed as a reason for the low spectral response of the bottom cell as the back reflection from aluminium is not available for absorption in the solar cell. This unknown layer may be a reason for high series resistance also in these cells.

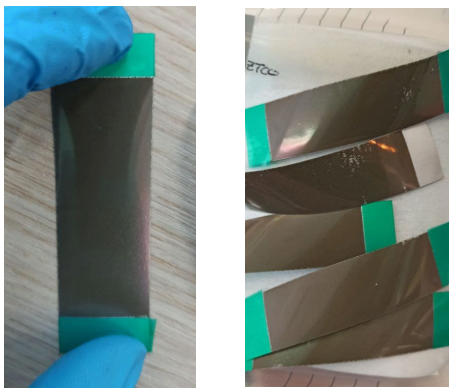

Figure 3.49: Sputtered layer with AZO observed black colour.

3.11. Potential issues and observations in the process

1. AMIGO depositions showed some irregularity in conditions when depositing the thick intrinsic bottom layers. The deposition in DPC 4 had intermediate stoppages from automatic plasma shutoffs. This might have had an effect on the thickness or growth of μcSi : H layer and performance of the cells.

2. Laser scattering with texture : For the cells with modulated texturing, special attention may be required for laser scribing. It shall be necessary to study the scattering properties in such scribing surfaces to avoid bruises along with the cut.

3. TCO additives : Upon visual inspection the TCO deposition irregularity on the temporary substrate is noticeable. Also on the final fabricated cell, this pattern is carried over and observed.

4. Positional Property : A trend with good cells or similar dark JV curves were noticed with adjacent positioned diodes. The image 3.50 shows the position and cell numbering convention for the samples. It shall be noted that for deposition #87*, The cells C2 C7 C8 C9 C12 C14 C19 and C20 resulted in non shunted cells. With deposited sample #94, the cells with diode properties reside with cells C2 C3 C7 C8 C13 C17 and C18. All these diodes are nearby positioned or in other words, exist on a straight line.

C1	C6	C11	C16
C2	C7	C12	C17
C3	C8	C13	C18
C4	C9	C14	C19
C5	C10	C15	C20

Figure 3.50: Cell positions in new version of lab scale cells.

5. Processing after deposition : The new version of cells allows measuring the dark properties at each stage of processing. And it was noticed that the cells get damaged during the final etching and temperature annealing of glue.

3.12. Outlook

Though the issue of total shunts in the cells was addressed, the subcell shunting in micromorph samples still prevails. A highly conductive n layer in the TRJ can also be a reason for this type of current leakage. The lateral conductivity of the n layer in TRJ may be affecting the FF value. As reported by J. Löffler et al.[57] the problem of localised shunts in the tandem configuration needs special attention with TRJ layers. Thus experiments with multiple TRJ layers and TRJ layer thicknesses in detail shall be a key to achieve good data sets and reproducible results.

The back contact sputtering of aluminium can have potentially a negative effect on the cell due to ion bombardment. Vacuum thermal deposition of Aluminium can be considered as an alternative.

A previous study conducted at Helianthos [13] has also demonstrated that the μcSi : H deposition on TCO directly is a challenging task and can result in defected cells, but at the same time when the same layer is grown on a-Si:H top cells in tandems, it is less defective. So the extremely low yield of μcSi : H single cells do not challenge the use of a-Si(n) layers as back contact n layers for good yields.

* Each of the samples deposited as a part of this thesis is given a number

4

Device Modelling & Performance Analysis

This chapter discusses the solar cell modelling and performance analysis on ASA. This chapter acquaints with the ASA software, via, its optical and electrical modelling aspects and introduces a new ASA automation plug-in *ASA Multi Run* aimed at enhanced user experience. This is discussed in section 4.3. Later in this chapter, we develop a micromorph model from calibrated single junctions. The concepts of performance enhancement are discussed in topics 4.10 to 4.13. Then we take a look at the impact of activation energy (4.14) and carbon dioxide flow (4.17)in the deposition of doped layers, on device performance. Finally, a performance analysis of the micromorph tandem model is done for out of standard testing conditions and an attempt to model the light soaking effect is presented.

4.1. Optical modelling

Optical solver is the primary solver platform of every simulation that forms the strong base of the software. ASA uses GenPro solver to find optical solutions and compute the optical response of the semiconductor. For the tasks in this thesis, ASA coupled with GenPro version 3 is used. GenPro3 solver is built upon GenPro1 and GenPro2 to aid ASA with a semi-coherent treatment of light and with the added advantage of handling textured interfaces [58]. GenPro4[59] is the latest and advanced solver which is superior to GenPro3, but to maintain the continuity of modelling study under FLAMINGO PV, this thesis uses the penultimate version. This thesis uses base models calibrated by E.M.Spaans [52] on the GenPro3-ASA platform in 2020.

The equations in the section 2.2are the basis of computing the photon absorption. Lambert-Beer law (equation: 2.4) governs the absorption of photons and Fresnel's equations (2.6 and 2.7) govern the interaction of the electromagnetic waves at the interfaces. GenPro 3 is equipped with the ability to handle the texturing of interfaces. Thus the input files for optical solving include refractive index data of the layers and surface profile height using atomic force microscopy (AFM). Since this approach takes the whole surface morphology into account, it outperforms the approach where the models only take RMS roughness [58]. At the interface, depending on the morphology of the surface, the reflected and transmitted components can be resolved into *specular* and *diffused*. The non scattered (specular) component continues in the same path as the incoming light wave and is considered *coherent*. Coherence of light means that the phases are maintained giving rise to interference fringes. From the rough morphology the amount of light diffused (scattered) give rise to out of phase waves - *incoherent* and thus does not result in interference fringes. In GenPro3 the scattered light amount, called *haze* and angular intensity distribution is calculated using scalar scattering theory[58].

4.2. Electrical modelling

In this section, we will have a short description of electrical modelling done by ASA. The section 4.2.1 introduces steady-state used for steady-state simulations of a-Si:H electrical simulations, followed by dangling bond and tail states' definition in ASA.

4.2.1. Semiconductor equations

The basic semiconductor equations for the electrical modelling constitutes the Poisson equation 4.1 and the continuity equations for the charges eq. 4.3, eq. 4.4[60].

$$\nabla \cdot (\varepsilon \nabla \Psi_{vac}) = -\rho, \tag{4.1}$$

where Ψ_{vac} is the vacuum level energy and ρ is the space charge density. This equation (Gauss Law) related the space charge density with the electric potential at a point due to this charge distribution. For the amorphous material, the value of ρ is given by

$$\rho = q\left(p - n + p_{\mathrm{loc}} - n_{\mathrm{loc}} + N_{\mathrm{d}}^{\mathrm{i}} - N_{\mathrm{a}}^{\mathrm{i}}\right) \tag{4.2}$$

where p_{loc} and n_{loc} are the localised hole and electron concentration and N_d^i,N_a^i the ion concentration of donor and acceptor respectively [61]. The continuity Equations represents the spatial conservation of charges in a steady-state condition. Numerically, the sum of generated and recombined charges is equal to the inflow and outflow of charges (represented by j) for the specific control volume[60].

$$\frac{\partial n}{\partial t} = \frac{1}{q}\nabla \cdot \vec{J}_n + G - R \tag{4.3}$$

$$\frac{\partial p}{\partial t} = -\frac{1}{q}\nabla \cdot \vec{J}_p + G - R, \tag{4.4}$$

For steady-state operations, the above equations 4.3 and 4.4 the time derivative equates to zero. Also, n,p are the electron and hole concentrations, t is the time, G is the generation rate, R is the recombination rate, $\vec{J}_p$ and $\vec{J}_n$ are the electron and hole current densities given by,

$$\begin{aligned} \vec{J}_n &= \mu_n n \nabla E_{fn} \\ \vec{J}_p &= \mu_p p \nabla E_{fp}, \end{aligned} \tag{4.5}$$

where E_{fn} and E_{fp} are the quasi-Fermi levels for electrons and holes, respectively. The equation set 4.5 in one dimension (X direction) can be written as 4.6.

$$\begin{aligned} J_{\mathrm{n}} &= qD_{\mathrm{n}}\frac{\mathrm{d}n}{\mathrm{d}x} + \mu_{\mathrm{n}} n\left[-q\frac{\mathrm{d}\phi}{\mathrm{d}x} - \frac{\mathrm{d}\chi}{\mathrm{d}x} - \frac{k_{\mathrm{B}}T}{N_{\mathrm{C}}}\frac{\mathrm{d}N_{\mathrm{C}}}{\mathrm{d}x}\right] \\ J_{\mathrm{p}} &= -qD_{\mathrm{p}}\frac{\mathrm{d}p}{\mathrm{d}x} + \mu_{\mathrm{p}} p\left[-q\frac{\mathrm{d}\phi}{\mathrm{d}x} - \frac{\mathrm{d}\left(\chi + E_{\mathrm{g}}\right)}{\mathrm{d}x} + \frac{k_{\mathrm{B}}T}{N_{\mathrm{V}}}\frac{\mathrm{d}N_{\mathrm{V}}}{\mathrm{d}x}\right] \end{aligned} \tag{4.6}$$

For the equation, the first term on the right-hand side representing the concentration gradient charge flow, the second term is the drift due to the electric field. The square bracket is the field across X-direction arising from potential ϕ, bandgap variation, the difference in effective density of states at bandgap energies for respective transport bands[60]. For detailed modelling principles used in ASA, the manual can be referred to [60].

4.2.2. Density of states

Tail states

Section 2.4 discusses the localized band tail states in amorphous materials (also refer to image 2.12). These states are single-electron states, meaning they are either occupied by one electron or remain unoccupied. Tail states near the conduction band exhibit acceptor like behaviour (unoccupied : neutral and occupied : negative) and their counterparts near the valance band shows donor like behaviour (unoccupied: positive and occupied: neutral). Valence band (VB) tail in a-Si:H is much broader than the conduction band(CB) tail and energies of the tail states in device grade a-Si:H are 45 meV for the VB tail and 30 meV for the CB tail typically [62].

Dangling Bonds : Standard Model and Defect pool Model

Defect states emerging from dangling bonds are *amphoteric* in nature. These are explained as positive when unoccupied, neutral when occupied by electron and negative when occupied by two electrons. For the distribution of dangling bond states models popularly used are the "standard model" and the "defect pool

model"[62].

The standard model assumes a Gaussian distribution for dangling states, given by equation 4.7

$$N_{db}^{+/0} = N_{db}\frac{1}{\sigma_{db}\sqrt{2\pi}}\exp\left(-\frac{\left(E-E_{db0}^{+/0}\right)^2}{2\sigma_{db}^2}\right) \tag{4.7}$$

where $N_{db}^{+/0}$ is the distribution of energy levels rising from $E^{+/0}$, N_{db} is the total dangling bond concentration of which $E^{+/0}$ are distributed around the peak level $E_{db0}^{+/0}$ with a standard deviation of the distribution σ_{db} [60].

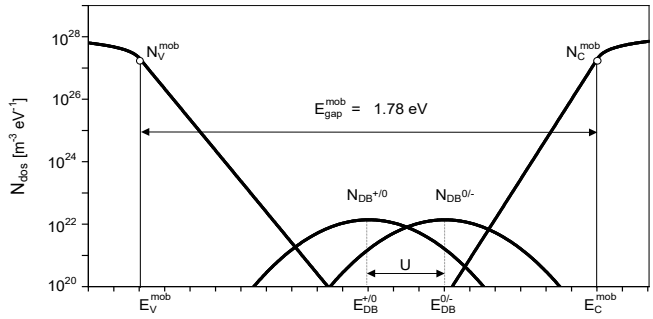

Figure 4.1: The standard model of the DOS distribution (logarithmic scale) in a-Si:H [60].

The defect pool model is an elaborate thermodynamic model which suggests the formation of dangling bonds by dissociation of weak Si-Si bonds. Different versions of the defect pool model exist, of which the Powell-Deane model (1993[63] and 1996[64]) is prominent. The central idea of this model is that occurrence and dangling bond concentration depend on the energy of formation of the dangling bonds[62].

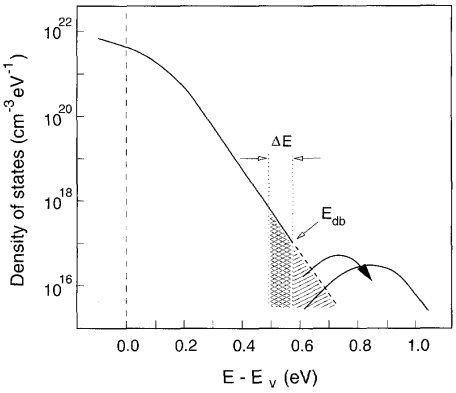

Figure 4.2: Schematic representation of weak bond to dangling bond transformation model.The hatched area marked E_{db} spontaneously decays to dangling bond. Adapted from [37]

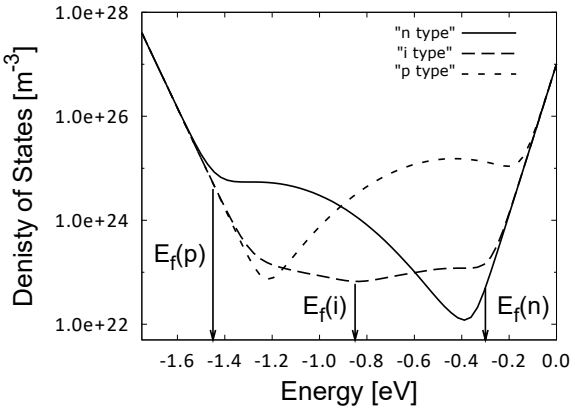

Figure 4.3: Defect-state distributions in a-Si:H according to the 1996 defect-pool model for three positions of the Fermi-level, close to the conduction-band (n-type), around mid-gap (i-type), and close to the valence-band (p-type). Inspired by [62]

4.2.3. Solver properties

For solving the electrical aspects of the model ASA solves Maxwell's equations eq.4.1 to eq.4.6 with boundary conditions at the limits of the electrical layers. ASA assumes a perfect collection of charges and ohmic contacts at the start and end of the defined grids. The finite element solving method is implemented with the help of newton or newton gummels iterative methods [60]. For more information on the solver properties and implementations, refer to the manual of ASA[60].

4.3. Plugin for ASA : ASA-Multi Run

In order to conduct a sensitivity analysis of a model and calibrate it against a real system, ASA needs many simulations with different parameters. Similar multiple changes of parameters and input files are needed to optimise the performance too. These changes are inevitable for the user and consume a large amount of time namely, input file change, verification of parameters and consolidating final outputs.

To decrease the manpower and intermediate time consumption thereby enhancing the user-friendly aspect, the automation plugin can play a vital role. A plug-in, also known as an *add-on* or *extension* is an external software or module that add new functionalities to the host program without altering the host program. As a part of this thesis to handle a heavy number of simulations, an extension is developed on Python named *ASA Multi-Run (AMR)* with the basic idea of omitting intermediate human interventions. ASA Multi-Run is based on the use of the ".exe" version of ASA rather than the website version. The website version of ASA for simulations was automated by E.M.Spaans named (*"Aut-ASA"*) as a part of the FLAMINGO PV project [52].

Algorithm : ASA Multi-Run (AMR) exploits the capability of Python to launch an executable from the python integrated development environments (IDEs)[65]. AMR uses the subprocess module in python to execute the "ASA.exe" file with a typical input file in text format. ASA Multi-Run algorithm is represented in the image 4.4. The algorithm omits repetitive editing of the input file and shell file making with the help of backup file creation and further replacement of the input with the same.
Input : A text format file with a *".cas"* extension is the typical input file for ASA. The cas input files are parsable in text format in python. To run ASA via AMR, the cas file is edited with two additional text lines at the beginning which facilitate a *polymorphic* condition. These lines are commented out with a "C" command from the C++ perspective (considering the current ASA version is built on C++), while it is treated as specific instructions by the plug-in to process. In this way, the same file can be used in the ASA web version, .exe version and AMR extension.
Output : The output of AMR includes a consolidated output file discussed more in the coming sections in .dat and .xls extension formats. This output file nomenclature is discussed in item 3 of the topic added features below. Along with this, the specified generated output files are saved in dedicated subdirectories.

4.3.1. AMR : Primary added features

ASA Multi-Run provides extra features for ASA users as already mentioned in the previous section, the main features available for AMR users are mentioned in this section. For a better understanding of these features from the description, a reference to Appendices A and B might be necessary.

1. Single Parameter : To change a single parameter over a range of values and execute them on ASA, AMR can be used. AMR takes this parameter as *parameter X* and saves the output with parameter value appended to the file name and folder name. These are applicable in the single variable analysis as in J_{sc} variation against absorber thickness.

2. Double Parameter Combinations : Double or multiple parameter combinations are particularly useful in analysing interdependent variables and their combined effect on external parameters. This facility of AMR is the most used type in this thesis namely, the tandem absorber combination optimisation and tandem recombination layer properties optimisation.

3. Consolidated Final Output : AMR merges the concept of text file handling and pandas *data frame* [66] to consolidate the illuminated solar parameter data from the ASA "solpar" output file. The plug-in keeps updating a master file with the external parameters and exports it as a final step of the execution. The facility of AMR is the most helpful for users in cases of a large number of outputs. The data is exported in both excel and *.dat* format taking into consideration Windows and Linux operating systems.

4.3.2. AMR : Subsidiary features

Apart from the features mentioned in the above section AMR adds some subsidiary features also as stated below.

1. Naming the execution : Each set of executions has the option to be named. This feature was included to identify the output files and to name the folders.

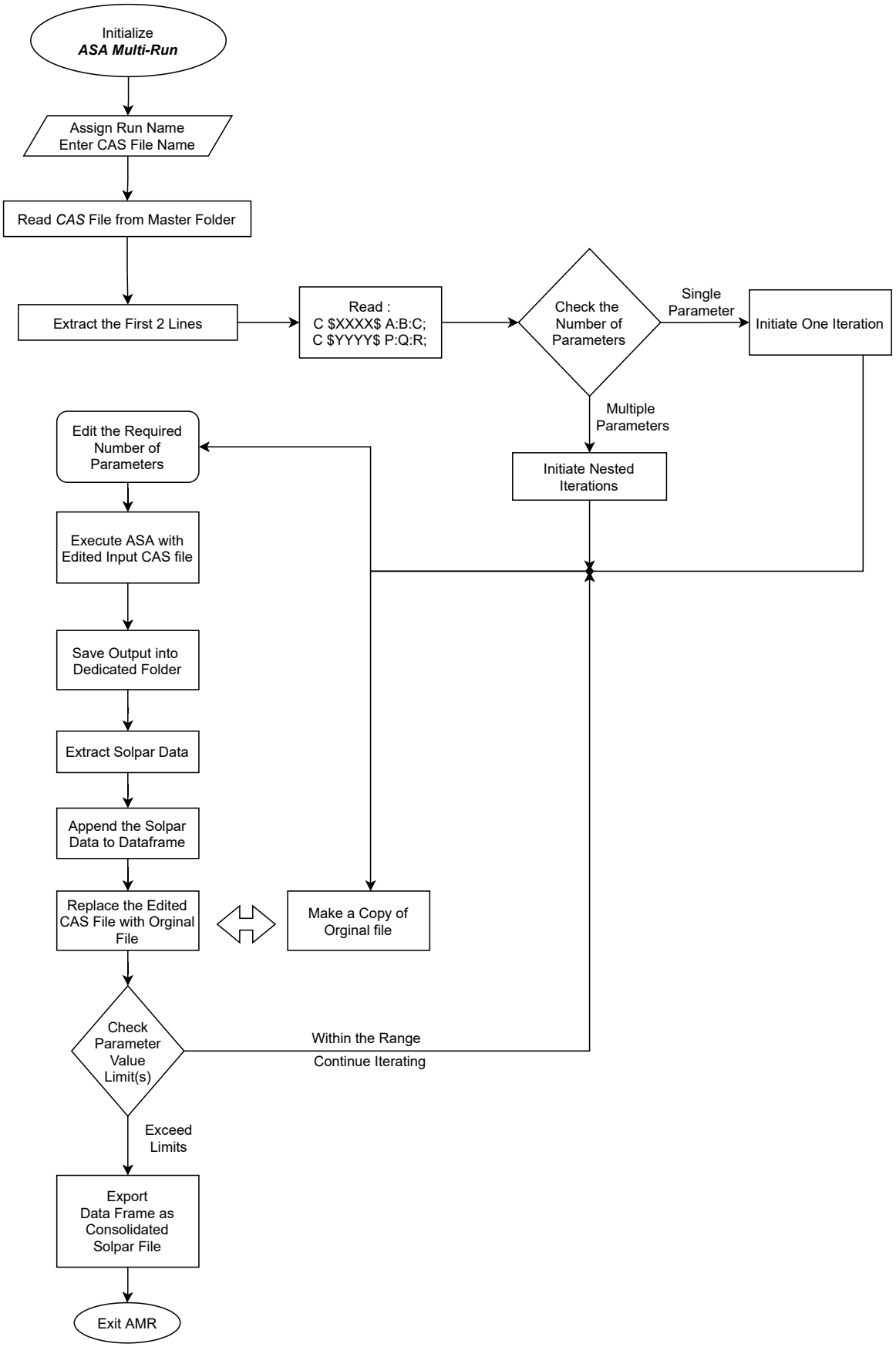

Figure 4.4: ASA Multi-Run algorithm flow chart.

2. Dedicated folder creation : The output files corresponding to each run is saved under a dedicated folder, identifiable with the run name and parameter value. If the ASA is run without any iteration and in normal mode, the folder is made in the given run name and date and time values.

3. ASA output files with dedicated names : The output files are given names with the parameter value. These files are directed to dedicated folders as mentioned above. These file names have identifications as *parameter X* and *parameter Y* suffixed to the names in order and shall be used for identification.

The plugin is added in the appendix A The above features were put to good use throughout this thesis work and an example of an edited ASA Multi-Run input file is added in Appendix B.

4.3.3. Errors and limitations

1. The float point error in python is considered a serious issue when working with modelling sensitive devices like solar cells. This computational error usually pops up on handling decimal values and is tried to be addressed in the plugin with a simple round off method and is expected to omit this issue from the majority of the cases.

2. The add-on is limited to variations in numerical parameters inside cas file. This is because of increment evaluation happening inside the plug-in. Thus it cannot handle a specific number of string changes in the cas file one after the other.

3. AMR consumes more of system memory compared to ASA simulation as the extracted values are stored in RAM before writing to an excel sheet.

4. The back end of the plugin utilizes multiple nested loops to parse through the cas file which can make the file handling slow.

5. The AMR plugin essentially needs to be in the same directory as the working directory, this decreases the ease of use and can be worked upon in the future versions.

4.3.4. Computational time

AMR takes negligibly small additional computational time than ASA. The simulation time of a textured tandem model used in this thesis is about 5 minutes and 40 seconds, which shall be the same in AMR. The time saved is in editing the polymorphic command lines consuming approximately 30 seconds on contrast might require 30 seconds for one cas file creation. Thus for 100 dual-parameter combination inputs (e.g., top cell thickness- bottom absorber thickness combination) , AMR consumes the same 30 seconds, but on the contrary ASA, file editing might take 100 times the same time. Usage of shell files and Aut-ASA[52] are the existing methods for multiple runs on ASA without human interaction, but the method requires the creation of individual cas files before making the shell. Thus ASA Multi-Run evidently holds superiority over the other methods.

4.4. Modelling of single-junction devices

This section presents the ASA thin-film modelling of single-junction cells. At this end, we discuss the calibrated models used for this purpose, changes to these models and behaviour, which leads to the building of tandem from these subcells. The descriptions are followed by the recombination junction modelling an integral part of tandems.

4.4.1. Calibrated models

For the study on micromorph cells, basic individual cells structure is formed from models calibrated by Spaans[52] as a part of the Flamingo PV project. The top cell is calibrated against the HyET single-junction a-Si:H absorber with p-doped a:SiC and n-doped a-Si:H as the top and bottom layers respectively of the p-i-n cell. The structure is shown in the figure 4.5 and the calibrated parameters of JV are represented in the figure 4.7. The bottom cell model is validated against a μc-Si:H reference cell developed by H.tan et al.[53]. The structure is shown in the figure 4.6 and its calibrated JV curve in the image 4.8.

To use the models in tandem micromorph cells, μc-Si:H subcell is given three changes :

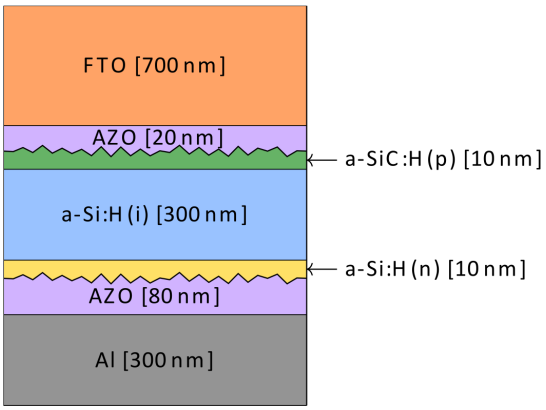

Figure 4.5: The HyET model used as base for calibration on ASA.Thicknesses are not to scale.

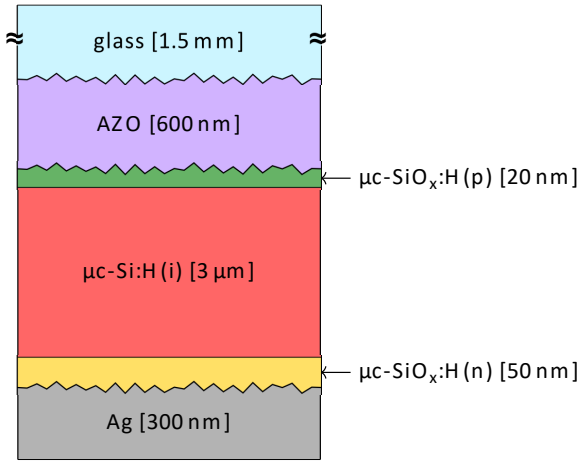

Figure 4.6: bottom cell model validated against a µc-Si:H reference cell developed by H.tan et al.[53]. Thicknesses are not to scale.

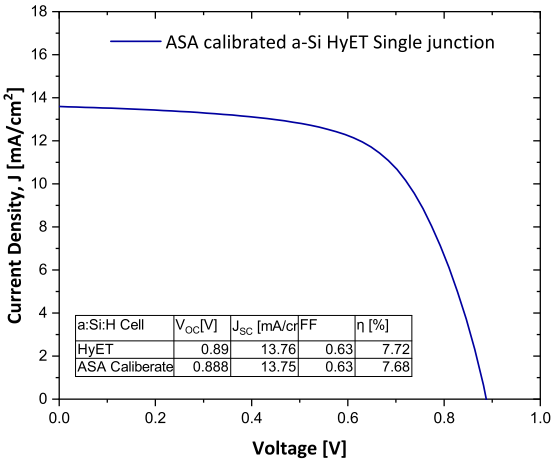

Figure 4.7: Illuminated JV curve of top cell simulated on ASA.

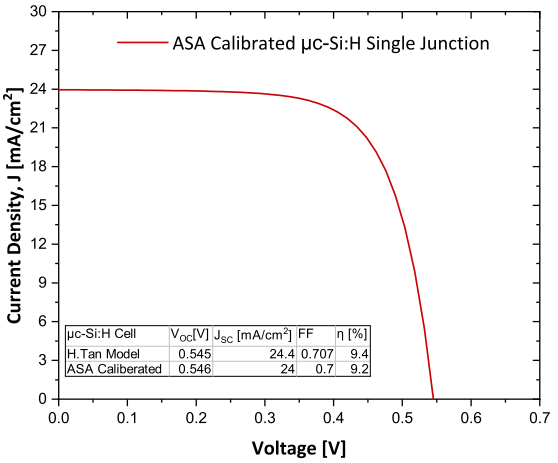

Figure 4.8: Illuminated JV curve of bottom cell simulated on ASA

1. The absorber layer is changed from 3 µm to 2 µm. The n layer thickness is reduced to 20 nm from 50 nm of the microcrystalline single junction. These alterations are done to maintain consistency with the absorber and bottom layers manufactured in HyET. The absorber layer thickness constraint of 2 µm is discussed in the section 4.8.

2. The µc-Si:H single-junction cells have modulated surface texturing on glass for efficient light scattering [53]. This texturing is different from the texturing used in our model which is FLAM 01. For this reason, the model texture is changed to FLAM01.

3. The back reflection is a result of a silver layer in Tan's model [53], but this is changed in our case and replaced with back contact and reflector material as Aluminium. This model with the changes are presented in figure 4.10.

Similarly, the HyET module structure is altered in two different aspects

1. The p-doped and n-doped layers of the cell is changed. p-doped a:SiC layer in the model is changed to p-µcSi : O_x layer and n a-Si:H layer is replaced with n-µcSi : O_x layer. These changes in layers are done from the calibrated p,n-doped layers of the microcrystalline model.

2. The a-Si:H single-junction cells have baseline texturing used in the industry, but the texturing of FLAMINGO tandem model is FLAM01, and correspondingly changed in the model too.

The illuminated JV curve results are :
The HyET model with mentioned changes is represented in the figure 4.9 and the simulated JV curve in 4.11.

The Voc of the model shows a fall, which is an effect of p-doped and n-doped layer thicknesses at the same time the model has a higher fill factor and inturn higher efficiency from improved band bending attained using the µcSi : O_x layers. It can be viewed that the model shows a slight increase in J_{sc} because of a change in texture. Although FLAM01 is better than the baseline texture, it shall be noted that this texturing is particularly effective in scattering higher wavelengths of the spectrum. Thus the J_{sc} change can be viewed as a combined effect of FLAM01 and parasitic absorption of doped layers.

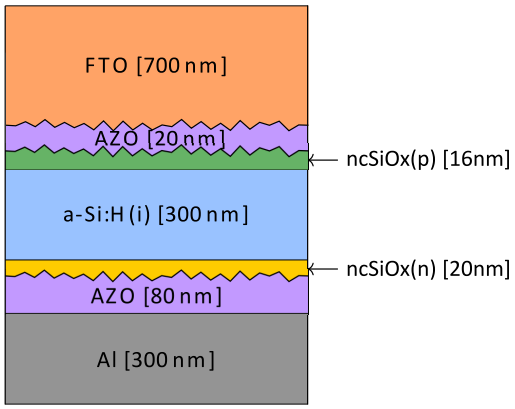

Figure 4.9: Structure of a-Si:H cell with texturing and p,n layer changes. Thicknesses are not to scale.

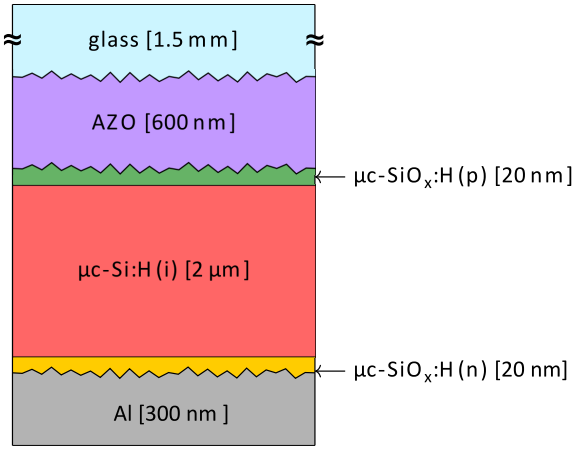

Figure 4.10: Structure of nc-Si:H cell with texturing and n layer thickness change.Thicknesses are not to scale.

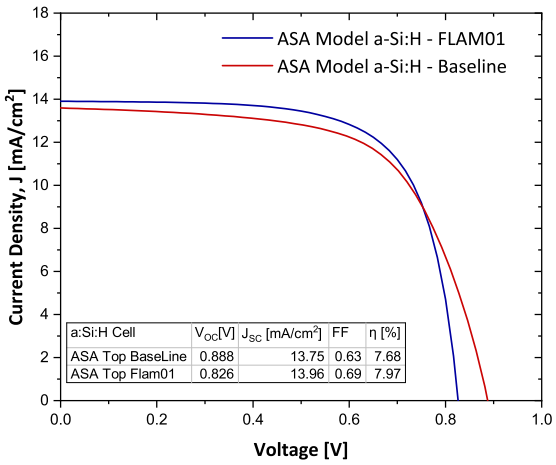

Figure 4.11: ASA simulation illuminated JV curves for for changes in a-Si:H single junctions.

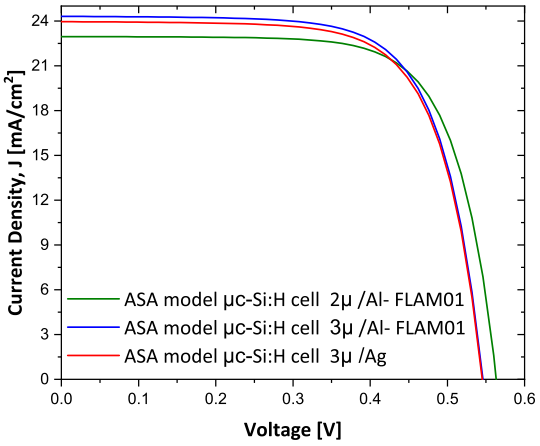

Figure 4.12: ASA simulation illuminated JV curves for for changes in ncSi:H single junctions.

The J-V curve changes for the model for a bottom reflector is as shown in the image 4.12. The base model presented in the above section is represented by a red line. The altered model with FLAM01 and aluminium back reflector is shown in the green graph. With the same thickness, a similar J_{sc} is attained with FLAM01. The thickness of 3 microns is sufficient enough to absorb a large fraction of the available light and also it can be noticed as the reduction in absorbance due to reflection is compensated by the enhanced scattering by FLAM01. The thickness is reduced to 2 microns in the next step with a reduction in J_{sc} value but a very slight increase in the V_{oc} due to a reduction in recombination losses with a one-third decreased thickness.

4.5. Modelling of TRJ

The identified challenge with modelling of tunnelling junction is that the probability of tunnelling through a potential well is dependent on non-local properties.*Delft Model* is used to model the tandem recombination

junction. This uses the trap assisted tunnelling (TAT)[67] combined with the Field Dependent Mobility Enhancement (FDME) Model[39] thus applying an enhanced carrier transport in the high-field region of the TRJ.

The TAT model enhances the tunnelling making it field-dependent, introducing a new parameter named effective tunnelling mass. The model is an extension of the Shockley-Read-Hall model. The TAT model in the absence of an electric field is the same as SRH[67]. According to M. Zeman et.al.,TAT accounts for the high recombination for high-field regions but at the same time, it fails to account for the tunnelling transport through the localised states towards the recombination sites. For this purpose, the Delft model introduces effectively extended state mobility of electrons and holes in high electric field regions [39].

4.6. External quantum efficiency simulations

The EQE measurements of tandem cells as mentioned in this thesis requires a bias light choice in simulations as well, but once simulated the measurement is computationally challenging and shows a high amount of discrepancies based on the bias light. It is also the case that to do this, the model needs to be given a bias voltage depending on the light biased cell for a good approximation. As a solution for this condition, the approach used in this simulation is electrical isolation of subcells simultaneously keeping the subcells optically coupled for the simulations.

For EQE bottom cell measurement, the top cell in the model is considered only optical. Then the generated charge carriers are collected exclusively from the bottom p-i-n layers, which means the simulated output is the bottom cell spectral response values. This same idea is implemented for top cell EQE also. The same method can be used to approximate the subcell J_{sc} values too with negligible or no variations[52].

4.7. Simulation result of a-Si:H/μc-Si:H tandem solar cell

This section describes the tandem model built from the above-calibrated model and the discussed changes. The primary work on a-Si:H/μc-Si:H tandem solar cell under the FLAMINGO PV project was done in 2020 [49] [52]. This model presented here holds changes from the previous studies (as already represented) in the section 4.4.1.Thus, a better band bending possibility for top cell, realistic tandem recombination junction, conformal FLAM01 texturing is assigned to the device interfaces. This model forms the basis of further studies presented in this thesis.

4.8. Simulation structure

The material layers considered are the same as the initial fabricated model mentioned in the section 3.5.The model is represented schematically in the figure 4.45. ASA-GP3 simulations predict possible improvements for the basic model in the later stages of this thesis. The primary elements of our model are :

1. *Encapsulant layers:* The encapsulant layers used for the solar cells are formed as two layers each of ETFE and glue. The layers are treated as non-absorptive with k=0. ETFE has a refractive index value of 1.43. The glue layers between two ETFE layers are 80μm possessing a refractive index of 1.53. The second glue layer which adheres to the TCO and ETFE is 75μm thick with a refractive index of 1.47. These layers apart from their primary objective of protection also help in efficient light management by reducing the reflection of light at the front of the cell. This idea is discussed in detail in section 4.9

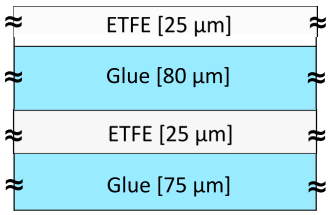

Figure 4.13: Structure of the front encapsulation used by HyET Solar. Thicknesses are not to scale.

2. *Absorber thickness:* The absorber thicknesses of simulated models are optimised in the further sections. But the main point of interest is the combination where the bottom cell thickness is below 2μm thick.

This limitation of thickness is brought forward based on the capacity of the machines and economics at HyET solar. To maintain a high throughput 2-micron thickness is the maximum value that can be deposited by the machine. This constrain is also aimed at limiting the production costs of solar cells.

3. *Back reflector:* The back reflectors used in HyET is aluminium with 300nm thickness. Refer to the discussion under the topic 3.5.5. Further improvements in the optical side of the device are possible using silver as the back contact, but the feasibility of using a noble metal like silver in solar cells lies in the benefit it offers against increased material costs.

4. *Texturing:* The texturing used is FLAM01 aiming at enhanced scattering in the red wavelength region of the spectrum as demonstrated by D.Rajagopal[49], for a detailed comparison between FLAM01 and baseline texturing refer to the work (optical analysis with GenPro4) done by D.Rajagopal as a part of Flamingo PV in 2020.

5. *TRJ:* A tunnel-recombination junction will form at the union of the two sub-cells between n-μcSi : O_x and p-μcSi : O_x. The modelling of such a junction is overviewed in the section 4.5.

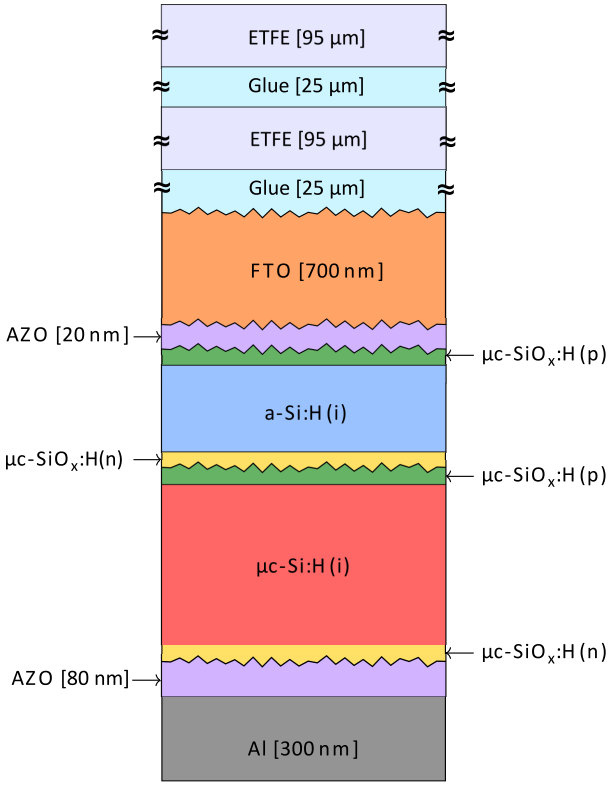

Figure 4.14: The micromorph tandem solar cell structure simulated on ASA. with encapsulation. NB: The thicknesses are not to scale

The refractive index data of these layers are given in appendix G.

4.9. Device performance

In this section, we shall discuss the device performance of micromorph tandem cells based on the model introduced in the preceding section. As a step by step procedure, models without any encapsulation is studied initially and encapsulation is introduced in later stages. The simulation for micromorph tandems with amorphous silicon absorber thickness of 300nm and the bottom cell thickness of 2000nm is done and the graph is plotted in the figure 4.15. The summary of these plots is tabulated 4.1. From this table, it can be noticed that the tandem is bottom cell current limited in nature.

Now the cell with encapsulation can be focused upon. The JV of encapsulated model for unchanged absorber thicknesses is represented in 4.16. The cell is integrated with FLAM01 texture. The encapsulated

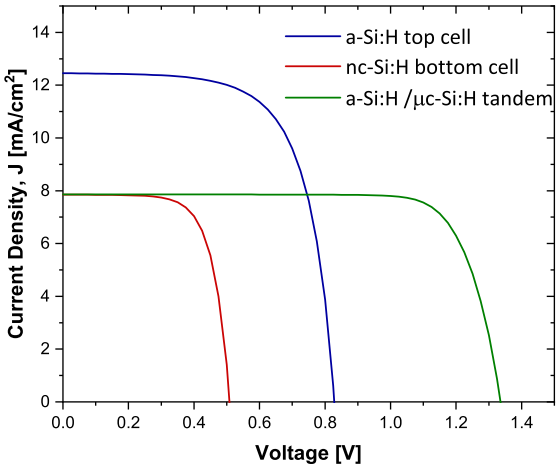

Figure 4.15: Device performance of micromorph solar cell with top cell 300nm and bottom cell 2 microns thick.

Table 4.1: External parameters of base tandem model

	Thickness [nm]	J_{sc} $[mA/cm^2]$	V_{oc} [V]	FF [-]
a-Si:H sub cell	300	12.45	0.828	0.67
µc-Si:H sub cell	2000	7.85	0.508	0.71
aSi/µc-Si:H Tandem		7.86	1.336	0.79

model shows an approximate increase in J_{sc} by 5.9%. The spectral response of the top cells shows an evident increase for which the reason can be attributed to a decrease in reflection due to better coupling of refractive indexes. Refer to the graph in figure 4.17 which plots photon absorption and EQE for both cases. We can notice an advantage in both these measurements for encapsulated cases over the non-encapsulated cells. The appearance of fringes in the encapsulated case also suggests that to model the real case, the ETFE layer shall be employed as incoherent.

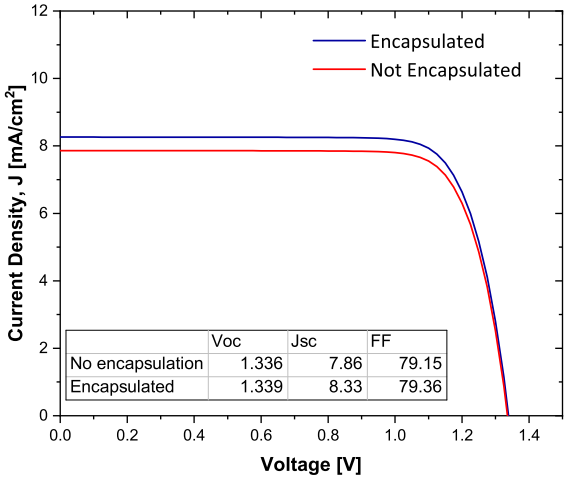

Figure 4.16: Illuminated JV comparison of encapsulated and non encapsulated tandem cells.

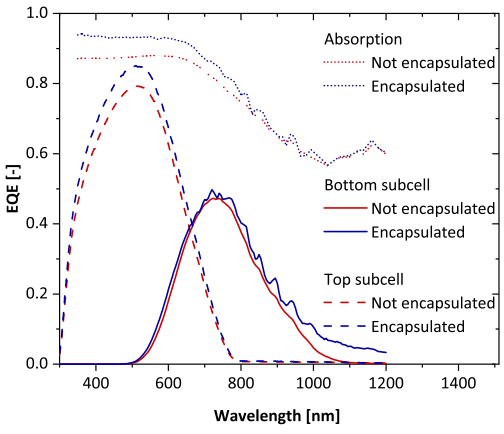

Figure 4.17: EQE/ Absorptance comparison of encapsulated and non encapsulated tandem cells.

Similar to the unencapsulated case, these results also suggest that the tandem cell with a-Si subcell thickness of 300nm is bottom cell limited and essentially requires current matching. This study on thickness optimisation is presented next.

4.10. Absorber thickness optimisation

For optimising the absorber to attain the current matching condition, combinations of a-Si:H and µc-Si:H thicknesses are studied. The top cell absorber thickness is varied from 100 nm to 300 nm with a step size of 10nm and the bottom cell absorber thickness is varied over 1000 to 2500 nm range with a step size of 50nm. Contour plots are made for each external parameter against the thickness combinations. Complete results are given in the appendix C.

The current mismatch simulation result is shown in the graph 4.18. The top subcell current minus the bottom subcell current value is plotted. The white shaded region demarcates the current matching region. Right of the slanting white line - the red shaded combinations represent bottom cell limited tandem cells and the blue region is the top cell limited area. The plot suggests that increasing the thickness of the limiting cell or decreasing the thickness of the counterpart can lead to a matching condition. A bottom cell thickness of 2 microns is of special interest throughout the study due to the aforementioned reasons (topic 4.8). With this idea, it can be observed that at a top cell thickness of 156 nm the current mismatch approximately takes a null value and gives the optimum performance in terms of short circuit current.

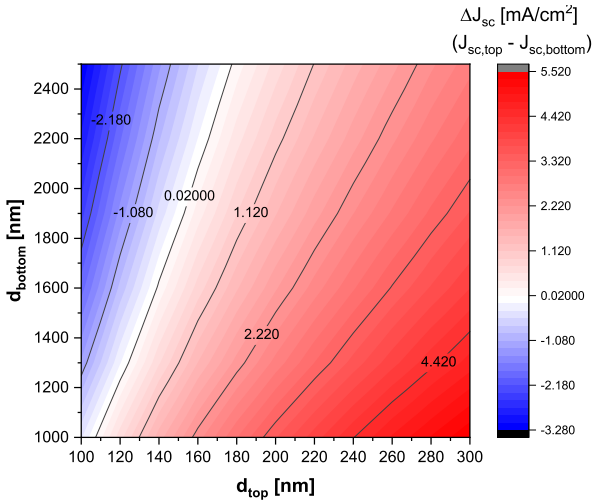

Figure 4.18: Current mismatch between top and bottom subcells for various absorber thickness combinations.

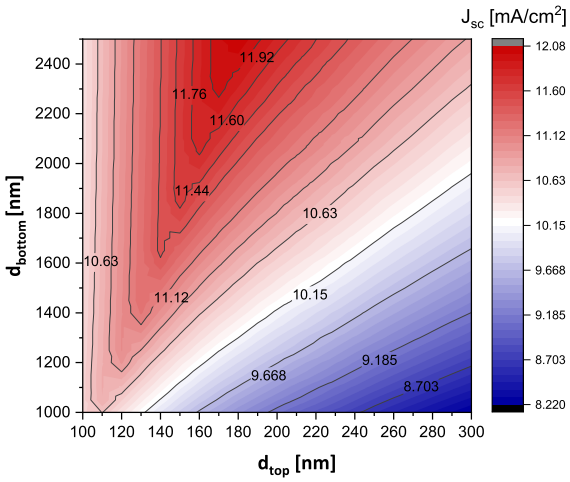

Figure 4.19: Short circuit current for various absorber thickness combinations.

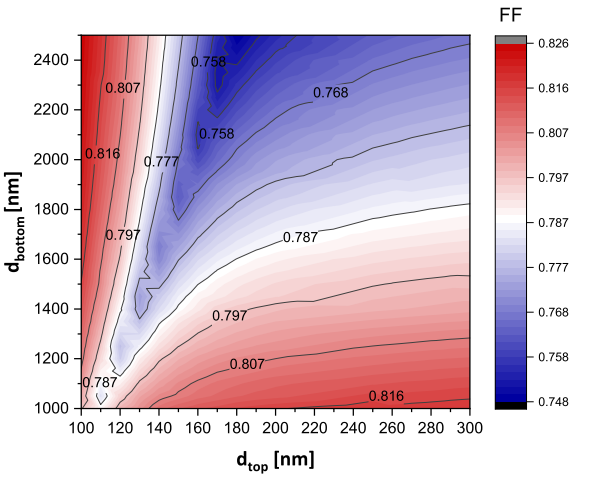

Figure 4.20: Fill factor variation for various absorber thickness combinations.

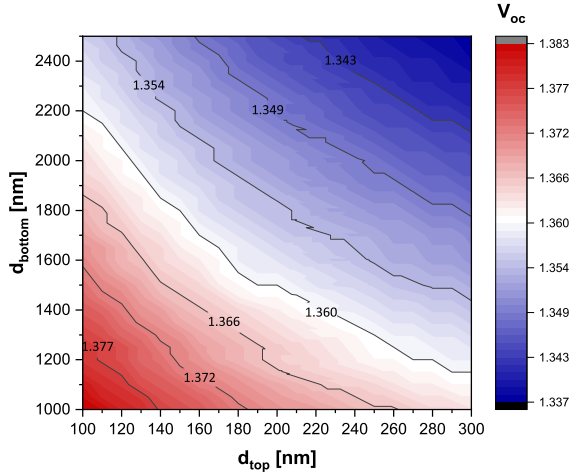

Figure 4.21: Open circuit voltage variation for various absorber thickness combinations.

The simulation results of the fill factor also follow the same trend as J_{sc}. The V-shaped peak value PROFILES observed with short circuit current change to a minimum value in Fill factor. The change in the shape of contour lines between the top cell limited region and bottom cell limited region is evident. For the bottom cell limiting range,the fill factor is more dependent on the change in thickness of the top cell, as indicated by the vertical contour lines. Following a similar trend,the contours on top cell limiting combinations show a near-horizontal characteristic suggesting that the FF change is responsive to bottom subcell absorber thickness. These trends arise from the current mismatch leading to a sharper "knee" in the JV curve.

This trend in V_{oc} is the same as observed in experiments. The plot in the figure 4.21 shows the open-circuit voltage trend over the thickness combinations. The thinner cells give higher V_{oc} due to reduced recombinations. Over the considered thickness ranges an overall difference of 40 mV is recorded. Which is quite a significant value, but the contour line trends to be equally responsive to both top and bottom subcell thickness variation.

4.11. TRJ thickness and doping optimisation

TRJ performance is very important in a tandem solar cell from both optical and electrical perspectives. The absorption in this layer is considered parasitic and directly proportional to thickness. The refractive data of these layers become significant when the layers can act as an intermediate reflecting layer, giving rise to light utilisation for top cells. This idea is addressed in 4.17. On the electrical side, ideal recombination junction performance is assured when recombinations happen via tunnelling when the bands for tunnelling are close by. This section primarily considers the electrical aspects of the junction in terms of thickness and doping.

4.11.1. TRJ thickness combination

TRJ thickness simulations for the model are done by varying both the n-layer and p-layer thickness from 10 nm to 35 nm. Fill factor and J_{sc} are studied with the help of contour plots. In ASA the illuminated JV simulations are done with a step size of 1 mV to increase the accuracy.

The illuminated JV curves plotted for different thickness combinations of TRJ in the image 4.22 implies two ideas. Firstly, the FF value diminishes with increasing thickness. Secondly, the J_{sc} value of the curve with the highest FF need not be the best. Thus we shall now have a look at the FF and J_{sc} with different combinations of TRJ thicknesses and analyse them with the help of contour plots.

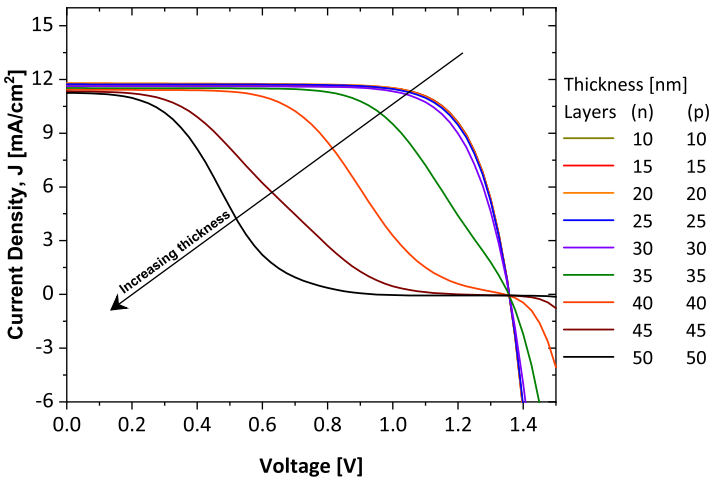

Figure 4.22: JV curves for different TRJ thickness combinations on ASA.
NB: Order of legend in the order of arrow direction

The series of combinations that were studied are results for these simulations are plotted in images 4.23 and 4.24. The change in n thickness from 10nm to 30 nm marks a difference of 2% in Fill factor for p layer

thickness below 25nm. Though we have used the smallest possible voltage step on ASA (1mV) yet it remains a fact that ASA uses an algorithm for interpolation to find maximum power point (MPP) and thereby arrive at the fill factor value. For this reason, the variations (not values) in the " region of mild variation " shall fall into the low confidence category. But as the p-layer thickness is varied above this value, the FF drops rapidly from 75% to 60%. In this region, the FF trend is roughly the same over n-µcSi : O_x value change. Here the FF versus thickness combinations also shows a little prominence for n layer fluctuation than p layer which shall be attributed to the DDOS value of n being higher than the p in calibrated model. (Refer to Appendix B dbond[3] n = 1.0e24 and dbond[4] n = 1.0e23 command).

The J_{sc} plot corresponding to the TRJ thickness combinations shows that the thicknesses of the layers should not be extremely thin or extremely thick for favourable J_{sc} values. Very thick layers shall result in recombination in the layers, and thin TRJ layers shall lead to the lesser opportunity of tunnelled recombination in the layers. The contour plot shows the blue shaded region towards high thickness values for both the doped layers marking a significant increase in parasitic absorption for the layers. The prominence in the effect of n layers in this shall be due to the structure of the cell with n stacked over p.

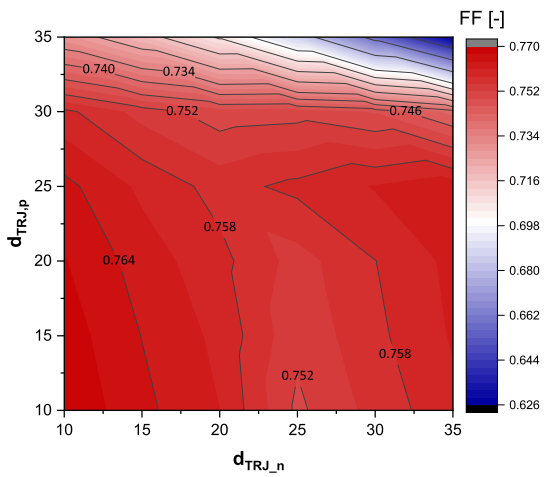

Figure 4.23: Fill factor variation for various TRJ layer thickness combinations.

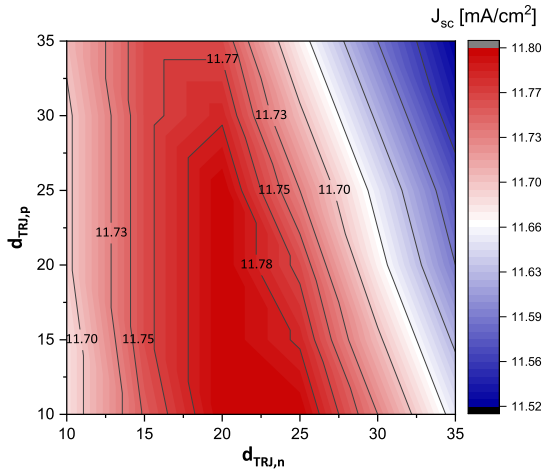

Figure 4.24: Short circuit current density variation for various TRJ layer thickness combinations.

To reach the best parameters for the TRJ layers, we shall consider another variable of doping. The contribution and significance of this are discussed in the next section 4.11.2.

4.11.2. TRJ activation energy Combinations

To maximise the device performance the activation energy, E_a of each doped layer is studied. The simulations for this study has a constant thickness for n-p TRJ layers at 25 nm and 20 nm respectively. JV curves shown in the figure 4.25 demonstrates the JV behaviour of different doping concentrations of the TRJ layers (Please note that the figure does not include all the JV curves considered). The activation energy (E_a) of n layer is the energy difference between the electron Fermi level and the conduction band and E_a of p layer is the energy state difference between hole Fermi level and valance band.

In the figure 4.25 E_a values 0.25 and 0.20 makes the best curve followed by E_a (0.20,0.20) and E_a (0.20,0.15) combinations. The n-doped layer E_a when exceeding 0.25 shows a fall in the value of FF. Similarly, if the E_a of p-doped layer hikes above 0.20 showcases the same behaviour. The JV curve of the tandem cell with TRJ is also plotted at an extreme case combination of E_a 0.10 and 0.40 which deviates drastically from the ideal curve. From these observations, we can derive that a donor activation energy of 0.20eV - 0.25eV and an acceptor activation energy of 0.15-0.20 is ideal for our tandem recombination junction at specified thicknesses. The doping activation energy values we have arrived at is reasonable, as it shows that highly doped p layers (lower activation value) facilitate better carrier transport for holes (entities with larger effective mass value) towards TRJ. The complete simulation results of this study are included as an Appendix D in this report. The topic

needs further analysis of behaviour and is elaborately discussed in the upcoming section 4.14.

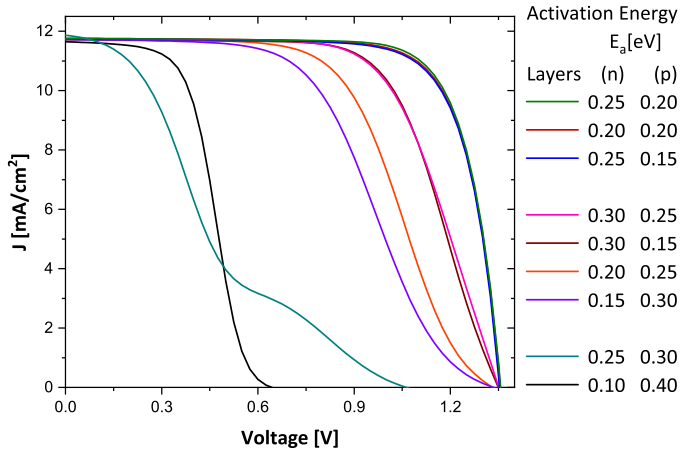

Figure 4.25: ASA simulated JV curves for different doping profiles of TRJ layers.
NB: Order of legend in descending order of FF values.

4.12. Performance at 2µ thick bottom layer

Now as we have gained the best performing parameters through studies, variations in short circuit current for a 2µ thick bottom cell at HyET can be focused. A variation of top cell thickness against a constant bottom cell absorber is conducted to identify the value of current limiting top cell thicknesses. The short circuit current variation with different top cell thicknesses combined with 2µm bottom cell absorber is represented in the diagram 4.26. The blue shaded region is top cell current limiting while the red background thicknesses mark the bottom cell current limits. Thus a maximum value of 11.75 is reached at a top cell thickness of 156 nm.

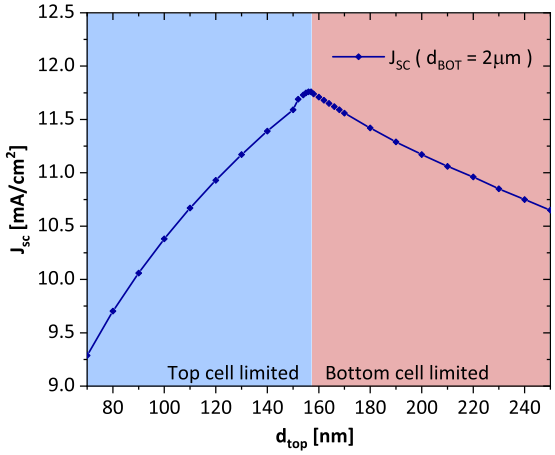

Figure 4.26: J_{sc} values at different top cell thickness for a fixed bottom absorber of 2µ

4.13. Optimized device performance

Since the studies on thicknesses of absorber layers and TRJ is complete, the structure parameters depicted in the section 4.8 can be modified. With the current matched absorber thickness combination in topic 4.10 and performance maximised TRJ parameters under section 4.11 the cell is expected to deliver the best performance. The parameters from optimisation, used for these simulations are tabulated below :

Table 4.2: Optimised parameters for the simulated micromorph tandem structure.

Layer	a-Si:H Absorber	n – $ncSiO_x$ TRJ		p – $ncSiO_x$ TRJ		ncSi:H Absorber
Parameter	Thickness [nm]	Thickness [nm]	Activation Energy [eV]	Thickness [nm]	Activation Energy [eV]	Thickness [nm]
Value	156	25	0.20-0.25	20	0.15-0.20	2000

ASA generated JV curve and spectral response for micromorph configuration with the above parameters (selected E_a n layer = 0.25 and E_a p layer=0.20) is given in images 4.27 and 4.28 respectively.

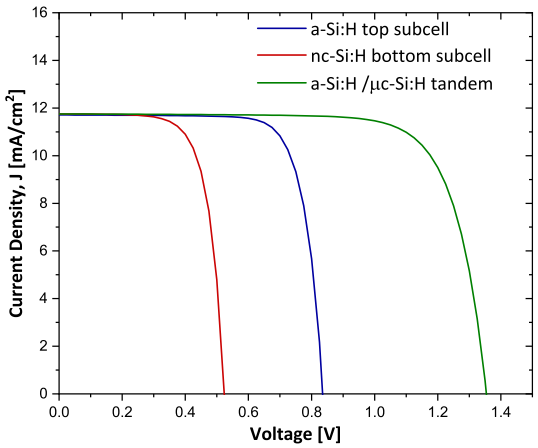

Figure 4.27: Illuminated JV : optimised micromorph model.

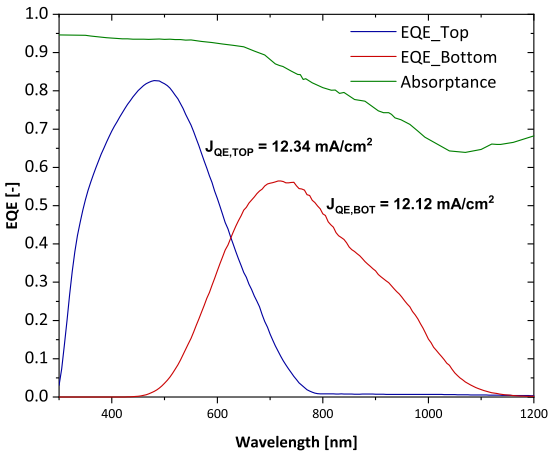

Figure 4.28: Spectral response : optimised micromorph model.

Table 4.3: Current matched condition, external parameters from ASA

	Thickness [nm]	J_{sc} [mA/cm^2]	V_{oc} [V]	FF [-]	η[-]
a-Si:H sub cell	156	11.76	0.835	0.77	-
µc-Si:H sub cell	2000	11.78	0.523	0.72	-
aSi:H/µc-Si:H Tandem	-	11.76	1.356	0.76	12.2

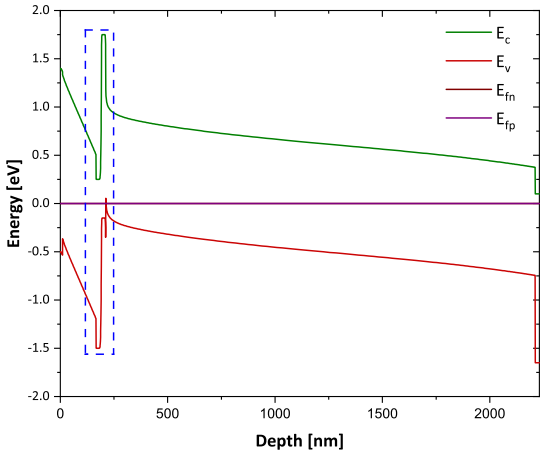

Figure 4.29: Optimised model band diagram at equilibrium.

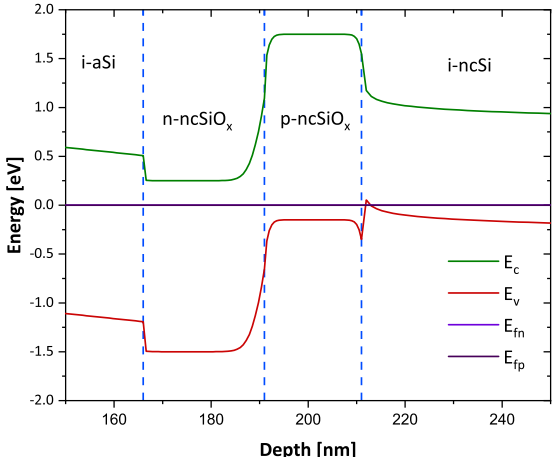

Figure 4.30: Zoomed in band diagram at equilibrium.

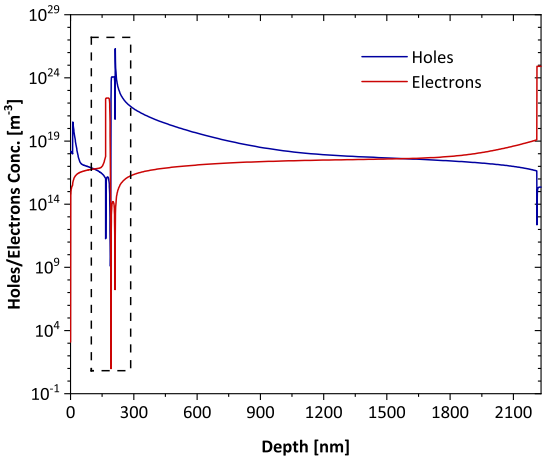

Figure 4.31: Electron and hole concentrations of the optimised model at equilibrium.

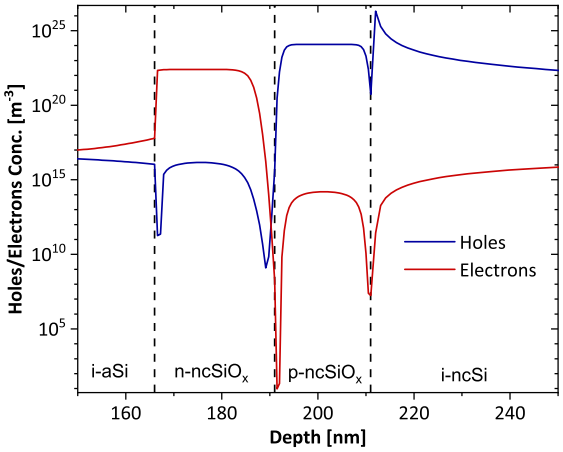

Figure 4.32: Zoomed in electron and hole concentrations at equilibrium.

From the electron and hole concentration graph focusing at 191 nm - the TRJ line, notice a fall in the concentration of electrons and holes on respective sides indicating an efficient sweeping of electrons to the sides and the recombination at the junction.

4.14. Tunnelling Recombination Junction doping

The significance of doping for the recombination junction is already evident from the study in the section 4.11.2. This end of the thesis discusses the idea in detail. This is conducted in two cases. *Case 1:* n-layer activation energy is kept constant and p-layer activation energy varied. *Case 2:* p-layer activation energy is kept constant and n-layer activation energy varied. For each cases recombination and band bending are observed at :

1. equilibrium : to understand how different is the behaviour of bands and electric field at equilibrium conditions.

2. maximum power point (MPP) of each curve : to see how the Fermi levels and recombinations vary at their own power points of each system.

3. optimised MPP bias voltage of 1.053V : to have an insight on why the other systems cannot generate the same current as of the optimised cell at this voltage.

NB: For the upcoming sections, green, red and blue are used as a colour convention for better apprehension. Green is the optimised performing cell, the blue curve is the worst performing and red is a slightly deviating "moderately" performing cell.

4.15. Case 1 : n layer E_a = 0.25eV

In this analysis , we keep the n doping constant and the E_a of p-doped layer is changed as 0.25eV and 0.30eV and compared with an ideal optimised value of 0.15eV. The simulated JV curves are represented in 4.33, and the curves show a decrease in performance on deviating from the optimised case. An increase in E_a value by 0.5eV shows a slight decrease in FF value but with similar J_{sc} and V_{oc} as ideal case. When the activation energy gap is doubled the resultant cell performance represents and drastic drop in FF and noticeably V_{oc}.

The corresponding band diagrams solved at equilibrium is depicted in the image 4.34. The influence of doping on band diagrams can be observed at the TRJ position of 191 nm on the depth axis. The energy gap between the conduction band of the n layer and the valance band of the p layer can be observed to increase with an increase in activation energy of the p layer. Thus, with a p-layer of insufficient doping, the valance band is more distant from the conduction band (the curved point in the graph). This trend is in exact congruence with performance decline. We can infer that a drop in FF is a direct implication of gap between the two TRJ band energies.

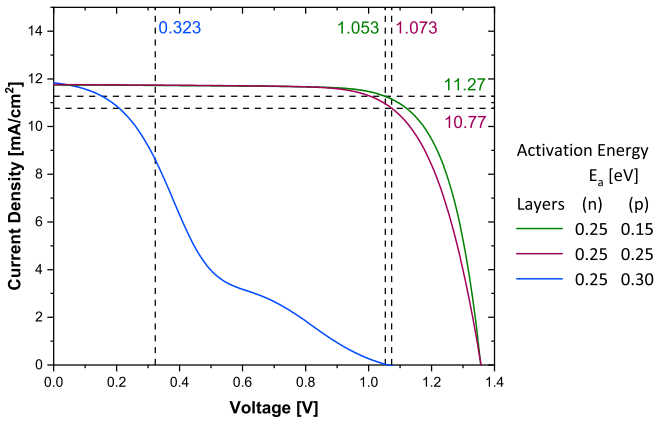

Figure 4.33: JV curves for case 1 analysis - n layer E_a = 0.25eV

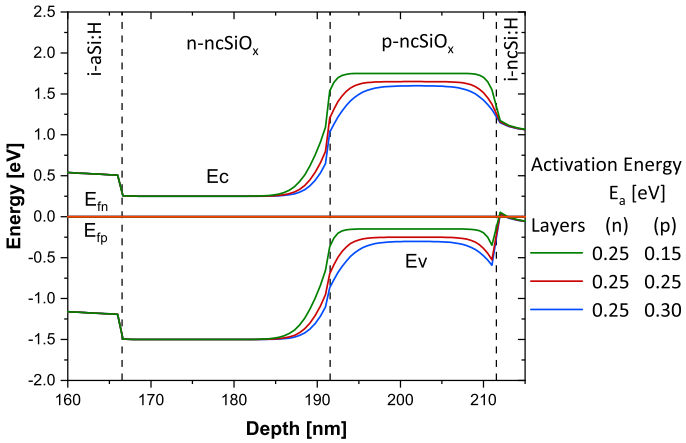

Figure 4.34: Band diagrams solved at equilibrium : case 1 analysis n layer E_a = 0.25eV

4.15.1. Comparison at bias voltage = 1.053

The cell generates maximum power at bias voltage 1.053V. The current density of the optimised cell at this bias value is 11.27(mA/cm^2). The other considered models generate 10.98 (mA/cm^2) and 0.1 (mA/cm^2) at this bias. The plots depicted 4.35 and 4.36 help in the study of electron-hole behaviour inside the cells at bias voltage = 1.053V. From the Fermi-level plot, we discern that the activation energy of 0.25eV for n layer combined with a p layer activation of 0.15eV results in an equal Fermi-energy state for electrons and holes on either side of the junction. This is a criterion for a TRJ to give peak performance[37]. For this same bias voltage, with a decrease in p layer doping, the energy difference between the E_{fn} and E_{fp} increases thereby suggesting the accumulation of charged entities in the TRJ layers, suggesting poor recombination.

The recombination data in the figure 4.36 shows lower recombination in the p layer with lower doping levels(blue curve). Also, it can be noted that in the best performing model(green curve), at the vicinity of the TRJ line (at 191 nm) has a sudden drop in recombination, which is also an indication that most of the carriers are tunnelled through and recombined at the junction. Focusing on the extreme case shown in the diagram, i.e, p doping E_a = 0.30, the blue curve suggests higher recombinations in the absorber layers, which shall be due to an insufficient electric field in the bottom cell. Also, a closer look at the graph indicate little or no drop of value at the interface for this case, which means fewer carriers tunnelled which explains a near-zero

current at a bias voltage of 1.053.

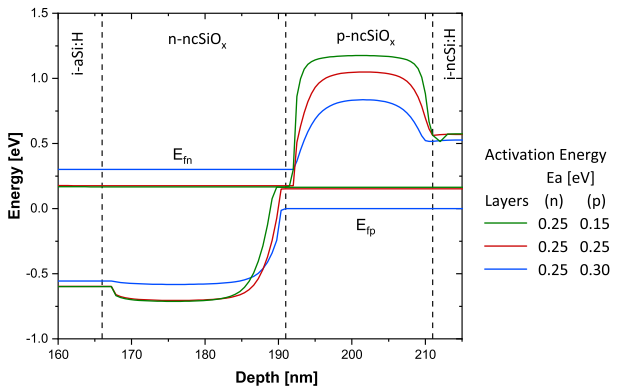

Figure 4.35: Comparison of Fermi levels at different p-layer activation energies at bias voltage = 1.053

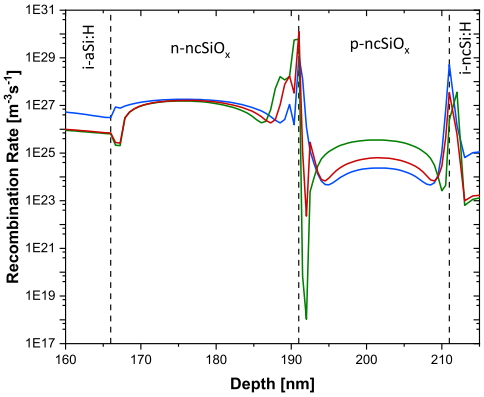

Figure 4.36: Comparison of recombination rates at different p-layer activation energies at bias voltage = 1.053

4.15.2. Comparison at MPP

The Fermi-level analysis and recombination rate analysis at the maximum power point of each system is discussed in this subsection. The combination of E_a (0.25,0.15) is analysed at bias voltage 1.053 V, then E_a (0.25, 0.25) combination at 1.079V and very low FF resulting JV curve due to E_a(0.25,0.30) combination is considered at 0.323 V.

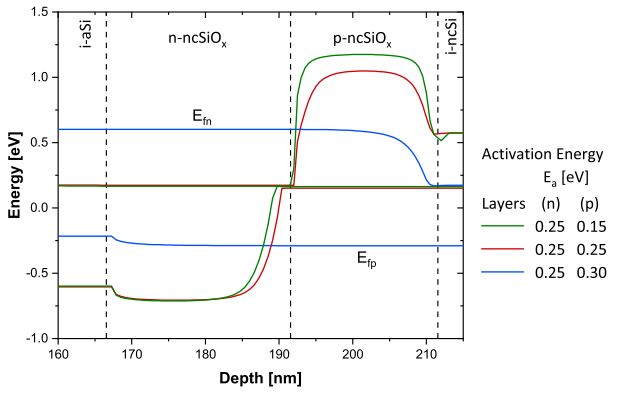

Figure 4.37: Comparison of Fermi levels at different p-layer activation energies at their own MPPs.

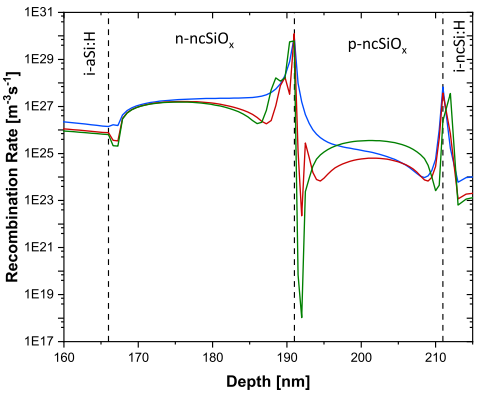

Figure 4.38: Comparison of recombination rates at different p-layer activation energies at their own MPPs.

For the very poor performing MPP point, the electric field at TRJ is not enough thereby forming a thick tunnelling barrier that is not easily penetrated by the electrons and holes. The Fermi level approximately remains constant indicating very high accumulation of charge carriers. Thus the number of carriers available for recombination is not high at low bias voltages for this configuration and shows a low performance in totality. A loss-free addition of the V_{oc}-s in a tandem cell is only accomplished when the quasi-Fermi levels of electrons and holes in the TRJs have the approximately same value. In summary, the blue curve shows an extreme deviation from the optimised case (green curve) in both Fermi-level explaining a low V_{oc} observed in the JV graph. The recombination plot shows no drop near the junction which indicates to recombination via extended valance and conduction band states as the mechanism there rather than tunnelling. Refer to section 2.8.

4.16. Case 2 : p layer E_a =0.15eV

For this analysis, we keep the p doping constant and the E_a of n-doped layer is varied as 0.30eV(red) and 0.40eV(blue) and compared with an ideal optimised value of 0.25eV (green). The JV curves for these models are shown below in this topic. At n layer with E_a = 0.30eV the fill factor decreases and has the maximum power point at a low voltage and low current density compared to the best case. The performance parameters drop drastically on a further decrease of doping. It can also be seen that the blue curve makes an open circuit voltage of approximately 0.7V.

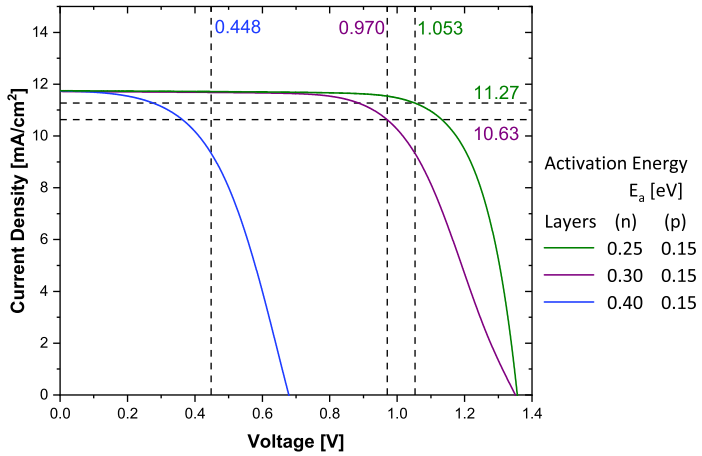

Figure 4.39: JV curves for case 2 analysis - p layer E_a =0.15eV

The band diagram of corresponding configurations (figure 4.40) clearly shows an increase in energy difference between the lowest point on conduction band in n – $ncSiO_x$ and the highest point in the valance band of p – $ncSiO_x$. Thus the closer these band energies are, the better the tunnelling and thus better is the performance. This conclusion is the same as what we reached in case 1 equilibrium state. Thus the p layer or n layer activation energies hold equal priorities in a TRJ.

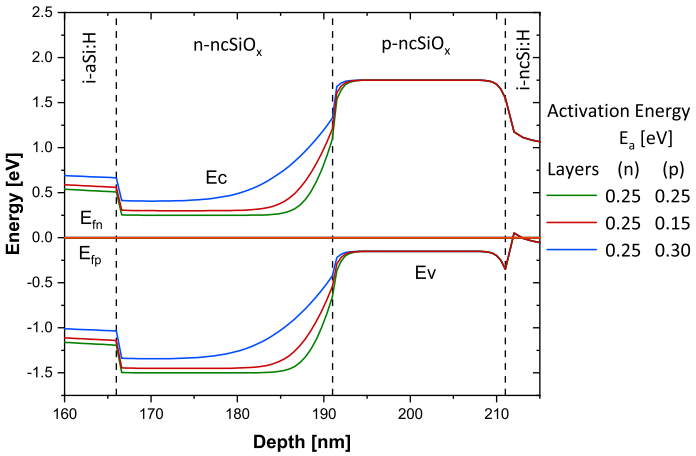

Figure 4.40: Band diagrams solved at equilibrium : case 2 analysis - p layer E_a =0.15eV

4.16.1. Comparison at bias voltage = 1.053

Similar to the comparison in case :1, here we have a detailed evaluation for case 2, keeping the activation energy of the p layer at a constant value. The Fermi level shows a very similar trend as in the previous case. The best curve of optimised combination has coinciding energy state Fermi levels (Green) leading to good performance, indicating good recombinations. in contrast, the worst-performing cell shows significant recombination at a point that is very far from the desired vicinity of the TRJ junction (depth = 191 nm). This also suggests why this JV curve point lies in the fourth quadrant. The junction layers don't serve their desired purpose in this configuration similar to an 'unrealistically' large voltage drop across TRJ noted by J.A.Willemen [37].

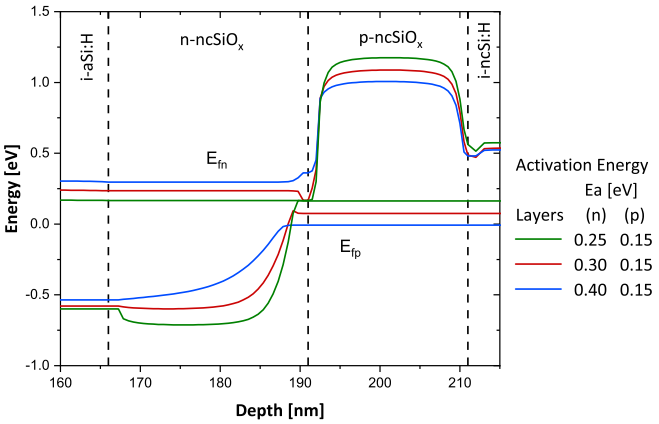

Figure 4.41: Comparison of Fermi levels at different n-layer activation energies at bias voltage = 1.053

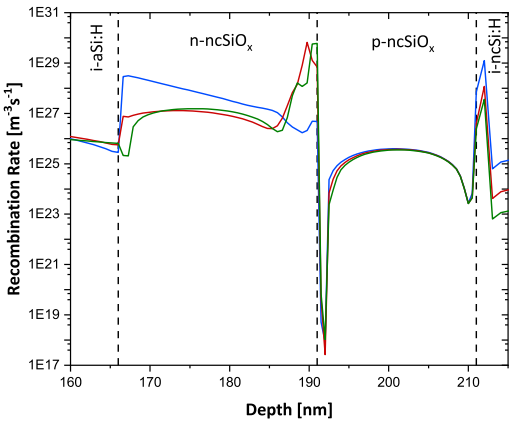

Figure 4.42: Comparison of recombination rates at different n-layer activation energies at bias voltage = 1.053

4.16.2. Comparison at MPP

The maximum power point of the best cell (green curve), the next good cell (red curve) and the worst-performing cell (denoted by the blue curves) follow a trend of Fermi levels. The explanation of this behaviour is very similar to the case 1 study but shall be explaining the p side of TRJ similar to the n side in case 1. the Fermi level splitting profiles into the layers is very same as observed in case 1.

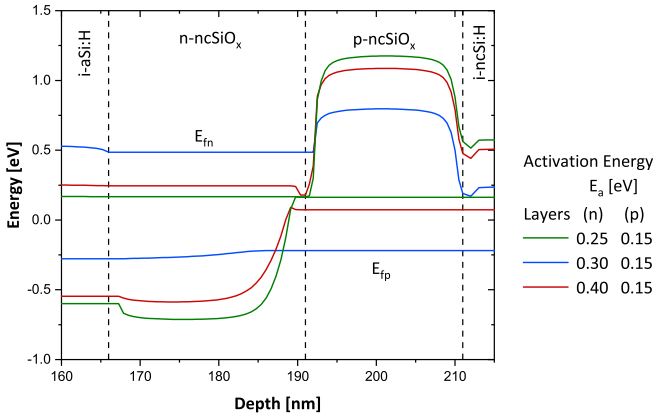

Figure 4.43: Comparison of recombination rates at different n-layer activation energies at their own MPPs

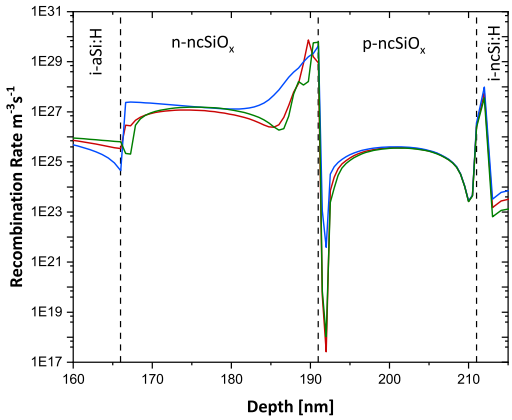

Figure 4.44: Comparison of fermi levels at different n-layer activation energies at their own MPPs

This concludes that with poorly doped layers, the objective of TRJ to facilitate tunnelling recombination at the junction is not satisfied and ultimately affect the cell behaviour forming a reverse biased n-p junction . One thing we should reckon regarding the conclusions from this section is that we did not consider any optical variations while explaining the graphs. We should not lose sight of the fact that fabricated solar cells often show much large number of defects with p-doped layers compared to n-doped layers and also higher resistance properties.

4.17. Oxygen fraction in p-$\mu cSi:O_x$

The conditions at which each layer is fabricated is very basic for its optical and electrical properties. In the fabrication using AMIGO cluster tool, we use CO_2, along with SiH_4 and B_2H_6 flows for $p-ncSiO_x$ deposition. The value of CO_2 flow determines the oxygen fraction in $p-ncSiO_x$ layers. These different physical conditions used for fabrication and characterisations are tabulated in table 4.4. All these depositions are done at pressure = 2.2, Power = 12 and chamber temperature = 300K.

In the table ,the deposition names are suffixed with their corresponding standard cubic centimeters per minute (SCCM) flow rates. From now on, in this study, these shall be used as the name to refer to the corresponding layers. Also here it shall be specifically noticed that the properties of the $p-ncSiO_x$ layer used in optimised model simulations, lies between sccm 1.6 and 2.4 and is assumed to be 2.0 here. Both electrical and optical properties of the materials with varying the oxygen fraction "X" are recorded in the table 4.4.

The idea of these simulations is to improve the optical response and performance of solar cells by varying the oxygen content of the $nc-SiO_x$ layers. For the simulations, we have accounted the change in the bandgap, the corresponding change in refractive index and extinction coefficient values of the materials. From the characterisation, the bandgap values obtained for CO_2 precursor gas flow of 0.8 sccm and 1.6 sccm, it can be observed that the bandgap of these deposited layers is less than the calibrated bandgap of a-Si (E_g = 1.70). These measurements were done with ellipsometry.

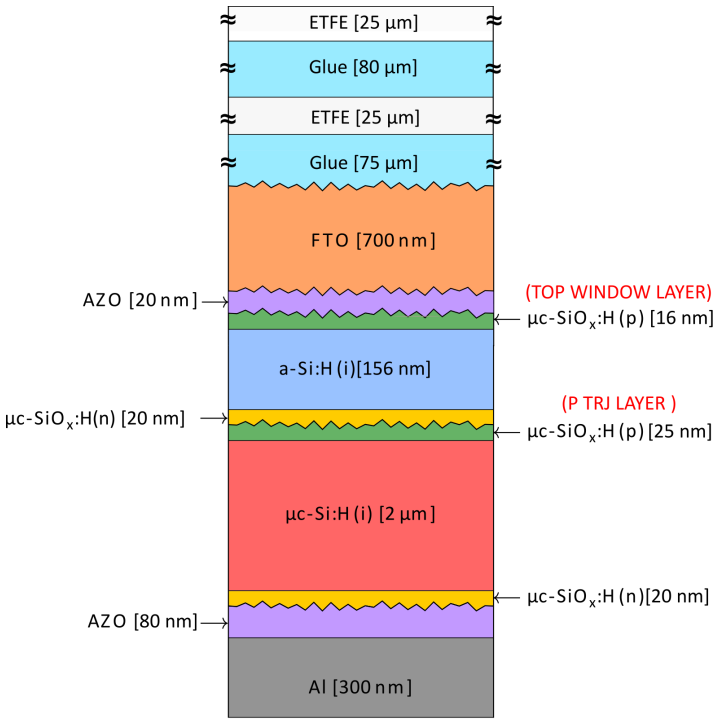

Figure 4.45: The micromorph tandem solar cell layers structure changed to 3.2 sccm simulated on ASA. With encapsulation. NB: The thicknesses are not to scale

For this study, we vary the optical parameters in the input n-k data file and the electrical side in the form of a bandgap. For the simulation purposes, the considered layers are assumed to maintain the same activation

energy as the optimised values in the section 4.11 and no change for E_a is made in the .cas file.

Table 4.4: The deposition condition for p – ncSiO$_x$ in amigo cluster tool. Depositions are done at pressure = 2.2, Temperature = 300K, power = 12

Layer	SiH_4 [sccm]	B_2H_6 [sccm]	H_2 [sccm]	CO_2 [sccm]	Thickness [nm]	Deposition Rate [nm/s]	n@600	E04	EG [eV]
p – ncSiO$_x$0.8	0.8	20	170	0.8	48.67	0.044	4.08	1.89	1.362
p – ncSiO$_x$1.6	0.8	20	170	1.6	27.04	0.025	2.98	2.00	1.532
p – ncSiO$_x$2.0	0.8	20	170	2.0	-	0.032	2.56	-	1.900
p – ncSiO$_x$2.4	0.8	20	170	2.4	35.14	0.032	2.25	2.58	2.186
p – ncSiO$_x$3.2	0.8	20	170	3.2	41.49	0.038	2.04	2.68	2.228

4.17.1. p-doped ncSiO$_x$ layer as top window layer

The p-doped layer of the top subcell is substituted in the ASA simulation and top cell thickness is varied over a range to identify the current matching thickness of the top absorber corresponding to the fixed bottom thickness of 2 microns. The bandgap values obtained for p – ncSiO$_x$ CO_2 flows of 0.8 and 1.6 sccm, it can be seen that the bandgap of the deposited layer is less than the calibrated bandgap of a-Si (E_g = 1.95) used in our model. Thus the layer cases are omitted from simulations. The results are depicted in the figure 4.47. Though the variation in oxygen content in the p – ncSiO$_x$ layer results in possible transparent (wider bandgap) materials but also cause a change in refractive indexes which results in more reflection. As seen from the graph, p – ncSiO$_x$ 2.0 is the best among the three as it results in an equal maximum J_{sc} value as that of p – ncSiO$_x$ 2.4 but with thinner top absorber. Thin top cells are advantageous since they always result in better-stabilized efficiencies. This study concludes that the p layer used in the calibrated cell is the best among the considered five cases.

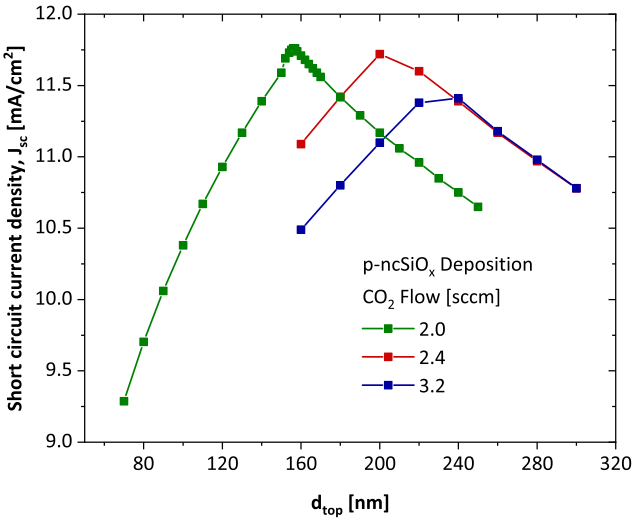

Figure 4.46: Comparison of current matching thickness for different p – ncSiO$_x$ layers used as window layer

4.17.2. p-doped ncSiO$_x$ layer in TRJ

As the next step, the p-doped layer in TRJ is substituted in the cas file. The top cell thickness for current matching corresponding to a fixed bottom thickness of 2 microns in each case is calculated. Here we consider the possibility of using p – ncSiO$_x$ as an intermediate reflection layer similar to the study done by P.Babal[41].

We substitute the p layer of TRJ by experimentally measured data with different CO_2 flows (sccm = 0.8, 1.6, 2.0, 2.4, 3.2). Similar to the previous study, we omit the possibility of using p – ncSiO$_x$0.8 and p – ncSiO$_x$ 1.6 as TRJ since we aim at reflection back to top cell and minimizing the absorption. From the results in the figure 4.48 we deduce that, with increasing oxygen content in the layer, we can achieve a current matched

state with thinner top cells. For p – ncSiO$_x$ 2.0 the needed thickness is 156nm, for ncSiO$_x$ 2.4 it decreases to 150nm and for ncSiO$_x$ 3.2 the current matched top cell is 145nm thick.

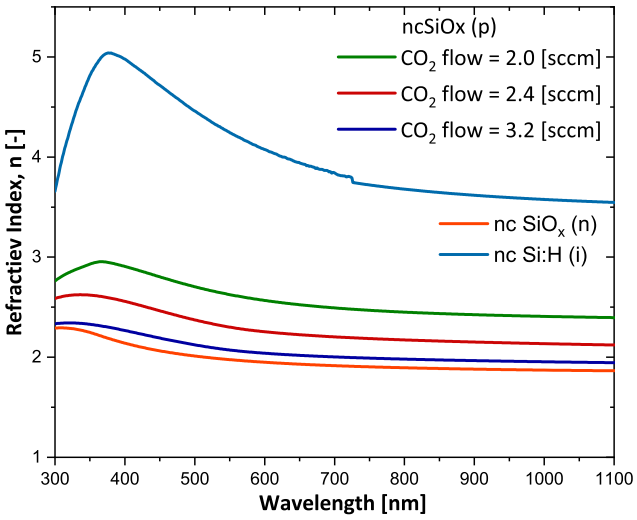

Figure 4.47: nk data associated with the new p layer TRJs

Paying attention to the top cell limited region we can observe that the plot shows a current increase for all top cell thickness ranges for ncSiO$_x$ 3.2. At the same time for the bottom limited region, the values are lower for each thickness. From these observations, it can be concluded that this trend is due to the reflective behaviour of the new p layer. For ncSiO$_x$ 3.2 the micromorph cell is bottom cell limited from 146nm thickness of aSi:H cell. Though the J$_{sc}$ value decreases with increasing sccm in fabrication, yet it opens a possibility of extraction of higher J$_{sc}$ for the total micromorph configuration. To extract the benefit of this behaviour of nc – SiO$_x$ 3.2 TRJ layers, the bottom cell needs to be thicker or require a reflection layer at the bottom to increase absorption in µcSi:H cell. These prospects are discussed in the next section 4.17.3.

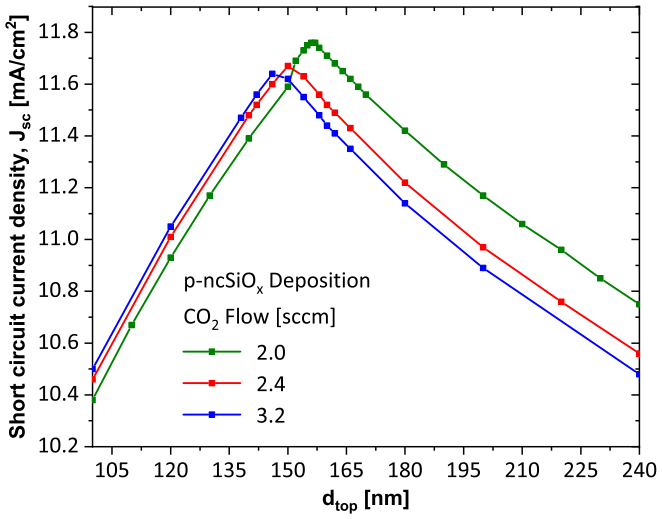

Figure 4.48: Comparison of current matching thickness for different p – ncSiO$_x$ layers used as TRJ layer

Note: The n layer oxygen fraction is not considered in this study due to deposition issues. The measurements of n value at 600nm and energy gap measured were not consistent and could not be proceeded due to time constraints. A similar study on the n and p layers combined can give better insights into this idea.

4.17.3. Possible extraction of higher current density using back reflector

The above discussion on current matching at different TRJ layers shows that the peak J_{sc} value can be achieved at a thinner top cell absorber thickness. This means that all combinations of top subcell thickness are more than that value, the tandem is limited by bottom subcell J_{sc}. As a study to demonstrate this, 100 nm thick silver is used as the back reflector and simulations are run on ASA.

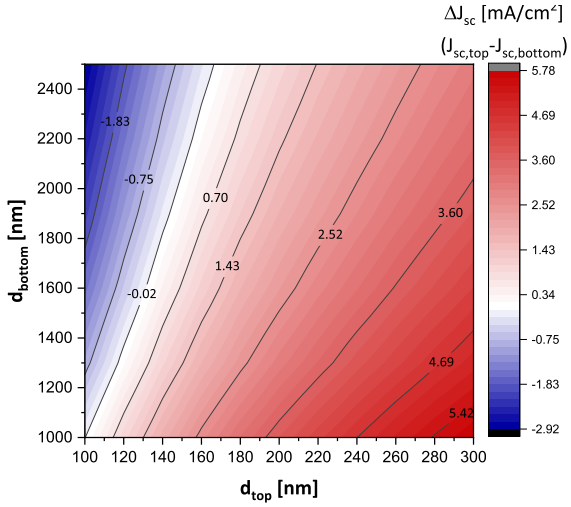

Figure 4.49: Current matching condition of micromorph cell with ncSiO$_x$ 3.2 combined with silver back reflector.

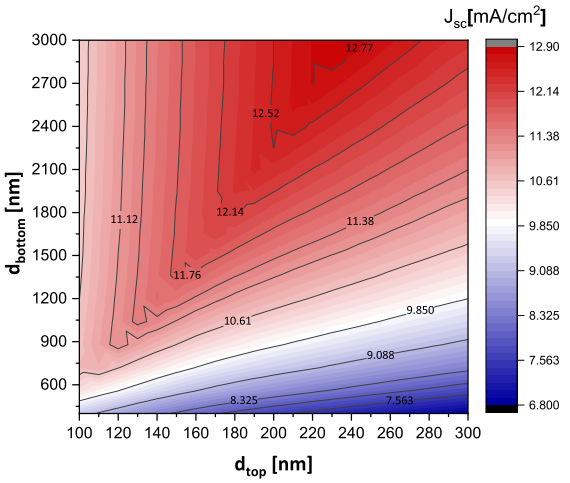

Figure 4.50: J_{sc} of micromorph cell with ncSiO$_x$ 3.2 combined with silver back reflector

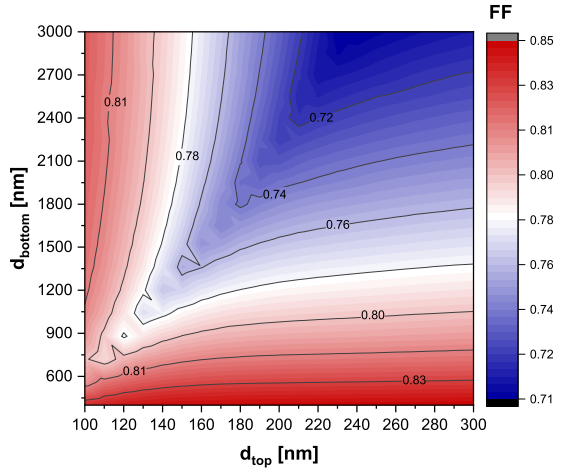

Figure 4.51: FF of micromorph cell with ncSiO$_x$ 3.2 combined with silver back reflector

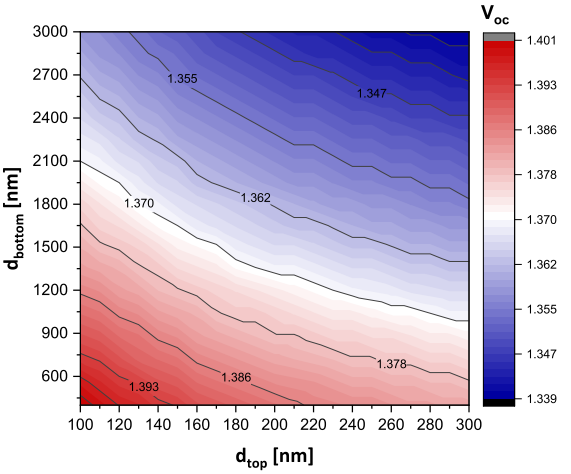

Figure 4.52: V_{oc} of micromorph cell with ncSiO$_x$ 3.2 combined with silver back reflector

A comparison can be done with the optimised performance discussed in the previous section 4.2. The current match line for our new structure (figure 4.49) has shifted towards the thinner top cell thickness side (towards left). In J_{sc} value, the previous best J_{sc} value of 11.74 is now obtained at a top cell 146 nm - bottom cell 1300 nm absorber combinations. This indicates that the reflection from TRJ combined with the reflection layer at the bottom can be beneficial in tackling the Staebler Wronski effect in our cells. These thin cells can also contribute to a slight increase in V_{oc} as thinner subcells have less recombination probability consequently increasing the V_{oc}.

Shifting our interest to bottom cell thickness of 2000 nm, the maximum possible J_{sc} shows a hike by 0.5

mA/cm^2. at 180 nm thick top cell resulting in a new total efficiency value of 12.42%. The feasibility for use of expensive material like silver in solar cells is a trade-off between the increased cost of production and the benefit it gives in terms of material and efficiency.

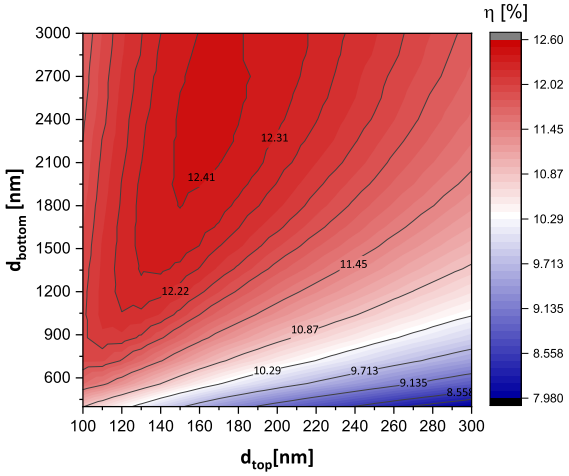

Figure 4.53: Efficiency of micromorph cell with ncSiO$_x$ 3.2 combined with silver back reflector

4.18. Deviation from STC : temperature and irradiation

Tandem module performances are very sensitive to current matching conditions. So for these modules, it is necessary to have an examination of the micromorph module's temperature-dependent and spectral mismatch characteristics. In this part of the thesis, we address the change in performance parameters of the micromorph configuration with temperature and irradiance spectrum.

4.18.1. Temperature-dependent characteristics of the tandem cells

The temperature dependency of performance was modelled by including multiple relations to ASA. Namely altering the density of states, the carrier mobilities and exponential tail state values. In addition to these, the mobility gap was assumed as independent of temperature along with the optical bandgap. The activation energy of the material shall also vary with respect to temperature but we neglect this for convenience. The above-mentioned parameters that are varied inversely proportional to temperature fraction (T/T$_{stc}$) to the power 1.5 [68].

ASA faces limitations in simulating J$_{sc}$ value changes because the optical solver does not incorporate temperature changes. Experiments and literature state that the J$_{sc}$ has a positive temperature coefficient. To perfectly replicate this optical band gap approach need to be used together with n-k data change and corresponding band gaps on ASA separately. Since the FF is dependent on current matching as we have already seen in the section 4.10 , we shall expect these errors to be carried over to FF and efficiency also. In such a case, the simulated parameters are V$_{oc}$ and Efficiency only. For these simulations, the mentioned temperature is the semiconductor temperature, and it is considered uniform in the module.

The temperature vs V$_{oc}$ and Temperature vs Efficiency plots shows a trend in slope. The drop of V$_{oc}$ and Efficiency drop grows when the semiconductor is hotter. Thus the coefficient of V$_{oc}$ and efficiency reduction is bigger towards higher temperature region. Neglecting this effect a linear fit is done for a rough estimation of declining performance. This is summarised in the table 4.5. The top cell V$_{oc}$ change in this study is in good agreement with the experimental results from modules of HyET as reported by A.Anchalia [69].

NB: In the table 4.5, the top and bottom subcells efficiencies are noted as NA, because these are heavily dependent on spectral distributions. The V$_{oc}$ change per temperature gives good agreement : the decrease in the top and bottom subcells sums up to the decline in tandem.

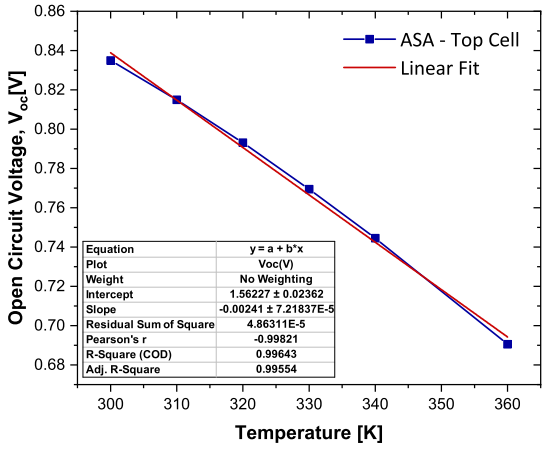

Figure 4.54: Top cell V_{oc} w.r.t change in module temperature

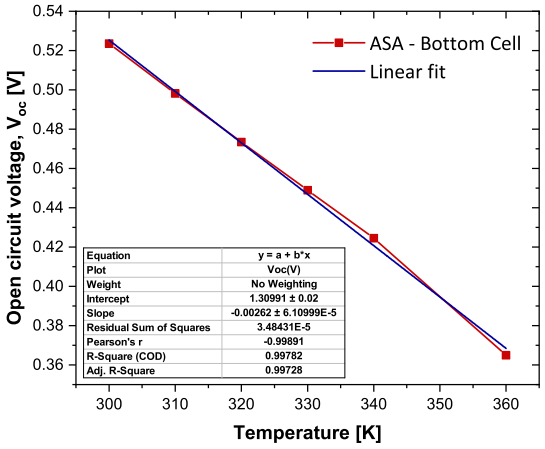

Figure 4.55: Bottom cell V_{oc} w.r.t change in module temperature

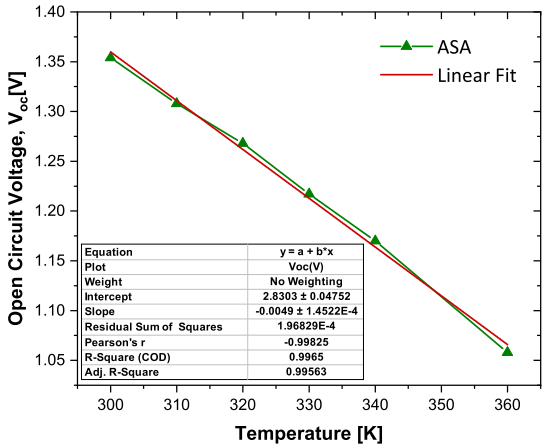

Figure 4.56: Micromorph V_{oc} w.r.t change in module temperature

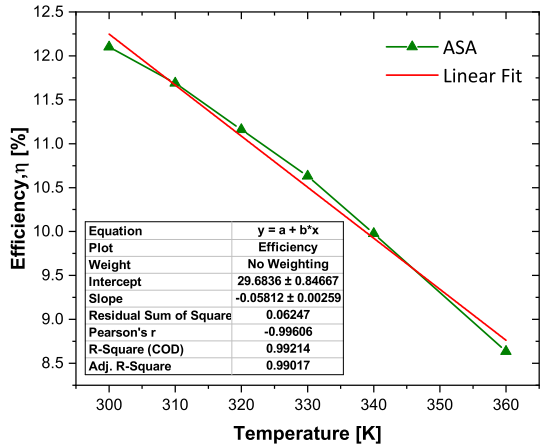

Figure 4.57: Micromorph efficiency variation w.r.t change in temperature

Table 4.5: Temperature coefficient of subcells and tandem configuration (Linear fit).

	V_{oc} decrease [V / K]	EFF decrease [% / K]
Micromorph tandem	0.0049	0.058
Top subcell	0.0024	NA
Bottom subcell	0.0026	NA

4.18.2. Impact of spectral mismatch on the tandem performance

For observing the irradiation changes and predicting the real-world performance of the tandems we consider AM1.5 spectrum fractions. To mimic wavelength imbalances affecting the tandem we consider two wavelength ranges : (1) 300nm - 750nm and (2) 750nm - 1200nm. A powerful method to investigate the current matching of the cell is to simulate this [70]. For spectral variations, ASA needs alteration in the input spectrum file as fractional changes to the flux. We have considered 750nm as a point of attention because the a-Si cell is responsive till this point and the bottom cell response till this point shall be seen as complementary. Once we shift the analysis to wavelength-dependent flux change, the idea is to replicate an environment with coloured light and investigate the current mismatch in tandems for those cases. J_{sc} values are recorded

against consecutively varying spectral flux.

350nm - 1200nm : On varying the AM1.5 flux in ASA, 1000W/m^2 is reduced down to 0.6 times the flux and later increased to 1.4 times the irradiation. The JV curve shows a scaled increase in its shape image 4.58. The performance of tandems increases linearly with the availability of more photons. No mismatch is observed in the subcell currents as there is no slope change in the J_{sc} vs AM1.5 fraction plot. The slope of this graph is a combined effect of both subcells.

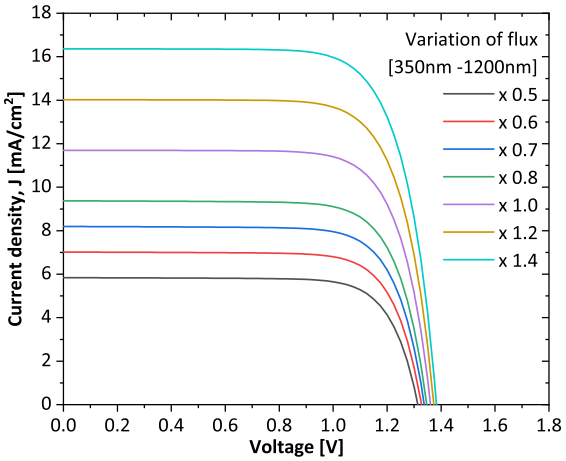

Figure 4.58: Micromorph illuminated JV variation with consecutively varied AM1.5 spectrum from 0.6 times to 1.4 times the total flux

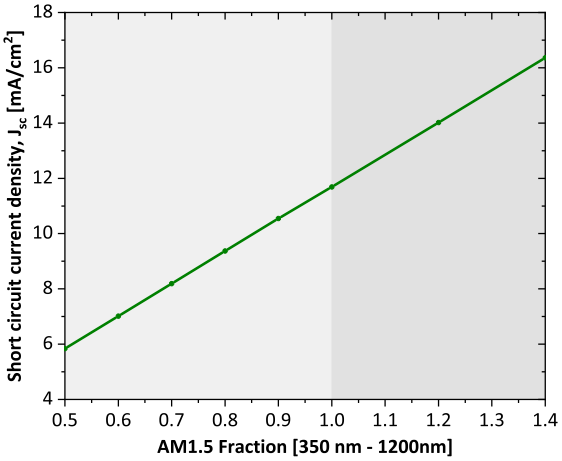

Figure 4.59: Micromorph J_{sc} variation versus consecutively varied AM1.5 spectrum from 0.6 times to 1.4 times the total flux

750nm - 1200nm : The photon flux for 350nm - 750nm is maintained the same as AM1.5 spectral flux. The slope remains constant till J_{sc} value reaches 11.7 mA/cm2 and slowly saturates beyond that. The successive JV curves also get closer indicating the same. The region beyond 1.0 X Flux is top cell limited. This is because the a-Si:H top cell is not responsive for flux alterations beyond 750 nm wavelength.

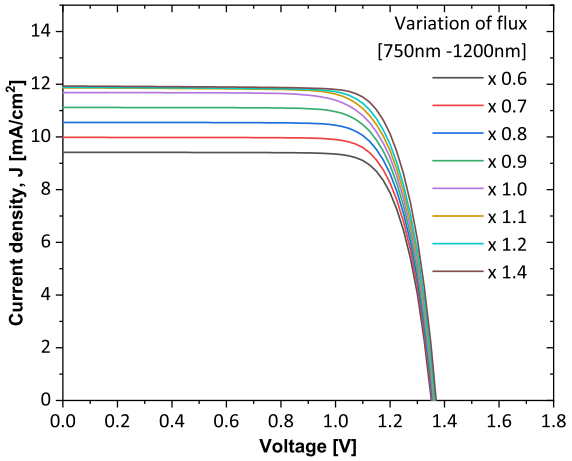

Figure 4.60: Micromorph illuminated JV variation with consecutively varied 750nm -1200nm from 0.6 times to 1.4 times the total flux

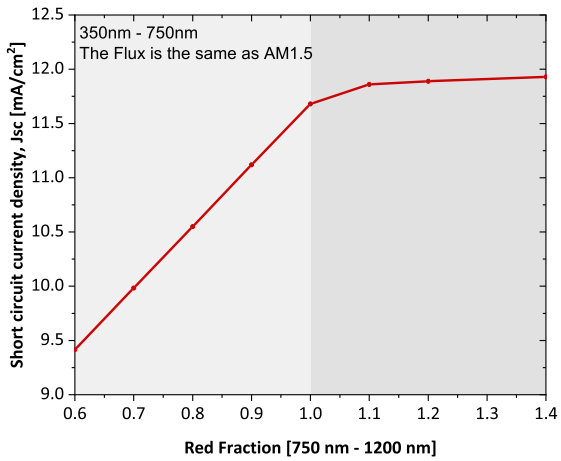

Figure 4.61: Micromorph J_{sc} variation versus consecutively varied 750nm -1200nm from 0.6 times to 1.4 times the total flux

350nm - 750nm variation : The photon flux for 750nm - 1200nm is maintained the same as AM1.5 spectral flux. The wavelengths below 750nm are contributing to the top cell current value and this acts as a limiting condition for the tandems here. As a result, J_{sc} increases up to the matched value of 11.7 mA/cm2 at 1.0 times the flux and shows a decrease in slope. This region is bottom cell current limited, but unlike the red spectrum

change case, the J_{sc} does not saturate to a constant value as the ncSi:H bottom cell is also responsive to a wavelength between 550 to 750 nm.

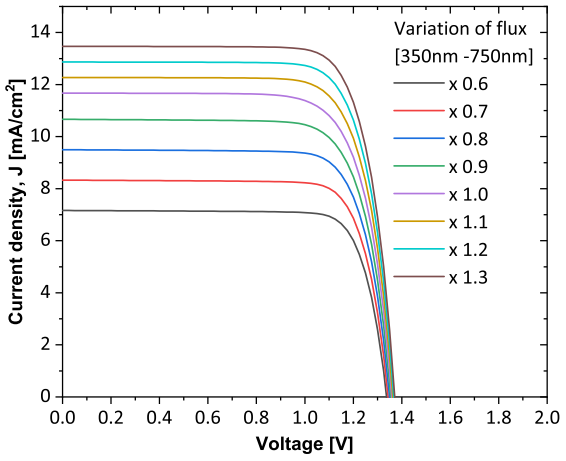

Figure 4.62: Micromorph illuminated JV variation with consecutively varied 300nm -750nm from 0.6 times to 1.3 times the total flux

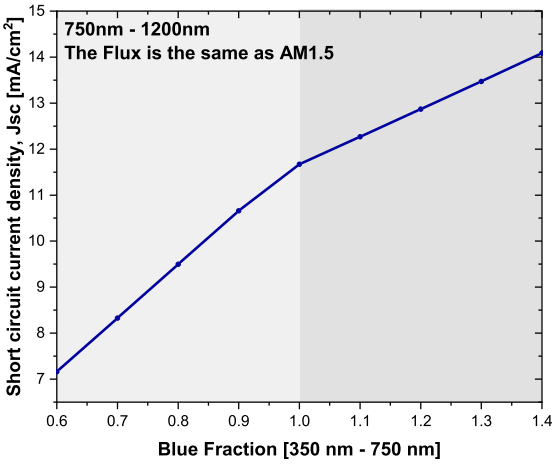

Figure 4.63: Micromorph J_{sc} variation versus consecutively varied 300nm -750nm from 0.6 times to 1.3 times the total flux

4.19. Light soaking condition

This part of the thesis is a preliminary trial to incorporate light soaking effects into our model to predict the performance under extended illumination conditions. This is an essential study in performance analysis. Different models have been developed to explain the Staebler Wronski effect (refer section 3.2.2) over the years [71] but the exact physical background and modelling of the phenomenon are still not thoroughly explained. Irrespective of the models, it is assumed that the degradation is caused by defect creation and defect creation is caused by the recombination events. In this portion of the thesis, we consider an approach followed by A.Klaver et.al. [72] by using the defect density of states variation modelled on ASA.

4.19.1. Modelling

For replicating light soaking we use the real measured degradation data of HyET solar which we try to explain using the existing models. The observed trends in parameter values are done solely with the help of an increase in defect density of states when exposed to illumination. For implementing the increase in defect density of states to our model, We consider a homogeneous rise in the defect density in the bulk of the i-layer suggested by Block [73]. When considering the real-time data it shall also be taken into account that,over time the module's heat dissipation property plays an important role in the annealing effect of the formed metastable defects.

In the simulation, we assume that the drift mobility in extended states does not change analogous to [72]. In order to recalculate the DOS at light-soaked states, we take the following approach. The new Density of state distribution, as a function of E, x is given as [72] ,

$$N(x,E)_{\text{degraded state}} = N(x,E)_{\text{as-deposited}} + \Delta N(x,E)_{\text{induced}} \tag{4.8}$$

In a simplified approach of the model by Klaver, we can approximate the recombination density involving the valance band tail approximated independently of the depth of the cell. Here we deviate from the mentioned model and we use the improved defect pool model estimation for the ratio of charged to neutral defects by Powell and Deane [63]. This approximation is essential in our case as we do not define the depth dependency parameters on the calibration of our model.

As a consequence of this, the term $\Delta N(x,E)_{\text{induced}}$ in the equation 4.8 can be approximated as

$$\Delta N(E)_{\text{induced}} = \sum_{n=e,z,h} (C_n - 1) \cdot \cdot N_n(ref, E), \tag{4.9}$$

where the subscripts "e", "z" and "h" denote the negative neutral and positive charge states respectively (refer to explanation in section 4.2.2). C_n is the approximated multiplication factor for the increase in DOS and and *"ref"* is the reference point and initial value at the energy state.

We take the reference point value as the defined defect state density value of our model from calibration. When we simulate the change in C_z we introduce more defects to the middle of the gap at the position of dangling bonds. and C_e,C_h inclusions will add defects near conduction and valance bands respectively. For this modelling, we follow the approach of only varying the z parameter using C_z following the approach of Klaever[72] and studies of Nádaždy et al.[74] and Schumm et. al [75]. This multiplication factor is obtained form careful matching of experimental data and ASA results. Before implementing the study in tandem solar cells, we need to fit the experimental data of light soaking for the HyET model that was calibrated in section 4.4.1.

4.19.2. Matching measured data for single-junction a-Si cells

The multiplication factor for neutral DOS is related to time as $C_z \propto T^A$ where A is less than one. The usual values range from 0.3 to 0.5. This factor has a thermal annealing influence and can vary with module architecture. From the trends observed in light-soaked data of the modules, we have identified the fast degradation phase and slow degradation phase and tried to fit the J_{sc} and FF parameters for the same in this section with the help of a division factor for Cz. Thus the aforementioned relation can be modified as $C_z = K_z T^A$. Thus with careful fittings, we obtain K and A values. Several simulations done are shown in Appendix E.

The single junction cell degradation curves, FF and J_{sc} is fitted using $C_z = 0.7T^{0.4}$ for degradation between 0 to 3300 minutes and from 3300 minutes to 174840 using $C_z = 0.2T^{0.4}$

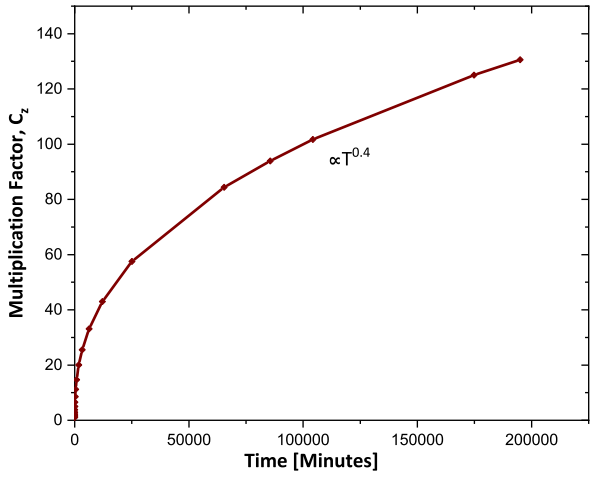

Figure 4.64: Multiplication factor vs Time

This $T^{0.4}$ dependence from the fitted curve vary from some similar studies, which often attributes the C_z value to $T^{0.3}$ [76][72]. Also, we stress that this fit is made considering one parameter (and drift mobility in extended states unchanged) while the Staebler-Wronski effect, in reality, involves multiple variables.

4.19.3. Light soaking on a-Si:H/μc-Si:H tandem solar cell

For focusing on the light soaking effect of tandems, we mainly look at the effect on top cell absorber causing a fall in J_{sc}. To execute this in ASA, the above curve fitted coefficients was incorporated into the top cell DOS. Similar to the a-Si single-junction cells, only defect creation was assumed in the top cell and the reverse process of defect annihilation resulting from temperature annealing is not accounted for. the variations from a single junction that needs special attention shall be the temperature annealing effect. It shall change as a

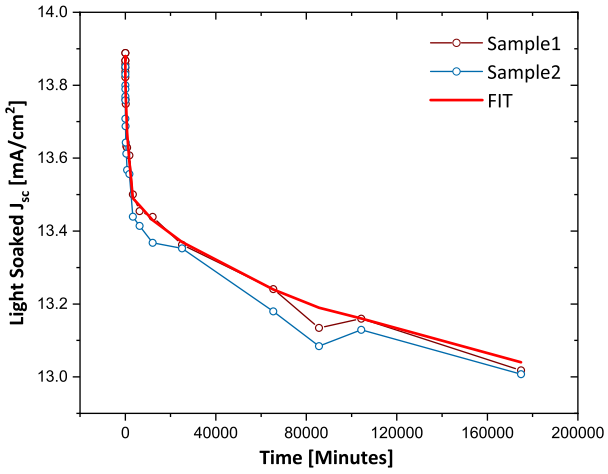

Figure 4.65: J_{SC} Curve fit for light soaking for a-Si Single junction historical data of HyET

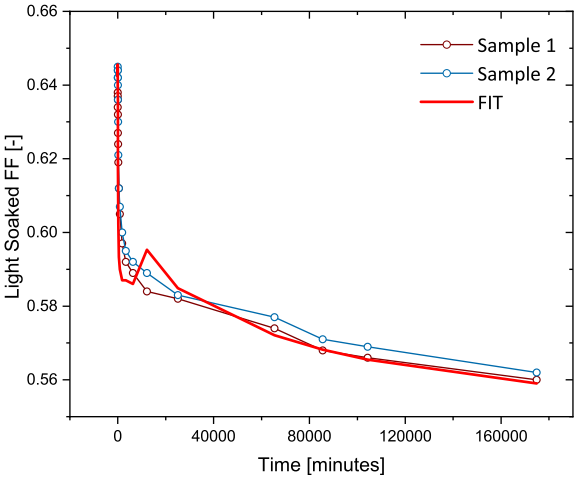

Figure 4.66: FF Curve fit for light soaking for a-Si Single junction historical data of HyET

result of different semiconductor temperature dissipation mechanisms from multiple layers. The attempt to match J_{SC} for the optimised thickness of 156 nm top cell absorber was made.

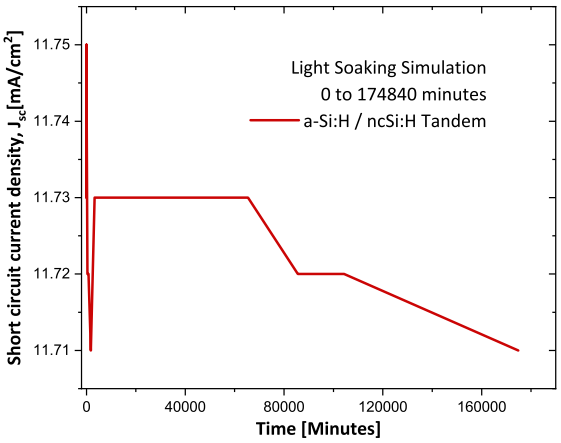

Figure 4.67: Attempted modelling of Jsc light soaking for micromorph tandem.

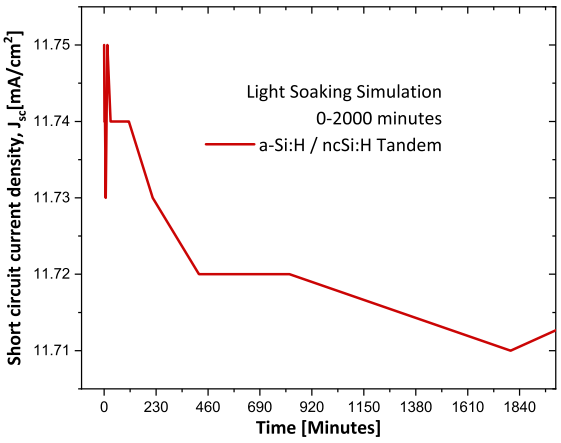

Figure 4.68: Attempted modelling of Jsc light soaking for micromorph tandem 0 to 2000 minutes

Result The attempt to extend the light-soaked values to tandem cells were unsuccessful using the above model and assumptions. The simulated curve is shown in 4.67 and magnified in a range up to 2000 hours in the figure 4.68. These curves do not show a realistic degradation nature and the incorporation to the tandem model cannot be considered successful. Possible reasons for failure can be:

1. Change in DOS value in tandem layers interfering with the model. We apply the trap assisted tunnelling model for all layers for tandem (refer to section 4.5). ASA demands the model to be declared for the whole system (and not specific layers). So TAT model in the a-Si layers which was previously not present for single junctions can cause the issue.

2. Use of thinner layers, the available data was only fitted against one thickness as HyET manufactures modules at 300nm and multi layers in tandem with unable to recreate the effect.

3. The assumption of constant mobility factor in the degradation model not consistent with tandem model which uses FDME.

To identify the exact issue, we need further simulations and studies on the same with help of ASA, looking at sensitivity of each parameter.

5
Conclusions and Outlooks

This thesis investigated the fabrication methods of micromorph tandem solar cells and the possible challenges and alternatives in the processes. With the help of the optoelectronic modelling tool- ASA, the fabricated structure was modelled and analysed to predict the performances.

5.1. Conclusions

5.1.1. Fabrication

Micromorph tandem solar cells were successfully fabricated on flexible aluminium substrates. The new texturing employed (FLAM01) is conformal in nature over the different deposition layers, while the texturing transfer from aluminium to the TCO-Air interface is not satisfactory and needs some further study with TCO depositions.

The initial fabricated cells had a low yield and low performance. The fabrication process has its challenges arising both from the cell structure and materials. The fabricated tandem cells had partial and total shunting issues. On measurement, the n-doped nc – SiO_x layers exhibited 60meV activation energy. This lateral conductivity can bypass the cell scribes leading to cell shunts. As an alternative, the thesis suggests the utilization of a-Si(n) which exhibited 300meV activation energy. When put in practice, this helped to improve the yield. The subcell shunting issue could not be solved and still prevails with fabrication processes.

5.1.2. Modelling

ASA is a powerful tool to study Tandem solar cells, and predict their performances. A plugin was developed on python to enhance the user experience and ease clubbed with a considerable amount of reduction in manpower and time consumption.

A Tandem micromorph model was developed starting from the single junction calibrated models. The ideas of new texturing - FLAM01 and encapsulation was implemented. The model was matched for top and bottom cell currents and optimised for absorber thicknesses, tunnelling recombination junction thicknesses and tunnelling recombination junction doings. The arrived values include: top cell thickness of 156 nm, bottom cell of 2 microns, TRJ n-doped layer of 25nm, p-doped layer of 20nm thickness and donor activation energy 0.25eV and acceptor activation energy of 0.15eV. This performance maximised cell resulted in 11.70mA/cm^2 as the short circuit current density, and 1.356 V_{oc} and efficiency of 12.2%.

The background of performance variation with TRJ layer thickness and dopings were studied in detail. The summary of this study can be put down in one line as - the closer the band states of TRJ layers, the better they are for tunnelling and thereby enhances the performance of the tandems. The possible improvements on the model were studied in the light of fabrication processes, namely the oxygen fraction in silicon oxide layers simulated with the help of real-time measured optical data and bandgap. The p-doped nc – SiO_x layers of 2.0 sccm CO_2 flow was found best for the top cell p layer and p nc – SiO_x at 3.2 sccm CO_2 flow was found better for TRJ doping. In the latter case, a current increase in the top cell at the expense of bottom cell values were observed across top layer thickness combinations. This has the potential to improve the cells in sense of stabilized efficiencies at thinner top cells. To attain this use of a silver back reflector and thicker bottom cells

are suggested in this thesis.

Performance analysis outside standard conditions was simulated in this thesis on ASA. The fall of Voc obtained was 4.9mV/K and the degradation of efficiency from simulated data was 0.058% per kelvin. The conducted spectral response study resulted in the understanding of subcell responses separately for different regions in the spectrum. Finally, on the modelling side, an attempt was made to model light soaking with help of measured data from HyET solar. This data was fitted for single junction cells with dangling bonds variation with a factor $T^{0.4}$. But the extrapolation of this model to the tandem configuration resulted in erroneous values over a wide range of time.

5.2. Outlooks

5.2.1. Fabrication

The main observed performance issue with fabricated models was the low fill factor. In this project, we observed that the n-nc – SiO_x layer is highly laterally conductive. The material is also used as our n layer in the TRJ. Thus experiments with multiple TRJ layers and TRJ layer thicknesses in detail shall be a key to achieve good data sets and reproducible results.

Deposition on a glass substrate can be a good benchmark for understanding the deposition properties and attainable performances of the micromorph solar cells. The issues with nanocrystalline growth might be resulting from the deposition machine.

The back contact sputtering of aluminium can have potentially a negative effect on the cell due to ion bombardment. This shall be studied under SEM, before the total fabrication of the cell. Since the glue interferes with SEM, for good resolution observation the scribe/back contact deposition observation shall be done before adhering them to the PEN carrier. Also with future fabrications, Vacuum thermal deposition of aluminium can be considered as an alternative.

The complete cell fabrication can be done with help of depositions using masks, starting from silicon deposition. These kinds of cells then can be completely isolated from each other with "pillar" type depositions.

5.2.2. Modelling

Primarily, GenPro 4 optical solver coupled with ASA can improve the optical side of the model. But this will require calibration of the single junction models from the beginning.

On the texturing aspect, for the ".cas" input files that we used in this thesis, we assume the texturing totally conformal. We assigned the same texture at multiple interfaces. But this is not the real case. AFM data can be taken at each deposition layer and this real data can be utilized to do a better and precise texture modelling of the tandem cells.

For the performance improvement study, With the help of optical data acquired for n-doped nc – SiO_x layers with their band gap values, investigation on a combined effect of n and p-doped TRJs with different oxygen content can be done.

Looking at the performance assessment, alteration of band gaps with temperature can also be brought into the picture and thus attaining the changes in J_{sc} values. For mimicking the light soaking performances, sensitivity analysis and tuning of the tunnelling parameters inside the model can be a point of interest.

On the last note, the optoelectronic model made in this thesis attains its completion only when the fabricated micromorph cell is successfully measured with good depositions and optical response. Throughout this thesis the deposition machine AMIGO and at sputtering tool at HyET solar has been showing issues. Once the JV parameters and EQE of these cells are attained, fine-tuning of the model parameters shall be done again based on the new values.

Bibliography

[1] UNFCCC, *Kyoto Protocol Reference Manual*, 2008. [Online]. Available: https://unfccc.int/resource/docs/publications/08_unfccc_kp_ref_manual.pdf

[2] N. M. Allen M.R., O.P. Dube, W. Solecki, F. Aragón-Durand, W. Cramer, S. Humphreys, M. Kainuma, J. Kala, Y. Mulugetta, R. Perez, M.Wairiu, and K. Zickfeld, "IPCC Special Report : Global Warming of 1.5°C," pp. 1–27, 2018. [Online]. Available: https://www.ipcc.ch/sr15/chapter/chapter-1/

[3] United Nations, "Paris Agreement," *Conference of the Parties, COP21*, 2015. [Online]. Available: https://unfccc.int/sites/default/files/english_paris_agreement.pdf

[4] REN21, *Renewables 2021 Global Status Report*. Paris, REN21 Secretariat, 2021. [Online]. Available: http://www.ren21.net/resources/publications/

[5] K. L. Chopra, P. D. Paulson, and V. Dutta, "Thin-film solar cells: An overview," *Progress in Photovoltaics: Research and Applications*, vol. 12, no. 2-3, pp. 69–92, 2004.

[6] J. Poortmans and V. Arkhipov, *Thin Film Solar Cells: Fabrication, Characterization and Applications*. John Wiley & Sons, 2006, vol. 18.

[7] T. D. Lee and A. U. Ebong, "A review of thin film solar cell technologies and challenges," *Renewable and Sustainable Energy Reviews*, vol. 70, pp. 1286–1297, 2017.

[8] R. Søndergaard, M. Hösel, D. Angmo, T. T. Larsen-Olsen, and F. C. Krebs, "Roll-to-roll fabrication of polymer solar cells," *Materials Today*, vol. 15, no. 1-2, pp. 36–49, 2012. [Online]. Available: http://dx.doi.org/10.1016/S1369-7021(12)70019-6

[9] "Thin film production process," HyET Solar. [Online]. Available: https://www.hyetsolar.com/production-process/

[10] "Thin film technology," HyET Solar. [Online]. Available: https://www.hyetsolar.com/technology/Thin-Film-Solar/

[11] *Flexible Lightweight AdvancedMaterials InNextGeneration Of PV: FlamingoPV*. Project Description, Delft University of Technology and HyET Solar, August 2018.

[12] R. Schropp, E. Middelman, E. Andel, van, H. Meiling, C. Werf, van der, P. Peters, L. Jonge-Meschaninova, de, J. Winkeler, R. Severens, M. Zeman, M. Sanden, van de, A. Kuijpers, C. Spee, and G. Jongerden, "Novel superstrate process for textured sno2:f/p+-i-n+ amorphous silicon solar cells suitable for rol-to-roll deposition," in *Proceedings of the 2nd World Conference on Photovoltaic Solar Energy Conversion, Vienna, 6-10 July 1998*, 1998, 2nd World Conference on Photovoltaic Solar Energy Conversion ; Conference date: 06-07-1998 Through 10-07-1998.

[13] M. Van den Donker, A. Gordijn, H. Stiebig, F. Finger, B. Rech, B. Stannowski, R. Bartl, E. Hamers, R. Schlatmann, and G. Jongerden, "Flexible amorphous and microcrystalline silicon tandem solar modules in the temporary superstrate concept," *Solar energy materials and solar cells*, vol. 91, no. 7, pp. 572–580, 2007.

[14] K. Jäger, J. Lenssen, P. Veltman, and E. Hamers, "Large-area production of highly efficient flexible lightweight thin-film silicon pv modules," in *Proc. 28th European Photovoltaic Solar Energy Conf., Paris, France*, 2013, pp. 2164–2169.

[15] A. Gordijn, M. Van Den Donker, F. Finger, E. Hamers, G. Jongerden, W. Kessels, R. Bartl, A. van Mol, J. Rath, B. Rech *et al.*, "Flexible a-si/μc-si tandem modules in the helianthos project," in *2006 IEEE 4th World Conference on Photovoltaic Energy Conference*, vol. 2. IEEE, 2006, pp. 1716–1719.

[16] The Laser interconnection process - HyET Internal documents- HyET Solar, 2020.

[17] A. H. Smets, K. Jäger, O. Isabella, R. A. Swaaij, and M. Zeman, *Solar Energy: The physics and engineering of photovoltaic conversion, technologies and systems*. UIT Cambridge Ltd., 2016.

[18] D. A. Neamen, *Semiconductor physics and devices: basic principles*, 4th ed. New York, NY: McGraw-Hill,, 2012.

[19] A. Einstein, "Über einen die erzeugung und verwandlung des lichtes betreffenden heuristischen gesichtspunkt," *Annalen der Physik*, vol. 322, no. 6, pp. 132–148, 1905. [Online]. Available: https://onlinelibrary.wiley.com/doi/abs/10.1002/andp.19053220607

[20] B. R. Wheaton, "Photoelectric effect," in *Compendium of Quantum Physics*. Springer, 2009, pp. 472–475.

[21] M. A. Green, *Solar cells: operating principles, technology, and system applications*. Prentice-Hall, Inc., 1 1982.

[22] G. R. Fowles, *Introduction to modern optics*. Courier Corporation, 1989.

[23] U. W. Peter Würfel, *Physics of Solar Cells: From Basic Principles to Advanced Concepts*, 3rd ed. Wiley-VCH, 2016.

[24] D. F. Swinehart, "The beer-lambert law," *Journal of chemical education*, vol. 39, no. 7, p. 333, 1962.

[25] W. Pauli, "Über den zusammenhang des abschlusses der elektronengruppen im atom mit der komplexstruktur der spektren," *Zeitschrift für Physik*, vol. 31, no. 1, pp. 765–783, 1925.

[26] I. G. Kaplan, "Pauli exclusion principle and its theoretical foundation," *arXiv preprint arXiv:1902.00499*, 2019.

[27] H. Overhof, "Fundamental concepts in the physics of amorphous semiconductors," *Journal of non-crystalline solids*, vol. 227, pp. 15–22, 1998.

[28] M. A. Green, "Accuracy of analytical expressions for solar cell fill factors," *Solar Cells*, vol. 7, no. 3, pp. 337–340, 1982.

[29] N. M. Shannan, N. Z. Yahaya, and B. Singh, "Two diode model for parameters extraction of pv module," pp. 260–264, 2014.

[30] M. Fortes, E. Comesana, J. Rodriguez, P. Otero, and A. Garcia-Loureiro, "Impact of series and shunt resistances in amorphous silicon thin film solar cells," *Solar Energy*, vol. 100, pp. 114–123, 2014.

[31] R. N. Hall, "Electron-hole recombination in germanium," *Physical review*, vol. 87, no. 2, p. 387, 1952.

[32] W. Shockley and W. Read Jr, "Statistics of the recombinations of holes and electrons," *Physical review*, vol. 87, no. 5, p. 835, 1952.

[33] J. Yang, A. Banerjee, and S. Guha, "Amorphous silicon based photovoltaicsfrom earth to the final frontier," *Solar energy materials and solar cells*, vol. 78, no. 1-4, pp. 597–612, 2003.

[34] M. M. de Wild-Scholten, "Energy payback time and carbon footprint of commercial photovoltaic systems," *Solar Energy Materials and Solar Cells*, vol. 119, pp. 296–305, 2013.

[35] F. Meillaud, A. Shah, C. Droz, E. Vallat-Sauvain, and C. Miazza, "Efficiency limits for single-junction and tandem solar cells," *Solar energy materials and solar cells*, vol. 90, no. 18-19, pp. 2952–2959, 2006.

[36] A. Shah, *Thin-film silicon solar cells*. EPFL press Lausanne, 2010, vol. 68.

[37] J.A.Willemen, "Modelling of amorphous silicon single- and multi-junction solar cells," no. 18-19, pp. 2952–2959, 2006. [Online]. Available: http://resolver.tudelft.nl/uuid:0771d543-af5f-4579-8a35-0b68d34a1334

[38] M. Zeman and J. Krc, "Electrical and optical modelling of thin-film silicon solar cells," *MRS Online Proceedings Library (OPL)*, vol. 989, 2007.

[39] M. Zeman, J. Willemen, L. Vosteen, G. Tao, and J. Metselaar, "Computer modelling of current matching in a-si: H/a-si: H tandem solar cells on textured tco substrates," *Solar Energy Materials and Solar Cells*, vol. 46, no. 2, pp. 81–99, 1997.

[40] P. R. i Cabarrocas, "Deposition techniques and processes involved in the growth of amorphous and microcrystalline silicon thin films," in *Physics and technology of amorphous-crystalline heterostructure silicon solar cells*. Springer, 2012, pp. 131–160.

[41] P. Babal, "Doped nanocrystalline silicon oxide for use as (intermediate) reflecting layers in thin-film silicon solar cells," *Ph.D. Thesis*, 2014. [Online]. Available: https://doi.org/10.4233/uuid:448b63f4-2128-409e-bbd8-866e720116ed

[42] A. Matsuda, "Amorphous and microcrystalline silicon," in *Springer handbook of electronic and photonic materials*, S. Kasap and P. Capper, Eds. Springer, 2017, ch. 25, pp. 573–586.

[43] R. Platz, S. Wagner, C. Hof, A. Shah, S. Wieder, and B. Rech, "Influence of excitation frequency, temperature, and hydrogen dilution on the stability of plasma enhanced chemical vapor deposited a-si: H," *Journal of applied physics*, vol. 84, no. 7, pp. 3949–3953, 1998.

[44] D. Tsu, B. Chao, S. Ovshinsky, S. Guha, and J. Yang, "Effect of hydrogen dilution on the structure of amorphous silicon alloys," *Applied physics letters*, vol. 71, no. 10, pp. 1317–1319, 1997.

[45] S. Guha, J. Yang, A. Banerjee, B. Yan, and K. Lord, "High quality amorphous silicon materials and cells grown with hydrogen dilution," *Solar energy materials and solar cells*, vol. 78, no. 1-4, pp. 329–347, 2003.

[46] A. Shah, "Thin-film silicon solar cells," in *Practical Handbook of Photovoltaics*. Elsevier, 2012, pp. 209–281.

[47] K. Ellmer, "Magnetron sputtering of transparent conductive zinc oxide: relation between the sputtering parameters and the electronic properties," *Journal of Physics D: Applied Physics*, vol. 33, no. 4, p. R17, 2000.

[48] A. D. Elliott, "Confocal microscopy: Principles and modern practices," *Current Protocols in Cytometry*, vol. 92, no. 1, p. e68, 2020. [Online]. Available: https://currentprotocols.onlinelibrary.wiley.com/doi/abs/10.1002/cpcy.68

[49] D. Rajagopal, "Modulated surface texturing on temporary aluminium substrate for flexible thin-film solar cells," *MSc. Thesis*, 2020.

[50] A. M. Shah, "Modulated surface texturing on temporary aluminium substrate for flexible thin-film solar cells," *MSc. Thesis*, Expected completion: August 2021.

[51] Y. Zhao, P. Procel, C. Han, L. Mazzarella, G. Yang, A. Weeber, M. Zeman, and O. Isabella, "Design and optimization of hole collectors based on nc-siox: H for high-efficiency silicon heterojunction solar cells," *Solar Energy Materials and Solar Cells*, vol. 219, p. 110779, 2021.

[52] E. Spaans, "Optimisation of a-si:h/µc-si:h tandem solar cell on flexible al substrates," *MSc. thesis*, 2020.

[53] H. Tan, E. Moulin, F. T. Si, J.-W. Schüttauf, M. Stuckelberger, O. Isabella, F.-J. Haug, C. Ballif, M. Zeman, and A. H. Smets, "Highly transparent modulated surface textured front electrodes for high-efficiency multijunction thin-film silicon solar cells," *Progress in Photovoltaics: Research and Applications*, vol. 23, no. 8, pp. 949–963, 2015.

[54] S. B. Nawaratne, "Nanocrystalline silicon solar cells on flexible al substrates," *MSc. Thesis*, 2020.

[55] I. Lombardero and C. Algora, "Understanding the influence of shunts in the i–v curves and electroluminescence of multijunction solar cells," *Solar Energy Materials and Solar Cells*, vol. 204, p. 110236, 2020.

[56] A. Shah, F. Sculati-Meillaud, Z. Berényi, O. Ghahfarokhi, and R. Kumar, "Diagnostics of thin-film silicon solar cells and solar panels/modules with variable intensity measurements (vim)," *Solar energy materials and solar cells*, vol. 95, no. 1, pp. 398–403, 2011.

[57] J. Löffler, A. Gordijn, R. Stolk, H. Li, J. Rath, and R. Schropp, "Amorphous and micromorphsilicon tandem cells with high open-circuit voltage," *Solar energy materials and solar cells*, vol. 87, no. 1-4, pp. 251–259, 2005.

[58] K. Jäger, M. Fischer, R. Van Swaaij, and M. Zeman, "A scattering model for nano-textured interfaces and its application in opto-electrical simulations of thin-film silicon solar cells," *Journal of Applied Physics*, vol. 111, no. 8, p. 083108, 2012.

[59] R. Santbergen, T. Meguro, T. Suezaki, G. Koizumi, K. Yamamoto, and M. Zeman, "Genpro4 optical model for solar cell simulation and its application to multijunction solar cells," *IEEE journal of photovoltaics*, vol. 7, no. 3, pp. 919–926, 2017.

[60] M. Zeman, J. van den Heuvel, M. Kroon, J. Willemen, B. Pieters, J. Krc, and S. Solntsev, "Manual : Advanced Semiconductor Analysis: opto-electronic simulator for amorphous and crystalline semiconductor devices," 2013.

[61] R. E. Schropp, M. Zeman *et al.*, *Amorphous and microcrystalline silicon solar cells: modeling, materials and device technology*. Springer, 1998, vol. 8.

[62] B. E. Pieters, "Characterization of thin-film silicon materials and solar cells through numerical modeling," 2008. [Online]. Available: http://resolver.tudelft.nl/uuid:83bc5ff4-8e33-4962-9014-68cfbad8226f

[63] M. Powell and S. Deane, "Improved defect-pool model for charged defects in amorphous silicon," *Physical Review B*, vol. 48, no. 15, p. 10815, 1993.

[64] ——, "Defect-pool model and the hydrogen density of states in hydrogenated amorphous silicon," *Physical Review B*, vol. 53, no. 15, p. 10121, 1996.

[65] *Subprocess management*, Python.3.9.6 Documentation. [Online]. Available: https://docs.python.org/3/library/subprocess.html

[66] *Pandas DataFrame*, Python Pandas Documentation. [Online]. Available: https://pandas.pydata.org/docs/reference/frame.html#

[67] G. Hurkx, D. Klaassen, and M. Knuvers, "A new recombination model for device simulation including tunneling," *IEEE Transactions on electron devices*, vol. 39, no. 2, pp. 331–338, 1992.

[68] B. Hill, "Solar cell devices physics: by steven j. fonash; published by academic press, london, march 1982; 332 pp; price,£ 23.20; isbn 0-12-261980-3," 1983.

[69] A. Anchalia, "Data analysis of an outdoor a-si:h pv system," *MSc. Thesis*, Expected completion: August 2021.

[70] E. Aydin, T. G. Allen, M. De Bastiani, L. Xu, J. Ávila, M. Salvador, E. Van Kerschaver, and S. De Wolf, "Interplay between temperature and bandgap energies on the outdoor performance of perovskite/silicon tandem solar cells," *Nature Energy*, vol. 5, no. 11, pp. 851–859, 2020.

[71] M. Gostein and L. Dunn, "Light soaking effects on photovoltaic modules: Overview and literature review," in *2011 37th IEEE Photovoltaic Specialists Conference*. IEEE, 2011, pp. 003 126–003 131.

[72] A. Klaver and R. Van Swaaij, "Modeling of light-induced degradation of amorphous silicon solar cells," *Solar Energy Materials and Solar Cells*, vol. 92, no. 1, pp. 50–60, 2008.

[73] M. Block, "Defect distribution in a-si: H-pin solar cells before and after degradation," *Journal of non-crystalline solids*, vol. 164, pp. 701–704, 1993.

[74] V. Nádaždy and M. Zeman, "Origin of charged gap states in a-si:h and their evolution during light soaking," *Phys. Rev. B*, vol. 69, p. 165213, Apr 2004. [Online]. Available: https://link.aps.org/doi/10.1103/PhysRevB.69.165213

[75] G. Schumm, "Chemical equilibrium description of stable and metastable defect structures in a-si: H," *Physical Review B*, vol. 49, no. 4, p. 2427, 1994.

[76] M. Stutzmann, W. Jackson, and C. Tsai, "Kinetics of the staebler–wronski effect in hydrogenated amorphous silicon," *Applied physics letters*, vol. 45, no. 10, pp. 1075–1077, 1984.

A

ASA Multi-Run

The below given python file is the back-end of ASA Multi Run plug in it requires a special cas file to run as given in Appendix B. To make use of the plugin change the "CAS FILE NAME " and "RUN NAME" in the file. The multi run can handle, usual cas files with two lines left blank at the top, one parameter varied over a range, two parameters varied over a range, one parameter/two parameters at a time without range. The python file needs to be already kept in the same directory as the .exe and .cas files of ASA.
Please refer to the commend legend, at the end of the program combined with the flow chart in figure 4.4 to identify the steps inside the program.

```
# ASA MULTI RUN
# **************
# Author : Govind Padmakumar , TU Delft.
# Date : 06/04/2021
# ****************************************

# The following python program is meant to act as a plug-in for ASA Software.
# The plug-in is useful to execute ASA
# with multiple parameters & for multiple values.

# DESCRIPTION Of Plug In :
# The py file handles an input CAS file of a specific format.
# CAS file has first two lines  dedicated for information on variable parameters.
# The lines start with " C " and has parameters with editable text and variable
# values separated by the keywords for each variable being $XXXX$ and $YYYY$
# (Same in this py file).
# Output of each simulation is stored in folders.
# Consolidated output made into one single file
# ( same files in .dat and .xls formats).

# ********************************************************************************

# Edit the input CAS file name in the following line
# Give RUN name to identify the simulation !
CAS_FILE_NAME = "CASFILE.cas"
RUN_NAME = "RUN_NAME"

# ********************************************************************************

import os  # noqa: E402
import fileinput  # noqa: E402
import shutil  # noqa: E402
import subprocess  # noqa: E402
import numpy as np  # noqa: E402
import datetime  # noqa: E402
```

```
import math  # noqa: E402
import re  # noqa: E402
import pandas as pd  # noqa: E402
from tabulate import tabulate  # noqa: E402

# Function to call ASA & to set the input .cas file to its original X Y variable form
def EXECUTE_ASA(CAS_FILE):
    print("\n ********************** INITIALISING ASA **********************")
    subprocess.call(['ASA.exe', CAS_FILE])
    shutil.copyfile(CAS_FILE_NAME + '.bak', CAS_FILE_NAME)


# A function to avoid the float error values in python.
# The function truncates a value to two decimal places
def trunc_float_error(value_to_truncate, digits) -> float:
    scaler_value = 10.0 ** digits
    return math.trunc(scaler_value * value_to_truncate) / scaler_value


# Function to extract Solpar Data from different folders
# taking only each parameters separately.
def SOLPAR_EXTRACT(directory, Master_df, X, Y=0):
    for path, dirs, files in os.walk(directory):
        for filename in files:
            if filename.startswith("solpar"):  # identifying the solpar file
                solpar_path = os.path.join(path, filename)
                with open(solpar_path, 'r') as solpar_file: # opening solpar
                                                            # file using path
                    data = solpar_file.read()
                    if 'Voc' in data:
            # print(data) #Extraction of solpar data each data separated

                        voc = re.search(r"Voc   =(.*?)V ---", data).group(1)
                        isc = re.search(r"Isc   =(.*?) A/m", data).group(1)
                        jsc = float(isc) / (-10)
                        vmpp = re.search(r"Vpmax =(.*?)V ---", data).group(1)
                        impp = re.search(r"Ipmax =(.*?)A/m", data).group(1)
                        jmpp = float(impp) / (-10)
                        pmpp = re.search(r"Pmax  =(.*?)W/m", data).group(1)
                        ff = re.search(r"FF    =(.*?)---", data).group(1)
                    else:
                        [voc, jsc, vmpp, jmpp, pmpp, ff] = [0, 0, 0, 0, 0, 0]

                    extracted_Solpar = pd.DataFrame(
                        [[X, Y, float(voc), float(isc), float(vmpp), float(impp),
                                                 float(pmpp), float(ff)]],
                        columns=["X(Parameter)", "Y(Paramter)", "Voc(V)",
                                 "Jsc(mA/cm^2)", "Vmax(V)",
                                 "Jmax(mA/cm^2)", "Pmax(W/m^2)", "FF"])
            # Adding the extracted solpar data of current run to main master data frame
                    Master_df = Master_df.append(extracted_Solpar)

            # Adding the Solpar data extracted for this execution to the dat file
                    # print(Solpar_data)        #uncomment to see the solpar of each run
                    with open('Solpar_' + RUN_NAME + '.dat', 'a') as dat_file_out:
                        dat_file_out.write(tabulate([[X, Y, voc, jsc,
```

```
                                                    vmpp, jmpp, pmpp, ff]]))
    return Master_df  # Returns the master file with updated solpar values

# Opens the cas file for operation and execution
cas_in = open(CAS_FILE_NAME)
print("\n ********************** READING FILE **********************")

# Taking the line by line values : extracting first two lines
for parameter_spec, line in enumerate(cas_in):
    if parameter_spec == 0:  # Line 1 Parameter X
        [parameter_X_line] = [line]
        # print(parameter_X_line)
    if parameter_spec == 1:  # Line 2 Parameter Y
        [parameter_Y_line] = [line]
        # print(parameter_Y_line)
cas_in.close()

# CASE 0 : NORMAL CAS FILE EXECUTION !

if '#' in parameter_X_line and '#' in parameter_Y_line:

    [spec_values_X, spec_values_Y] = [parameter_X_line.split('#'),
                                      parameter_Y_line.split('#')]

    [parameter_X, start_value_X, end_value_X, skip_value_X] = \
                    [spec_values_X[1], float(spec_values_X[2]),
                    float(spec_values_X[3]) + float(spec_values_X[4]),
                    float(spec_values_X[3])]
    if spec_values_Y[0] != '\n':
        [parameter_Y, start_value_Y, end_value_Y, skip_value_Y] = \
                    [spec_values_Y[1], float(spec_values_Y[2]),
                    float(spec_values_Y[3]) + float(spec_values_Y[4]),
                    float(spec_values_Y[3])]

# To avoid the solpar data extracted to a " .dat File "
    # comment the following line : these give heading for the dat file

    # Solpar_table= tabulate([], headers=["X", "Y", "Voc", "Isc",
    #                                     "Vmax","Imax","Pmax","FF"])
    with open('Solpar_' + RUN_NAME + '.dat', 'w') as f:
        f.write(tabulate([], headers=["X(Parameter)", "Y(Paramter)",
                                      "Voc(V)", "jsc(mA/cm^2)", "Vmax(V)",
                                      "jmax(mA/cm^2)", "Pmax(W/m^2)", "FF"]))

# The following lines has Solpar data extracted to a xls file via data frame
    Solpar_data = pd.DataFrame([], columns=["X(Parameter)", "Y(Paramter)",
                                            "Voc(V)","jsc(mA/cm^2)", "Vmax(V)",
                                            "jmax(mA/cm^2)","Pmax(W/m^2)", "FF"])

    # CASE 1 : Only One Parameter Change - X parameter only.

    # CASE 1A: Single parameter, Single Value ( only one value and step value = 0 ).
    if spec_values_Y[0] == '\n':  # Y[0] ==  \n  means second line blank

        if skip_value_X == 0:
            toSearch_X = parameter_X  # 1
```

```
            toReplace_X = parameter_X.replace("$XXXX$", str(start_value_X))  # 2

            save_directory = RUN_NAME + "_X_" + str(start_value_X)  # 3
            os.mkdir(save_directory)

            with fileinput.FileInput(CAS_FILE_NAME, inplace=True, backup='.bak')\
                                                                    as file:  # 6
                for line in file:
                    print(
                        line.replace(toSearch_X, toReplace_X).
                            replace("DIRECTORY", save_directory).
                            replace("a$X$_para$Y$", str(start_value_X)), end='')  # 4

                EXECUTE_ASA(CAS_FILE_NAME)  # 5
            Solpar_data = SOLPAR_EXTRACT(save_directory, Solpar_data, start_value_X)

        # CASE 1B: Single parameter, Range of values.
        else:
            for x in np.arange(start_value_X, end_value_X, skip_value_X):
                x = trunc_float_error(x, 2)  # 7

                toSearch_X = parameter_X  # 1
                toReplace_X = parameter_X.replace("$XXXX$", str(x))  # 2
                save_directory = RUN_NAME + "_X_" + str(x)  # 3
                os.mkdir(save_directory)

                with fileinput.FileInput(CAS_FILE_NAME, inplace=True,
                                         backup='.bak') as file:  # 6
                    for line in file:
                        print(line.replace(toSearch_X, toReplace_X)
                            .replace("DIRECTORY", save_directory)
                            .replace("a$X$_para$Y$", str(x)), end='')  # 4

                    EXECUTE_ASA(CAS_FILE_NAME)  # 5
                Solpar_data = SOLPAR_EXTRACT(save_directory, Solpar_data, x)

    # CASE 2 : Two Parameters Change - X AND Y parameters
    if spec_values_Y[0] != '\n':

        # CASE 2A: Two parameters, Both Single Value ( ie, One combination X,Y ).
        if skip_value_X == 0 and skip_value_Y == 0:
            [toSearch_X, toSearch_Y] = [parameter_X, parameter_Y]  # 1 # 2
            [toReplace_X, toReplace_Y] = [parameter_X
                                          .replace("$XXXX$", str(start_value_X)),
                                          parameter_Y
                                          .replace("$YYYY$", str(start_value_Y))]
            save_directory = RUN_NAME + "_X_" + str(start_value_X) \
                                                + "_Y_" + str(start_value_Y)  # 3
                                                    os.mkdir(save_directory)

            with fileinput.FileInput(CAS_FILE_NAME, inplace=True, backup='.bak') \
                                                            as cas_input:  # 6
                for x_parameter_line in cas_input:
                    print(
                        x_parameter_line.replace(toSearch_X, toReplace_X)
                            .replace(toSearch_Y, toReplace_Y)
```

```
                        .replace("DIRECTORY", save_directory)
                        .replace("a$X$", str(start_value_X))
                        .replace("a$Y$",str(start_value_Y)),end='')  # 4
                EXECUTE_ASA(CAS_FILE_NAME)  # 5
            Solpar_data = SOLPAR_EXTRACT(save_directory, Solpar_data,
                                         start_value_X, start_value_Y)

        # CASE 2B : Two parameters, Both has range of values.
        else:
            for x in np.arange(start_value_X, end_value_X, skip_value_X):
                x = trunc_float_error(x, 2)  # 7
                toSearch_X = parameter_X  # 1
                toReplace_X = parameter_X.replace("$XXXX$", str(x))  # 2

                for y in np.arange(start_value_Y, end_value_Y, skip_value_Y):
                    y = trunc_float_error(y, 2)  # 7

                    toSearch_Y = parameter_Y  # 1
                    toReplace_Y = parameter_Y.replace("$YYYY$", str(y))  # 2

                    save_directory = RUN_NAME + "_X_" + str(x) + "_Y_" + str(y)  # 3
                                                        os.mkdir(save_directory)

                    with fileinput.FileInput(CAS_FILE_NAME, inplace=True,
                                             backup='.bak') as cas_input:  # 6
                        for x_parameter_line in cas_input:
                            print(
                                x_parameter_line.replace(toSearch_X, toReplace_X)
                                    .replace(toSearch_Y,toReplace_Y)
                                    .replace("DIRECTORY", save_directory)
                                    .replace("a$X$", str(x))
                                    .replace("a$Y$", str(y)),end='')  # 4

                        EXECUTE_ASA(CAS_FILE_NAME)  # 5
                    Solpar_data = SOLPAR_EXTRACT(save_directory, Solpar_data, x, y)

    # Exporting the extracted solpar data to excel sheet
    Solpar_data.to_excel(r'Solpar_' + RUN_NAME + '.xls', index=False)

    # COMMENT REFERENCE
    # 1 Text to be searched.
    # 2 Text with value replaced for keyword $XXXX$ OR $YYYY$
    # in CAS file (IN-PLACE REPLACEMENT).
    # 3 Directory name to save the output includes the value identify the run.
    # 4 Replacing the directory name in the cas file for keyword
    # "DIRECTORY" in CAS file (IN-PLACE REPLACEMENT).
    # 5 Call for ASA execution function.
    # 6 The replacement is in-place replacement and .bak file
    # is original file input without any change
    # 7 The value of floats can have error when converting binary values,
    # so needs to be truncated for smooth execution.

#CASE 0 : NORMAL ASA EXECUTION USUAL CAS FILE
else:
    time_run = datetime.datetime.now().strftime('%Y-%m-%d %H:%M:%S')
    save_directory = RUN_NAME + ''.join(j for j in time_run if j.isalnum())
```

```
os.mkdir(save_directory)
with fileinput.FileInput(CAS_FILE_NAME, inplace=True, backup='.bak')\
                                                        as file:  # 6
    for line in file:
        print( line.replace("DIRECTORY",save_directory)
               .replace("para$X$_para$Y$",RUN_NAME), end='')  # 4
    EXECUTE_ASA(CAS_FILE_NAME)
```

B

ASA Multi-Run Input .CAS file

The first two lines of the .cas file is what the automation tool reads. The below cas file is aimed at the variation of thicknesses in the absorber layers. the parameter 1 to be changed is given $XXXX$ and the other variable parameter is $YYYY$. The demonstrated variations are from 100 to 250 with a change in step 15s and for the parameter 2, 1000 to 2000 with a step of 50. the hash symbol used separates the values and the middle value is the step size. The AMR plug in can also run the usual cas files without any ranges or changes, provided the first two lines in the cas file remains blank.

Once the value is kept zero for a parameter, the plugin changes to other parameter variation over the specified range. Also this can be achieved using total removal of the second line. The para$X$_para$Y$ command areas are for identification of the results and these are replaced in plug in. "DIRECTORY" is replaced in the program and given the "RUN NAME" provided in the AMR plugin either combined with X and Y numbers or with the time and date of execution in case of normal cas files.

```
C #grid[2]      d=$XXXX$e-9 #100#15#250#;
C #grid[5]      d=$YYYY$e-9 #1000#100#2000#;


C ASA input Cas file for top cell in micromorph configuration Tandem device;
C Author : Govind Padmakumar;
C Cell structure made as a continuation of work done by E. Spaans;
C in 2019-20 as a part of Flamingo PV;
C Structural changes include the p,n layers changed to;
C nano crystalline silicon oxide materials.;
C from previous work by E. Spaans with a-SiC as a-Si(n) as top cell p / n layer;
C calibrated against HyET model;
C Bottom cell caliberated against H. Tans nc-Si:H pin cell by erik spaans;
C Model in this ASA CAS file is not calibrated/validated experimentally as the cells are ;
C not successfully fabricated due to constrains in the processes.;
C The interface used in this model is FLAM01 texturing Developed by ;
C D. Rajgopal as a part of Flamingo PV;
C date : 19/04/2021 ;

C DEVICE DEFINITION;

layers electrical=6 front=6 back=2;
grid[f.1] d=25e-6 ;
grid[f.2] d=80e-6;
grid[f.3] d=25e-6 ;
grid[f.4] d=75e-6;
grid[f.5] d=700.0e-9;
grid[f.6] d=20.0e-9;
```

```
grid[1]     d=10e-9 spaces=20;
grid[2]     d=$XXXX$e-9 spaces=200;

grid[3]     d=25e-9 spaces=40;
grid[4]     d=20e-9 spaces=40;

grid[5]     d=$YYYY$e-9 dx.t=1e-9 dx.c=30e-9 dx.b=1e-9;
grid[6]     d=50.0e-9 dx.t=1e-9;

grid[b.1]   d=80e-9;
grid[b.2]   d=300.0e-9;

C OPTICAL PARAMETERS OF LAYERS AND INTERFACES;

C Interface 1;
optical[f.1] lnk.file=etfe_FLAM.in incoherent;
optical[f.2] lnk.file=glue_FLAM_1.in;
optical[f.3] lnk.file=etfe_FLAM.in;
optical[f.4] lnk.file=glue_FLAM_2.in;
optical[f.5] lnk.file=FTO_FLAM.in;                  C front TCO;
optical[f.6] lnk.file=AZO_FLAM.in;        C AZO buffer layer;

C Interface 3;
optical[1]      lnk.file=nc-SiOx(p)_FLAM.in;           C p-ucSi;
optical[2]      lnk.file=a-Si(i)_FLAM.in;        C i-layer;
optical[3]      lnk.file=nc-SiOx(n)_FLAM.in;           C n-ucSi;

C Interface 6;
optical[4]      lnk.file=nc-SiOx(p)_FLAM.in;           C p-ucSi;
optical[5]      lnk.file=nc-Si(i)_FLAM.in;             C i-ucSi;
optical[6]      lnk.file=nc-SiOx(n)_FLAM.in;           C n-ucSi;

C Interface 9;
optical[b.1] lnk.file=AZO_FLAM.in;         C back TCO;
optical[b.2] lnk.file=Al_FLAM.in;         C back contact;

C Interface Data;

interface[i.5]  adf.h.rf = cossq adf.h.rb = cossq adf.h.tf = cossq adf.h.tb = cossq ;
interface[i.5]  adf.s.rf = cossq adf.s.rb = cossq adf.s.tf = cossq adf.s.tb = cossq ;
interface[i.5]  afm.file = FLAM01.in afm.size=20.0e-6;

interface[i.7]  adf.h.rf = cossq adf.h.rb = cossq adf.h.tf = cossq adf.h.tb = cossq ;
interface[i.7]  adf.s.rf = cossq adf.s.rb = cossq adf.s.tf = cossq adf.s.tb = cossq ;
interface[i.7]  afm.file = FLAM01.in afm.size=20.0e-6;

interface[i.10]  adf.h.rf = cossq adf.h.rb = cossq adf.h.tf = cossq adf.h.tb = cossq ;
interface[i.10]  adf.s.rf = cossq adf.s.rb = cossq adf.s.tf = cossq adf.s.tb = cossq ;
interface[i.10]  afm.file = FLAM01.in afm.size=20.0e-6;

interface[i.12]  adf.h.rf = cossq adf.h.rb = cossq adf.h.tf = cossq adf.h.tb = cossq ;
interface[i.12]  adf.s.rf = cossq adf.s.rb = cossq adf.s.tf = cossq adf.s.tb = cossq ;
interface[i.12]  afm.file = FLAM01.in afm.size=20.0e-6;

interface[i.14]  adf.h.rf = cossq adf.h.rb = cossq adf.h.tf = cossq adf.h.tb = cossq ;
interface[i.14]  adf.s.rf = cossq adf.s.rb = cossq adf.s.tf = cossq adf.s.tb = cossq ;
```

```
interface[i.14]  afm.file = FLAM01.in afm.size=20.0e-6;


C MATERIAL PARAMETERS OF LAYERS;

doping[1] e.act.acc=0.50;
doping[3] e.act.don=0.25;
doping[4] e.act.acc=0.15;
doping[6] e.act.don=0.10;

bands[1] e.mob=1.90 chi=4.000 nc=4.0e26 nv=4.0e26 epsilon=11.9;
bands[2] e.mob=1.70 chi=4.025 nc=2.0e26 nv=2.0e26 epsilon=11.9;

bands[3] e.mob=1.75 chi=4.275 nc=4.0e26 nv=4.0e26 epsilon=11.9;
bands[4] e.mob=1.90 chi=4.000 nc=4.0e26 nv=4.0e26 epsilon=11.9;

bands[5] e.mob=1.12 chi=4.000 nc=2.5e25 nv=2.5e25 epsilon=11.9;
bands[6] e.mob=1.75 chi=4.275 nc=4.0e26 nv=4.0e26 epsilon=11.9;

mobility[1] mu.e=10.0e-4   mu.h=1.0e-4;
mobility[2] mu.e=20.0e-4   mu.h=5.0e-4;

mobility[3] mu.e=10.0e-4   mu.h=1.0e-4;
mobility[4] mu.e=10.0e-4   mu.h=1.0e-4;

mobility[5] mu.e=75.0e-4   mu.h=30.0e-4;
mobility[6] mu.e=10.0e-4   mu.h=1.0e-4;

C DENSITY OF STATES PARAMETERS OF LAYERS;

vbtail[1] levels=50 e.range=0.9 c.neut=0.7e-15 c.pos=0.7e-15 n.emob=1.0e28 e.char=0.085;
vbtail[2] levels=20 c.neut=0.7e-15 c.pos=0.7e-15 e.range=1.0 n.emob=4e27 e.char=0.05;

vbtail[3] levels=50 e.range=0.9 c.neut=0.7e-15 c.pos=0.7e-15 n.emob=1.0e28 e.char=0.090;
vbtail[4] levels=50 e.range=0.9 c.neut=0.7e-15 c.pos=0.7e-15 n.emob=1.0e28 e.char=0.085;

vbtail[5] levels=50 e.range=0.9 c.neut=0.7e-15 c.pos=0.7e-15 n.emob=2.0e25 e.char=0.015;
vbtail[6] levels=50 e.range=0.9 c.neut=0.7e-15 c.pos=0.7e-15 n.emob=1.0e28 e.char=0.090;

cbtail[1] levels=50 e.range=0.9 c.neut=0.7e-15 c.neg=0.7e-15 n.emob=1.0e28 e.char=0.080;
cbtail[2] levels=15 c.neut=0.7e-15 c.neg=0.7e-15 e.range=0.7 n.emob=2e27 e.char=0.027;

cbtail[3] levels=50 e.range=0.9 c.neut=0.7e-15 c.neg=0.7e-15 n.emob=1.0e28 e.char=0.080;
cbtail[4] levels=50 e.range=0.9 c.neut=0.7e-15 c.neg=0.7e-15 n.emob=1.0e28 e.char=0.080;

cbtail[5] levels=50 e.range=0.9 c.neut=0.7e-15 c.neg=0.7e-15 n.emob=1.0e26 e.char=0.010;
cbtail[6] levels=50 e.range=0.9 c.neut=0.7e-15 c.neg=0.7e-15 n.emob=1.0e28 e.char=0.080;

dbond[1] levels=40 e.corr=0.2 d.e=0.144 e.range=5.0 ce.pos=3e-14 ce.neut=3e-15
ch.neg=3e-14 ch.neut=3e-15 n=1.0e23  e.neut=-0.65;
dbond[2] levels=20 e.corr=0.2 d.e=0.2 e.range=4.0 e.rel.mg=0
ce.pos=1e-14 ce.neut=5e-14 ch.neg=5e-13 ch.neut=5e-14 n=2.0e21;

dbond[3] levels=40 e.corr=0.2 d.e=0.144 e.range=5.0 ce.pos=3e-14 ce.neut=3e-15
ch.neg=3e-14 ch.neut=3e-15 n=1.0e24 e.neut=-1.25;
dbond[4] levels=40 e.corr=0.2 d.e=0.144 e.range=5.0 ce.pos=3e-14 ce.neut=3e-15
```

```
ch.neg=3e-14 ch.neut=3e-15 n=1.0e23  e.neut=-0.65;

dbond[5] levels=40 e.corr=0.2 d.e=0.144 e.range=5.0 ce.pos=3e-14 ce.neut=3e-15
ch.neg=3e-14 ch.neut=3e-15 n=3e20 e.neut=-0.70;
dbond[6] levels=40 e.corr=0.2 d.e=0.144 e.range=5.0 ce.pos=3e-14 ce.neut=3e-15
ch.neg=3e-14 ch.neut=3e-15 n=1.0e24 e.neut=-1.25;

C GENERAL SETTINGS;

settings newton gummel.starts=4 eps.pois=1e-4 eps.cone=1e-4 eps.conh=1e-4; C update.rec;
settings max.iter=99 damp=3;
settings     max.step.reduc=0;
settings e0.fdme=2.0e7;
settings  field.lim=4e6;
settings gru.factor=3 gru.steps=10;
settings tunn.mass=0.25;
settings sr.flux=1.0e20;

model[all] tat=on;
model[all] amorphous=on;
model[3-4]      fdme=on;

C SECTION F:  SOLUTIONS : ;

solve equil;
opticgen spectrum=am15_350-1200.in gp3;
print opticgen  file=./DIRECTORY/opticgen_tandem_para$X$_para$Y$.dat;
print absorption  file=./DIRECTORY/absorption_tandem_para$X$_para$Y$.dat;
print absorptance file=./DIRECTORY/absorptance_tandem_para$X$_para$Y$.dat;
variable v_start=0.0 v_end=1.0;
solve equil;
print bands file=./DIRECTORY/bands_tandem_para$X$_para$Y$.dat gnu;
print  efield file=./DIRECTORY/efield_tandem_para$X$_para$Y$.dat gnu;

solve equil;
solve jv v.start=0.0 v.end=1.5 n.step=60 illum;
print file=./DIRECTORY/jv_illum_tandem_para$X$_para$Y$.dat;
print solpar file=./DIRECTORY/solpar_tandem_para$X$_para$Y$.dat;

solve equil;
opticgen lambda=500e-9 flux=2e20 gp3;
solve sr wl.start=300e-9 wl.end=1200e-9 wl.step=5e-9 illum;
print sr file=./DIRECTORY/EQE_bottom_tandem_tandem_para$X$_para$Y$.dat gnuplot;

solve equil;
opticgen lambda=800e-9 flux=2e20 gp3;
solve sr wl.start=300e-9 wl.end=1200e-9 wl.step=5e-9 illum;
print sr file=./DIRECTORY/EQE_top_tandem_tandem_para$X$_para$Y$.dat gnuplot;

print dos.en.complete file=./DIRECTORY/dos_tandem_para$X$_para$Y$.dat gnu;
print rec file=./DIRECTORY/recomb_tandem_para$X$_para$Y$.dat gnu;
print elec file=./DIRECTORY/elec_tandem_para$X$_para$Y$.dat gnu;
print hole file=./DIRECTORY/hole_tandem_para$X$_para$Y$.dat gnu;
print rho file=./DIRECTORY/rho_tandem_para$X$_para$Y$.dat gnu;
```

C

TRJ Thickness Optimisation Simulations

The following table contains the recorded results from ASA simulations on absorber layer thickness optimisations.

Top Absorber [nm]	Bottom Absorber [nm]	Voc (V)	Isc (mA/cm2)	Vmax (V)	Imax (mA/cm2)	Pmax (W/m2)	FF
100	1000	1.383	10.53	1.168	9.944	116.1	0.7972
100	1050	1.382	10.52	1.168	9.965	116.4	0.8007
100	1100	1.381	10.51	1.169	9.978	116.6	0.8036
100	1150	1.379	10.51	1.17	9.986	116.8	0.806
100	1200	1.378	10.5	1.17	9.991	116.9	0.8081
100	1250	1.378	10.49	1.171	9.994	117.1	0.8095
100	1300	1.377	10.48	1.172	9.995	117.1	0.8111
100	1350	1.376	10.48	1.172	9.996	117.2	0.8125
100	1400	1.375	10.47	1.172	9.996	117.2	0.8137
100	1450	1.374	10.47	1.173	9.995	117.2	0.8149
100	1500	1.373	10.46	1.173	9.995	117.2	0.816
100	1550	1.372	10.46	1.173	9.994	117.2	0.817
100	1600	1.371	10.45	1.173	9.992	117.2	0.8179
100	1650	1.37	10.45	1.173	9.991	117.2	0.8186
100	1700	1.369	10.45	1.173	9.99	117.2	0.8193
100	1750	1.368	10.44	1.173	9.988	117.1	0.82
100	1800	1.367	10.44	1.173	9.987	117.1	0.8207
100	1850	1.366	10.44	1.173	9.985	117.1	0.8213
100	1900	1.365	10.43	1.172	9.984	117	0.8218
100	1950	1.364	10.43	1.172	9.982	117	0.8223
100	2000	1.364	10.43	1.172	9.981	117	0.8227
100	2050	1.363	10.42	1.172	9.98	116.9	0.8231
100	2100	1.362	10.42	1.172	9.978	116.9	0.8235
100	2150	1.361	10.42	1.171	9.978	116.9	0.824
100	2200	1.36	10.42	1.171	9.976	116.8	0.8243
100	2250	1.36	10.41	1.171	9.974	116.8	0.8246
100	2300	1.359	10.41	1.17	9.973	116.7	0.8249
100	2350	1.358	10.41	1.17	9.972	116.7	0.8251
100	2400	1.358	10.41	1.17	9.971	116.6	0.8254
100	2450	1.357	10.41	1.17	9.969	116.6	0.8256
100	2500	1.356	10.41	1.169	9.968	116.5	0.8259
110	1000	1.382	10.64	1.16	9.998	116	0.7888
110	1050	1.38	10.79	1.158	10.07	116.6	0.7831

110	1100	1.379	10.8	1.157	10.12	117.1	0.7861
110	1150	1.378	10.8	1.157	10.16	117.5	0.7899
110	1200	1.377	10.79	1.157	10.18	117.8	0.7931
110	1250	1.377	10.78	1.158	10.2	118.1	0.7956
110	1300	1.376	10.78	1.159	10.21	118.3	0.798
110	1350	1.375	10.77	1.16	10.22	118.5	0.8001
110	1400	1.374	10.76	1.16	10.22	118.6	0.8021
110	1450	1.372	10.76	1.161	10.23	118.7	0.8038
110	1500	1.371	10.75	1.161	10.23	118.8	0.8054
110	1550	1.37	10.75	1.153	10.3	118.7	0.806
110	1600	1.369	10.75	1.156	10.27	118.7	0.8072
110	1650	1.369	10.74	1.161	10.23	118.8	0.8081
110	1700	1.367	10.74	1.162	10.22	118.8	0.8091
110	1750	1.366	10.73	1.164	10.21	118.8	0.81
110	1800	1.366	10.73	1.165	10.2	118.8	0.8109
110	1850	1.365	10.73	1.165	10.2	118.8	0.8117
110	1900	1.364	10.72	1.165	10.2	118.8	0.8124
110	1950	1.363	10.72	1.164	10.2	118.8	0.813
110	2000	1.362	10.72	1.164	10.2	118.8	0.8135
110	2050	1.361	10.71	1.163	10.21	118.7	0.8141
110	2100	1.361	10.71	1.161	10.23	118.7	0.8146
110	2150	1.36	10.71	1.161	10.22	118.7	0.815
110	2200	1.359	10.71	1.156	10.26	118.7	0.8155
110	2250	1.358	10.71	1.154	10.28	118.6	0.816
110	2300	1.358	10.7	1.151	10.31	118.6	0.8164
110	2350	1.357	10.7	1.161	10.22	118.7	0.8175
110	2400	1.356	10.7	1.161	10.22	118.7	0.8179
110	2450	1.356	10.7	1.161	10.22	118.6	0.8182
110	2500	1.355	10.7	1.16	10.22	118.6	0.8185
120	1000	1.38	10.41	1.161	9.89	114.8	0.7991
120	1050	1.379	10.56	1.156	10	115.7	0.7945
120	1100	1.378	10.7	1.153	10.1	116.5	0.7899
120	1150	1.377	10.84	1.15	10.18	117.1	0.7851
120	1200	1.376	10.97	1.149	10.25	117.7	0.7801
120	1250	1.376	11.04	1.148	10.3	118.2	0.7783
120	1300	1.374	11.04	1.147	10.34	118.6	0.7817
120	1350	1.373	11.04	1.147	10.37	118.9	0.785
120	1400	1.372	11.03	1.147	10.39	119.2	0.7878
120	1450	1.371	11.03	1.147	10.41	119.4	0.7903
120	1500	1.37	11.02	1.148	10.42	119.6	0.7926
120	1550	1.368	11.02	1.148	10.43	119.8	0.7945
120	1600	1.367	11.01	1.148	10.44	119.9	0.7963
120	1650	1.367	11.01	1.149	10.45	120	0.7977
120	1700	1.366	11	1.149	10.45	120.1	0.7991
120	1750	1.365	11	1.149	10.46	120.2	0.8004
120	1800	1.364	11	1.149	10.46	120.2	0.8015
120	1850	1.363	10.99	1.15	10.46	120.3	0.8026
120	1900	1.362	10.99	1.15	10.46	120.3	0.8036
120	1950	1.361	10.99	1.15	10.46	120.3	0.8045
120	2000	1.361	10.98	1.15	10.46	120.3	0.8052
120	2050	1.36	10.98	1.15	10.47	120.3	0.8059
120	2100	1.359	10.98	1.15	10.47	120.4	0.8066
120	2150	1.358	10.98	1.15	10.47	120.4	0.8073

120	2200	1.358	10.97	1.15	10.47	120.3	0.8079
120	2250	1.357	10.97	1.15	10.47	120.3	0.8084
120	2300	1.356	10.97	1.15	10.47	120.3	0.8089
120	2350	1.356	10.97	1.15	10.47	120.3	0.8094
120	2400	1.355	10.96	1.149	10.47	120.3	0.8098
120	2450	1.354	10.96	1.149	10.47	120.3	0.8102
120	2500	1.354	10.96	1.149	10.47	120.3	0.8106
130	1000	1.379	10.19	1.169	9.667	113	0.8043
130	1050	1.378	10.34	1.158	9.851	114.1	0.8013
130	1100	1.376	10.48	1.154	9.968	115.1	0.7976
130	1150	1.375	10.62	1.151	10.07	115.9	0.7938
130	1200	1.374	10.74	1.147	10.17	116.7	0.7901
130	1250	1.374	10.87	1.145	10.25	117.4	0.7858
130	1300	1.373	10.99	1.143	10.32	118	0.782
130	1350	1.371	11.11	1.141	10.39	118.5	0.778
130	1400	1.37	11.21	1.14	10.44	118.9	0.7741
130	1450	1.369	11.26	1.149	10.38	119.2	0.7731
130	1500	1.368	11.26	1.144	10.45	119.5	0.776
130	1550	1.367	11.26	1.141	10.5	119.8	0.7786
130	1600	1.366	11.25	1.14	10.53	120.1	0.781
130	1650	1.365	11.25	1.142	10.54	120.3	0.783
130	1700	1.364	11.25	1.143	10.54	120.5	0.785
130	1750	1.363	11.24	1.144	10.54	120.6	0.7868
130	1800	1.362	11.24	1.146	10.53	120.7	0.7884
130	1850	1.362	11.24	1.148	10.53	120.8	0.7898
130	1900	1.361	11.23	1.15	10.52	120.9	0.7912
130	1950	1.36	11.23	1.139	10.64	121.1	0.7932
130	2000	1.359	11.23	1.139	10.64	121.2	0.7942
130	2050	1.358	11.22	1.139	10.65	121.3	0.7953
130	2100	1.358	11.22	1.139	10.65	121.3	0.7962
130	2150	1.357	11.22	1.139	10.65	121.3	0.7971
130	2200	1.356	11.22	1.139	10.65	121.4	0.7979
130	2250	1.355	11.21	1.139	10.66	121.4	0.7986
130	2300	1.355	11.21	1.139	10.66	121.4	0.7993
130	2350	1.354	11.21	1.139	10.66	121.4	0.7999
130	2400	1.354	11.21	1.139	10.66	121.4	0.8004
130	2450	1.353	11.21	1.139	10.66	121.4	0.801
130	2500	1.352	11.2	1.139	10.66	121.4	0.8015
140	1000	1.377	9.988	1.164	9.556	111.3	0.8089
140	1050	1.376	10.14	1.16	9.682	112.3	0.8053
140	1100	1.375	10.28	1.156	9.806	113.4	0.8021
140	1150	1.374	10.41	1.152	9.922	114.3	0.7991
140	1200	1.373	10.54	1.148	10.03	115.2	0.7961
140	1250	1.372	10.67	1.145	10.13	116	0.7925
140	1300	1.371	10.78	1.143	10.22	116.7	0.7894
140	1350	1.37	10.9	1.14	10.3	117.4	0.7863
140	1400	1.369	11.01	1.139	10.35	117.8	0.7822
140	1450	1.367	11.11	1.135	10.44	118.5	0.7795
140	1500	1.366	11.22	1.133	10.5	118.9	0.7761
140	1550	1.365	11.31	1.131	10.55	119.4	0.7727
140	1600	1.364	11.41	1.13	10.6	119.7	0.7693
140	1650	1.364	11.47	1.129	10.64	120.1	0.7679
140	1700	1.363	11.47	1.128	10.67	120.4	0.7702

140	1750	1.362	11.47	1.128	10.7	120.6	0.7725
140	1800	1.361	11.46	1.127	10.72	120.9	0.7746
140	1850	1.36	11.46	1.127	10.74	121	0.7766
140	1900	1.359	11.46	1.127	10.75	121.2	0.7784
140	1950	1.358	11.45	1.127	10.77	121.4	0.78
140	2000	1.358	11.45	1.127	10.78	121.5	0.7814
140	2050	1.357	11.45	1.127	10.79	121.6	0.7827
140	2100	1.356	11.45	1.127	10.8	121.7	0.784
140	2150	1.356	11.44	1.127	10.8	121.8	0.7852
140	2200	1.355	11.44	1.127	10.81	121.9	0.7862
140	2250	1.354	11.44	1.127	10.81	121.9	0.7871
140	2300	1.353	11.44	1.127	10.82	122	0.788
140	2350	1.353	11.43	1.127	10.82	122	0.7888
140	2400	1.352	11.43	1.127	10.83	122	0.7895
140	2450	1.352	11.43	1.127	10.83	122.1	0.7903
140	2500	1.351	11.43	1.127	10.83	122.1	0.7909
150	1000	1.376	9.807	1.165	9.395	109.5	0.8112
150	1050	1.375	9.953	1.154	9.577	110.5	0.8072
150	1100	1.374	10.09	1.157	9.647	111.6	0.8052
150	1150	1.372	10.23	1.153	9.766	112.6	0.8025
150	1200	1.371	10.35	1.15	9.877	113.5	0.7998
150	1250	1.371	10.48	1.146	9.982	114.4	0.7967
150	1300	1.37	10.6	1.143	10.08	115.2	0.794
150	1350	1.368	10.71	1.141	10.17	116	0.7913
150	1400	1.367	10.82	1.142	10.2	116.5	0.7877
150	1450	1.366	10.92	1.135	10.33	117.2	0.7855
150	1500	1.365	11.03	1.132	10.4	117.8	0.7827
150	1550	1.364	11.12	1.13	10.47	118.3	0.7799
150	1600	1.363	11.22	1.127	10.54	118.8	0.777
150	1650	1.362	11.31	1.126	10.6	119.3	0.7738
150	1700	1.361	11.4	1.124	10.65	119.7	0.7709
150	1750	1.361	11.49	1.123	10.69	120	0.7679
150	1800	1.36	11.57	1.121	10.73	120.3	0.7649
150	1850	1.359	11.64	1.12	10.77	120.6	0.7625
150	1900	1.358	11.66	1.12	10.8	120.9	0.7636
150	1950	1.357	11.66	1.119	10.82	121.1	0.7656
150	2000	1.357	11.65	1.119	10.85	121.3	0.7673
150	2050	1.356	11.65	1.118	10.86	121.5	0.7691
150	2100	1.355	11.65	1.118	10.88	121.7	0.7707
150	2150	1.354	11.65	1.118	10.89	121.8	0.7722
150	2200	1.354	11.65	1.118	10.91	121.9	0.7735
150	2250	1.353	11.64	1.118	10.92	122	0.7748
150	2300	1.352	11.64	1.117	10.93	122.1	0.7759
150	2350	1.352	11.64	1.117	10.94	122.2	0.7769
150	2400	1.351	11.64	1.117	10.95	122.3	0.7779
150	2450	1.35	11.63	1.117	10.95	122.4	0.7789
150	2500	1.35	11.63	1.117	10.96	122.4	0.7798
160	1000	1.375	9.645	1.166	9.247	107.8	0.8127
160	1050	1.374	9.79	1.159	9.388	108.8	0.809
160	1100	1.372	9.929	1.158	9.5	110	0.8072
160	1150	1.371	10.06	1.154	9.621	111	0.8047
160	1200	1.37	10.19	1.15	9.733	112	0.8023
160	1250	1.369	10.31	1.147	9.841	112.9	0.7994

160	1300	1.368	10.43	1.144	9.94	113.7	0.7969
160	1350	1.367	10.54	1.141	10.03	114.5	0.7945
160	1400	1.366	10.65	1.149	10.02	115.1	0.7912
160	1450	1.365	10.76	1.136	10.2	115.9	0.7893
160	1500	1.364	10.86	1.133	10.29	116.5	0.7869
160	1550	1.363	10.95	1.13	10.36	117.1	0.7844
160	1600	1.362	11.05	1.127	10.43	117.6	0.7819
160	1650	1.361	11.14	1.125	10.5	118.2	0.7791
160	1700	1.36	11.23	1.123	10.56	118.6	0.7765
160	1750	1.359	11.32	1.121	10.62	119.1	0.774
160	1800	1.358	11.4	1.119	10.67	119.5	0.7714
160	1850	1.358	11.48	1.118	10.72	119.8	0.7687
160	1900	1.357	11.56	1.116	10.76	120.1	0.7661
160	1950	1.356	11.64	1.115	10.8	120.5	0.7634
160	2000	1.355	11.71	1.125	10.72	120.6	0.76
160	2050	1.355	11.78	1.118	10.82	120.9	0.7574
160	2100	1.354	11.83	1.111	10.9	121.1	0.7563
160	2150	1.353	11.83	1.107	10.96	121.3	0.7577
160	2200	1.352	11.83	1.102	11.03	121.5	0.7593
160	2250	1.352	11.83	1.11	10.97	121.7	0.7613
160	2300	1.351	11.83	1.11	10.98	121.9	0.7627
160	2350	1.351	11.83	1.109	11	122	0.764
160	2400	1.35	11.82	1.109	11.01	122.1	0.7653
160	2450	1.349	11.82	1.109	11.03	122.2	0.7665
160	2500	1.348	11.82	1.108	11.04	122.3	0.7677
170	1100	1.371	9.782	1.158	9.365	108.4	0.8086
170	1150	1.37	9.914	1.154	9.487	109.5	0.8063
170	1200	1.368	10.04	1.151	9.601	110.5	0.8039
170	1250	1.368	10.16	1.147	9.709	111.4	0.8012
170	1300	1.367	10.28	1.144	9.81	112.3	0.7989
170	1350	1.366	10.39	1.142	9.905	113.1	0.7967
170	1400	1.365	10.5	1.139	9.994	113.8	0.7944
170	1450	1.364	10.61	1.127	10.16	114.4	0.7912
170	1500	1.362	10.71	1.133	10.16	115.2	0.7896
170	1550	1.361	10.8	1.13	10.25	115.8	0.7873
170	1600	1.361	10.9	1.128	10.32	116.4	0.785
170	1650	1.36	10.99	1.125	10.4	117	0.7825
170	1700	1.359	11.08	1.123	10.46	117.5	0.7802
170	1750	1.358	11.16	1.121	10.53	117.9	0.7779
170	1800	1.357	11.25	1.119	10.58	118.4	0.7756
170	1850	1.356	11.33	1.117	10.64	118.8	0.7732
170	1900	1.356	11.41	1.115	10.69	119.2	0.7709
170	1950	1.355	11.48	1.12	10.67	119.4	0.7678
170	2000	1.354	11.56	1.108	10.81	119.8	0.7653
170	2050	1.354	11.63	1.11	10.83	120.2	0.7634
170	2100	1.353	11.7	1.109	10.87	120.5	0.761
170	2150	1.352	11.77	1.107	10.9	120.7	0.7586
170	2200	1.351	11.84	1.106	10.94	121	0.7562
170	2250	1.351	11.9	1.105	10.97	121.2	0.7538
170	2300	1.35	11.96	1.104	10.99	121.4	0.7517
170	2350	1.349	11.99	1.103	11.02	121.6	0.7513
170	2400	1.349	11.99	1.103	11.04	121.7	0.7526
170	2450	1.348	11.99	1.102	11.06	121.9	0.7539

170	2500	1.347	11.99	1.101	11.08	122	0.7553
180	1000	1.372	9.368	1.165	8.989	104.8	0.8148
180	1050	1.371	9.512	1.159	9.127	105.8	0.8112
180	1200	1.367	9.907	1.151	9.479	109.1	0.8051
180	1250	1.367	10.03	1.148	9.588	110	0.8024
180	1300	1.366	10.15	1.145	9.689	110.9	0.8003
180	1350	1.365	10.26	1.142	9.785	111.7	0.7981
180	1400	1.364	10.37	1.139	9.876	112.5	0.796
180	1450	1.362	10.47	1.128	10.02	113.1	0.7929
180	1500	1.361	10.57	1.133	10.05	113.9	0.7914
180	1550	1.36	10.67	1.13	10.13	114.5	0.7893
180	1600	1.359	10.76	1.128	10.21	115.1	0.7871
180	1650	1.359	10.85	1.125	10.29	115.7	0.7848
180	1700	1.358	10.94	1.123	10.36	116.3	0.7827
180	1750	1.357	11.03	1.121	10.42	116.8	0.7805
180	1800	1.356	11.11	1.118	10.49	117.3	0.7784
180	1850	1.355	11.19	1.116	10.55	117.7	0.7763
180	1900	1.355	11.27	1.115	10.6	118.2	0.7741
180	1950	1.354	11.34	1.115	10.62	118.4	0.7712
180	2000	1.353	11.42	1.101	10.79	118.8	0.7689
180	2050	1.353	11.49	1.109	10.75	119.3	0.7672
180	2100	1.352	11.56	1.107	10.8	119.6	0.7651
180	2150	1.351	11.63	1.105	10.84	119.9	0.7629
180	2200	1.35	11.7	1.104	10.89	120.2	0.7607
180	2250	1.35	11.76	1.102	10.92	120.4	0.7585
180	2300	1.349	11.83	1.101	10.96	120.7	0.7565
180	2350	1.348	11.89	1.1	10.99	120.9	0.7542
180	2400	1.347	11.95	1.099	11.02	121.1	0.7521
180	2450	1.347	12.01	1.098	11.05	121.3	0.7501
180	2500	1.346	12.07	1.097	11.07	121.5	0.748
190	1000	1.371	9.246	1.165	8.874	103.4	0.8155
190	1050	1.37	9.39	1.156	9.032	104.4	0.8119
190	1100	1.369	9.527	1.158	9.128	105.7	0.8104
190	1250	1.366	9.906	1.147	9.474	108.7	0.8034
190	1300	1.365	10.02	1.145	9.576	109.6	0.8013
190	1350	1.364	10.13	1.142	9.673	110.4	0.7992
190	1400	1.363	10.24	1.139	9.764	111.2	0.7971
190	1450	1.361	10.34	1.128	9.911	111.8	0.7941
190	1500	1.36	10.44	1.133	9.939	112.6	0.7927
190	1550	1.359	10.54	1.13	10.02	113.3	0.7907
190	1600	1.359	10.63	1.128	10.1	113.9	0.7887
190	1650	1.358	10.73	1.125	10.18	114.6	0.7864
190	1700	1.357	10.81	1.123	10.25	115.1	0.7844
190	1750	1.356	10.9	1.121	10.32	115.7	0.7824
190	1800	1.355	10.98	1.118	10.39	116.2	0.7804
190	1850	1.355	11.06	1.116	10.45	116.6	0.7784
190	1900	1.354	11.14	1.114	10.51	117.1	0.7763
190	1950	1.353	11.22	1.113	10.55	117.4	0.7735
190	2000	1.352	11.29	1.11	10.62	117.9	0.7719
190	2050	1.352	11.36	1.108	10.67	118.3	0.7699
190	2100	1.351	11.43	1.106	10.72	118.6	0.7679
190	2150	1.35	11.5	1.105	10.77	118.9	0.7658
190	2200	1.349	11.57	1.103	10.82	119.3	0.7639

190	2250	1.349	11.64	1.101	10.86	119.6	0.762
190	2300	1.348	11.7	1.1	10.9	119.8	0.7601
190	2350	1.347	11.76	1.098	10.94	120.1	0.758
190	2400	1.346	11.82	1.097	10.97	120.3	0.7561
190	2450	1.345	11.88	1.096	11	120.6	0.7541
190	2500	1.345	11.94	1.094	11.03	120.8	0.7522
200	1000	1.37	9.132	1.165	8.766	102.1	0.816
200	1050	1.369	9.275	1.153	8.949	103.2	0.8124
200	1100	1.368	9.412	1.157	9.02	104.4	0.811
200	1150	1.366	9.543	1.154	9.142	105.5	0.8088
200	1300	1.364	9.905	1.144	9.468	108.4	0.8021
200	1350	1.363	10.02	1.142	9.566	109.2	0.8
200	1400	1.362	10.12	1.139	9.657	110	0.798
200	1450	1.361	10.23	1.127	9.812	110.6	0.795
200	1500	1.36	10.33	1.133	9.834	111.4	0.7937
200	1550	1.359	10.42	1.13	9.919	112.1	0.7917
200	1600	1.358	10.52	1.128	10	112.8	0.7898
200	1650	1.357	10.61	1.125	10.08	113.4	0.7876
200	1700	1.356	10.7	1.123	10.15	114	0.7857
200	1750	1.355	10.78	1.121	10.22	114.5	0.7838
200	1800	1.355	10.87	1.118	10.29	115.1	0.7818
200	1850	1.354	10.94	1.116	10.35	115.6	0.7799
200	1900	1.353	11.02	1.114	10.41	116	0.778
200	1950	1.352	11.1	1.112	10.46	116.3	0.7752
200	2000	1.352	11.17	1.11	10.53	116.9	0.7738
200	2050	1.351	11.25	1.108	10.58	117.3	0.7718
200	2100	1.35	11.32	1.106	10.64	117.6	0.7699
200	2150	1.349	11.38	1.104	10.69	118	0.7681
200	2200	1.348	11.45	1.102	10.74	118.3	0.7663
200	2250	1.348	11.52	1.1	10.78	118.6	0.7645
200	2300	1.347	11.58	1.099	10.82	118.9	0.7627
200	2350	1.346	11.64	1.097	10.87	119.2	0.7607
200	2400	1.345	11.7	1.096	10.91	119.5	0.7589
200	2450	1.345	11.76	1.094	10.94	119.7	0.7571
200	2500	1.344	11.82	1.093	10.98	120	0.7553
210	1000	1.369	9.024	1.165	8.663	100.9	0.8164
210	1100	1.367	9.304	1.157	8.919	103.2	0.8114
210	1200	1.364	9.559	1.15	9.155	105.3	0.8072
210	1400	1.361	10.01	1.139	9.556	108.8	0.7987
210	1500	1.359	10.22	1.133	9.734	110.3	0.7945
210	1600	1.357	10.41	1.128	9.901	111.6	0.7906
210	1700	1.355	10.59	1.123	10.05	112.9	0.7867
210	1800	1.354	10.75	1.118	10.19	114	0.7829
210	1900	1.352	10.91	1.114	10.32	115	0.7792
210	2000	1.351	11.06	1.11	10.44	115.8	0.7751
210	2100	1.349	11.21	1.106	10.55	116.6	0.7715
210	2200	1.347	11.34	1.102	10.65	117.4	0.7681
210	2300	1.346	11.47	1.098	10.75	118	0.7646
210	2400	1.344	11.59	1.095	10.83	118.6	0.761
210	2500	1.343	11.71	1.092	10.91	119.1	0.7576
220	1000	1.369	8.922	1.164	8.565	99.73	0.8168
220	1100	1.366	9.2	1.157	8.821	102	0.8118
220	1200	1.364	9.455	1.15	9.057	104.1	0.8076

220	1300	1.362	9.691	1.144	9.269	106	0.8032
220	1400	1.36	9.91	1.139	9.459	107.7	0.7992
220	1500	1.358	10.11	1.133	9.638	109.2	0.7951
220	1600	1.356	10.3	1.127	9.806	110.5	0.7913
220	1700	1.355	10.48	1.123	9.96	111.8	0.7874
220	1800	1.353	10.65	1.118	10.1	112.9	0.7838
220	1900	1.351	10.81	1.114	10.23	113.9	0.7801
220	2000	1.35	10.96	1.11	10.35	114.8	0.7762
220	2100	1.348	11.1	1.105	10.46	115.7	0.7728
220	2200	1.347	11.23	1.102	10.57	116.4	0.7695
220	2300	1.345	11.36	1.098	10.66	117.1	0.7661
220	2400	1.344	11.49	1.095	10.75	117.7	0.7627
220	2500	1.342	11.6	1.092	10.83	118.3	0.7593
230	1000	1.368	8.823	1.164	8.47	98.6	0.8171
230	1100	1.365	9.1	1.156	8.726	100.9	0.8122
230	1200	1.363	9.354	1.149	8.962	103	0.808
230	1300	1.361	9.59	1.144	9.174	104.9	0.8036
230	1400	1.359	9.808	1.139	9.364	106.6	0.7997
230	1500	1.357	10.01	1.133	9.544	108.1	0.7956
230	1600	1.355	10.2	1.127	9.712	109.5	0.7919
230	1700	1.354	10.38	1.122	9.866	110.7	0.7881
230	1800	1.352	10.55	1.118	10.01	111.9	0.7845
230	1900	1.351	10.7	1.114	10.14	112.9	0.7809
230	2000	1.349	10.85	1.11	10.26	113.8	0.7771
230	2100	1.348	11	1.105	10.37	114.7	0.7739
230	2200	1.346	11.13	1.101	10.48	115.4	0.7706
230	2300	1.344	11.26	1.098	10.58	116.1	0.7674
230	2400	1.343	11.38	1.094	10.67	116.8	0.764
230	2500	1.341	11.5	1.091	10.75	117.4	0.7608
240	1000	1.367	8.726	1.164	8.378	97.5	0.8174
240	1100	1.364	9.003	1.156	8.634	99.81	0.8125
240	1200	1.362	9.256	1.149	8.869	101.9	0.8084
240	1300	1.361	9.491	1.143	9.081	103.8	0.804
240	1600	1.355	10.1	1.127	9.62	108.4	0.7924
240	1700	1.353	10.28	1.122	9.774	109.7	0.7887
240	1800	1.352	10.45	1.118	9.916	110.8	0.7851
240	1900	1.35	10.6	1.114	10.04	111.9	0.7816
240	2000	1.349	10.75	1.11	10.17	112.8	0.778
240	2100	1.347	10.89	1.105	10.29	113.7	0.7748
240	2200	1.345	11.03	1.101	10.4	114.5	0.7716
240	2300	1.343	11.16	1.098	10.49	115.2	0.7684
240	2400	1.342	11.28	1.094	10.59	115.8	0.7651
240	2500	1.341	11.4	1.091	10.67	116.4	0.762
250	1000	1.366	8.632	1.164	8.288	96.43	0.8177
250	1100	1.364	8.908	1.156	8.544	98.74	0.8128
250	1200	1.361	9.161	1.149	8.779	100.9	0.8087
250	1300	1.36	9.395	1.143	8.99	102.8	0.8044
250	1400	1.358	9.611	1.146	9.103	104.3	0.7995
250	1500	1.356	9.813	1.132	9.36	106	0.7965
250	1600	1.354	10	1.127	9.529	107.4	0.7929
250	1700	1.353	10.18	1.122	9.684	108.7	0.7892
250	1800	1.351	10.35	1.118	9.826	109.8	0.7857
250	1900	1.349	10.5	1.114	9.955	110.9	0.7823

250	2000	1.348	10.65	1.109	10.08	111.8	0.7787
250	2100	1.346	10.8	1.105	10.2	112.7	0.7756
250	2200	1.344	10.93	1.101	10.31	113.5	0.7724
250	2300	1.343	11.06	1.097	10.41	114.2	0.7693
250	2400	1.341	11.18	1.094	10.5	114.9	0.7661
250	2500	1.34	11.3	1.091	10.59	115.5	0.763
260	1000	1.366	8.542	1.174	8.113	95.27	0.8168
260	1100	1.363	8.817	1.155	8.458	97.72	0.8131
260	1200	1.361	9.069	1.149	8.692	99.84	0.809
260	1300	1.359	9.303	1.143	8.902	101.8	0.8047
260	1400	1.357	9.518	1.144	9.029	103.3	0.7998
260	1500	1.355	9.719	1.132	9.273	105	0.7969
260	1600	1.353	9.907	1.127	9.441	106.4	0.7933
260	1700	1.352	10.08	1.122	9.596	107.7	0.7896
260	1800	1.351	10.25	1.118	9.738	108.8	0.7862
260	1900	1.349	10.41	1.114	9.868	109.9	0.7829
260	2000	1.347	10.56	1.109	9.992	110.8	0.7793
260	2100	1.345	10.7	1.105	10.11	111.7	0.7762
260	2200	1.344	10.83	1.101	10.22	112.6	0.7732
260	2300	1.342	10.96	1.097	10.32	113.3	0.7701
260	2400	1.341	11.08	1.094	10.42	114	0.7669
260	2500	1.339	11.2	1.091	10.51	114.6	0.7639
270	1000	1.365	8.457	1.171	8.052	94.3	0.817
270	1100	1.362	8.731	1.155	8.376	96.75	0.8134
270	1200	1.36	8.981	1.148	8.609	98.87	0.8093
270	1300	1.359	9.214	1.143	8.819	100.8	0.805
270	1400	1.357	9.429	1.143	8.959	102.4	0.8001
270	1600	1.353	9.817	1.127	9.357	105.4	0.7937
270	1700	1.352	9.994	1.122	9.512	106.7	0.79
270	1800	1.35	10.16	1.118	9.654	107.9	0.7866
270	1900	1.348	10.32	1.124	9.68	108.8	0.7826
270	2000	1.346	10.47	1.109	9.909	109.9	0.7799
270	2100	1.345	10.61	1.105	10.03	110.8	0.7769
270	2200	1.343	10.74	1.101	10.14	111.6	0.7738
270	2300	1.341	10.87	1.097	10.24	112.4	0.7708
270	2400	1.34	10.99	1.094	10.34	113.1	0.7677
270	2500	1.339	11.11	1.091	10.43	113.7	0.7647
280	1000	1.364	8.374	1.168	7.992	93.36	0.8172
280	1100	1.362	8.647	1.155	8.296	95.81	0.8136
280	1200	1.36	8.897	1.148	8.528	97.92	0.8096
280	1300	1.358	9.129	1.143	8.737	99.84	0.8053
280	1400	1.356	9.343	1.141	8.888	101.4	0.8004
280	1500	1.354	9.543	1.132	9.106	103.1	0.7976
280	1600	1.352	9.729	1.126	9.275	104.5	0.794
280	1700	1.351	9.906	1.122	9.43	105.8	0.7904
280	1800	1.349	10.07	1.117	9.572	107	0.7871
280	1900	1.347	10.23	1.124	9.603	107.9	0.7831
280	2000	1.346	10.38	1.109	9.827	109	0.7805
280	2100	1.344	10.52	1.105	9.948	109.9	0.7774
280	2200	1.342	10.65	1.101	10.06	110.7	0.7744
280	2300	1.341	10.78	1.097	10.16	111.5	0.7714
280	2400	1.34	10.9	1.094	10.26	112.2	0.7683
280	2500	1.338	11.02	1.091	10.35	112.8	0.7653

290	1000	1.364	8.295	1.165	7.934	92.46	0.8174
290	1100	1.361	8.566	1.155	8.219	94.9	0.8139
290	1200	1.359	8.815	1.148	8.451	97.02	0.8098
290	1300	1.358	9.046	1.143	8.659	98.94	0.8056
290	1400	1.356	9.26	1.139	8.82	100.5	0.8007
290	1500	1.354	9.459	1.132	9.027	102.2	0.7979
290	1600	1.352	9.645	1.126	9.196	103.6	0.7944
290	1700	1.351	9.821	1.122	9.351	104.9	0.7907
290	1800	1.349	9.986	1.117	9.492	106.1	0.7875
290	1900	1.347	10.14	1.123	9.529	107	0.7836
290	2000	1.345	10.29	1.109	9.748	108.1	0.7809
290	2100	1.344	10.43	1.105	9.869	109	0.7779
290	2200	1.342	10.56	1.101	9.98	109.9	0.7749
290	2300	1.34	10.69	1.097	10.08	110.6	0.772
290	2400	1.339	10.81	1.094	10.18	111.3	0.7689
290	2500	1.338	10.93	1.091	10.27	112	0.766
300	1000	1.363	8.22	1.163	7.879	91.61	0.8176
300	1100	1.361	8.49	1.154	8.147	94.06	0.8141
300	1200	1.359	8.738	1.148	8.378	96.17	0.81
300	1300	1.357	8.969	1.142	8.586	98.09	0.8058
300	1400	1.355	9.182	1.138	8.758	99.66	0.801
300	1600	1.351	9.566	1.126	9.122	102.7	0.7946
300	1700	1.35	9.741	1.122	9.276	104	0.791
300	1800	1.348	9.906	1.117	9.418	105.2	0.7879
300	1900	1.346	10.06	1.122	9.46	106.2	0.7839
300	2000	1.345	10.21	1.109	9.673	107.3	0.7814
300	2100	1.343	10.35	1.105	9.794	108.2	0.7784
300	2200	1.341	10.48	1.101	9.906	109	0.7754
300	2300	1.34	10.61	1.097	10.01	109.8	0.7725
300	2400	1.338	10.73	1.094	10.11	110.5	0.7694
300	2500	1.337	10.85	1.09	10.2	111.2	0.7665

D

TRJ Doping Simulations

The following table contains the recorded results from ASA simulations on TRJ dopings. The zeros represents the executed solutions did not converge

N-TRJ Ea	P-TRJ Ea	Voc [V]	Isc (A/m2)	Vmax (V)	Imax (A/m2)	Pmax (W/m2)	FF
0.1	0.1	0	0	0	0	0	0
0.1	0.15	0	0	0	0	0	0
0.1	0.2	0	0	0	0	0	0
0.1	0.25	0	0	0	0	0	0
0.1	0.3	0	0	0	0	0	0
0.1	0.35	0	0	0	0	0	0
0.1	0.4	0.6426	-116.4	0.3799	-101.7	38.62	0.5162
0.1	0.45	0	0	0	0	0	0
0.1	0.5	0.8259	-116.9	0.5928	-106	62.83	0.6509
0.15	0.1	0.1526	-117.5	0.1379	-294.2	40.56	2.262
0.15	0.15	1.353	-117.5	1.124	-106.8	120	0.755
0.15	0.2	0	0	0	0	0	0
0.15	0.25	0	0	0	0	0	0
0.15	0.3	1.334	-117.2	0.774	-102.4	79.28	0.5069
0.15	0.35	0.9342	-116.5	0.3007	-95.9	28.84	0.2651
0.15	0.4	0.6202	-116.8	0.3667	-101.2	37.12	0.5126
0.15	0.45	0.7414	-117	0.4563	-103.7	47.3	0.5455
0.15	0.5	0.8216	-117.1	0.5664	-105.7	59.87	0.622
0.2	0.1	0	0	0	0	0	0
0.2	0.15	1.354	-117.6	1.118	-108.3	121.1	0.761
0.2	0.2	1.356	-117.6	1.115	-108.3	120.7	0.7571
0.2	0.25	1.332	-117.5	0.8527	-104.7	89.3	0.5709
0.2	0.3	1.277	-116.8	0.2892	-84.52	24.44	0.1639
0.2	0.35	0	0	0	0	0	0
0.2	0.4	0	0	0	0	0	0
0.2	0.45	0	0	0	0	0	0
0.2	0.5	0	0	0	0	0	0
0.25	0.1	1.355	-117.5	1.117	-109.1	121.8	0.7657
0.25	0.15	1.355	-117.5	1.117	-109.1	121.9	0.7662
0.25	0.2	1.357	-117.6	1.117	-109.2	121.9	0.7643
0.25	0.25	1.356	-117.6	1.075	-108.6	116.8	0.7324
0.25	0.3	1.062	-118.6	0.3208	-87.39	28.03	0.2225
0.25	0.35	0	0	0	0	0	0
0.25	0.4	0	0	0	0	0	0
0.25	0.45	0	0	0	0	0	0
0.25	0.5	0	0	0	0	0	0

0.3	0.1	1.35	-117.1	0.9607	-106.9	102.7	0.6495
0.3	0.15	1.349	-117.2	0.9721	-107.2	104.2	0.6589
0.3	0.2	1.353	-117.3	1.002	-107.5	107.7	0.6786
0.3	0.25	1.351	-117.4	0.9679	-106.9	103.5	0.6529
0.3	0.3	1.274	-119.1	0.3726	-88.81	33.09	0.2182
0.3	0.35	0	0	0	0	0	0
0.3	0.4	0	0	0	0	0	0
0.3	0.45	0	0	0	0	0	0
0.3	0.5	0	0	0	0	0	0
0.35	0.1	0.9496	-116.8	0.6426	-101.2	65.03	0.5861
0.35	0.15	0.9567	-116.9	0.6334	-100.7	63.8	0.5705
0.35	0.2	0	0	0	0	0	0
0.35	0.25	0.9401	-117.1	0.5706	-96.66	55.16	0.5011
0.35	0.3	0.8405	-119.5	0.3902	-90.93	35.48	0.3534
0.35	0.35	0	0	0	0	0	0
0.35	0.4	0	0	0	0	0	0
0.35	0.45	0	0	0	0	0	0
0.35	0.5	0	0	0	0	0	0
0.4	0.1	0.6935	-117	0.4735	-93.93	44.48	0.5481
0.4	0.15	0	0	0	0	0	0
0.4	0.2	0	0	0	0	0	0
0.4	0.25	0	0	0	0	0	0
0.4	0.3	0	0	0	0	0	0
0.4	0.35	0.5783	-120.4	0.3447	-97.83	33.72	0.4844
0.4	0.4	0	0	0	0	0	0
0.4	0.45	0	0	0	0	0	0
0.4	0.5	0	0	0	0	0	0
0.45	0.1	0.6006	-119.3	0.3948	-94.83	37.44	0.5224
0.45	0.15	0	0	0	0	0	0
0.45	0.2	0	0	0	0	0	0
0.45	0.25	0	0	0	0	0	0
0.45	0.3	0	0	0	0	0	0
0.45	0.35	0.5584	-120.1	0.3456	-99.72	34.46	0.5139
0.45	0.4	0.545	-122.2	0.331	-98.87	32.73	0.4914
0.45	0.45	0	0	0	0	0	0
0.45	0.5	0	0	0	0	0	0
0.5	0.1	0.5636	-119.4	0.3684	-97.92	36.08	0.5362
0.5	0.15	0.5564	-119.4	0.3621	-98.56	35.68	0.5372
0.5	0.2	0	0	0	0	0	0
0.5	0.25	0.552	-119.6	0.3546	-99.7	35.35	0.5357
0.5	0.3	0.548	-119.7	0.3501	-100.4	35.14	0.5356
0.5	0.35	0	0	0	0	0	0
0.5	0.4	0.5386	-121.2	0.3269	-100.9	32.97	0.5051
0.5	0.45	0.549	-136.9	0.2499	-85.46	21.35	0.2842
0.5	0.5	0	0	0	0	0	0

E

Light soaking : Curve Fit data

K and A values for fit

98 different combinations of K and A were tried to fit the curve. The curves modelled are as follows and the legend to the curve is given in the next page.

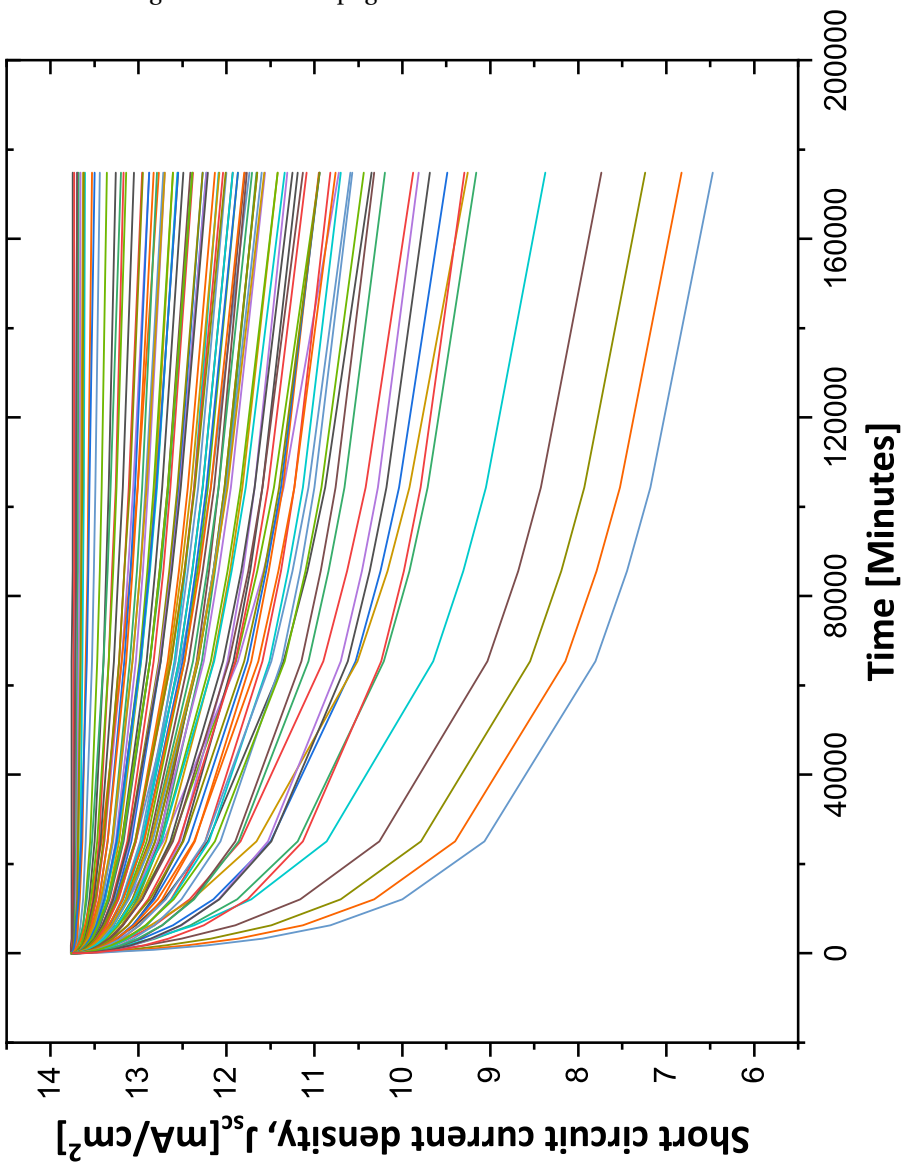

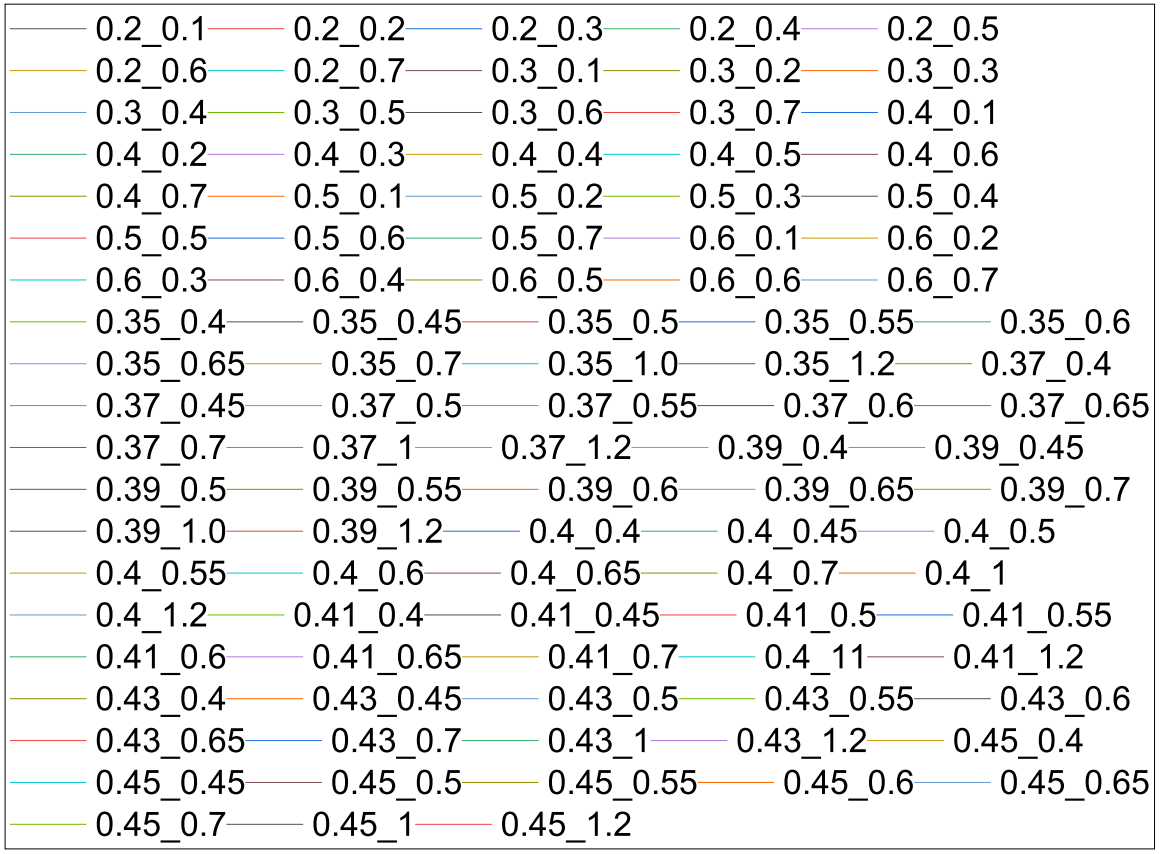
0.2_0.1
0.2_0.2
0.2_0.3
0.2_0.4
0.2_0.5
0.2_0.6
0.2_0.7
0.3_0.1
0.3_0.2
0.3_0.3
0.3_0.4
0.3_0.5
0.3_0.6
0.3_0.7
0.4_0.1
0.4_0.2
0.4_0.3
0.4_0.4
0.4_0.5
0.4_0.6
0.4_0.7
0.5_0.1
0.5_0.2
0.5_0.3
0.5_0.4
0.5_0.5
0.5_0.6
0.5_0.7
0.6_0.1
0.6_0.2
0.6_0.3
0.6_0.4
0.6_0.5
0.6_0.6
0.6_0.7
0.35_0.4
0.35_0.45
0.35_0.5
0.35_0.55
0.35_0.6
0.35_0.65
0.35_0.7
0.35_1.0
0.35_1.2
0.37_0.4
0.37_0.45
0.37_0.5
0.37_0.55
0.37_0.6
0.37_0.65
0.37_0.7
0.37_1
0.37_1.2
0.39_0.4
0.39_0.45
0.39_0.5
0.39_0.55
0.39_0.6
0.39_0.65
0.39_0.7
0.39_1.0
0.39_1.2
0.4_0.4
0.4_0.45
0.4_0.5
0.4_0.55
0.4_0.6
0.4_0.65
0.4_0.7
0.4_1
0.4_1.2
0.41_0.4
0.41_0.45
0.41_0.5
0.41_0.55
0.41_0.6
0.41_0.65
0.41_0.7
0.4_11
0.41_1.2
0.43_0.4
0.43_0.45
0.43_0.5
0.43_0.55
0.43_0.6
0.43_0.65
0.43_0.7
0.43_1
0.43_1.2
0.45_0.4
0.45_0.45
0.45_0.5
0.45_0.55
0.45_0.6
0.45_0.65
0.45_0.7
0.45_1
0.45_1.2

F

TRJ Fabrication

The table below represents the illuminated measurements data of fabricated tandem solar cells. The table shows the best cell performance only.

Sample	N_TRJ	P_TRJ	Voc (V)	Jsc (mA/cm2)	FF	Eff. (%)	Rsc (k cm2)	Roc (k cm2)	Vmpp (V)	Jmpp (mA/cm2)	Remark
S30	10	10	1.077	8.78	0.471	5.7	0.57	39.78	0.697	-6.39	C3
S31	10	15	0.95	10.09	0.402	3.86	0.34	39.18	0.592	-6.52	C2
S32	10	20	1.089	7.47	0.520	4.24	0.53	73.23	0.712	-5.6	C5
S33	10	25	0	0	0	0	0	0	0	0	NA
S34	10	30	0	0	0	0	0	0	0	0	NA
S35	15	10	0	0	0	0	0	0	0	0	NA
S36	15	15	0	0	0	0	0	0	0	0	NA
S37	15	20	1.080	9.10	0.498	4.94	0.27	73.72	0.712	-6.8	C6
S38	15	25	1.105	9.44	0.519	5.41	0.64	51.55	0.744	-7.27	C5
S39	15	30	1.098	9.21	0.537	5.43	0.20	77.70	0.744	-7.3	C7
S40	15	30	1.070	7.26	0.557	4.36	0.27	27.38	0.744	-7.3	C7
S41	20	15	1.021	7.42	0.594	4.5	0.95	26.89	0.729	-6.17	C5
S42	20	20	1.137	9.24	0.541	5.69	0.64	28.21	0.793	-7.18	C7
S43	20	25	1.179	8.5	0.591	5.93	1.31	27.86	0.823	-7.2	C8
S44	20	30	1.058	9.02	0.494	4.71	0.41	29.12	0.728	-6.47	C6
S45	25	10	0.993	9.77	0.471	4.57	0.46	27.79	0.672	-6.79	C8
S46	25	15	1.168	9.45	0.564	6.23	0.34	23.13	0.846	-7.36	C6
S47	25	20	1.186	9	0.622	6.64	0.47	20.97	0.887	-7.49	C3

G

Refractive index graphs of the used layers in modelling

The refractive index graphs for all the layers used in micromorph tandem base model is given in the graph below.

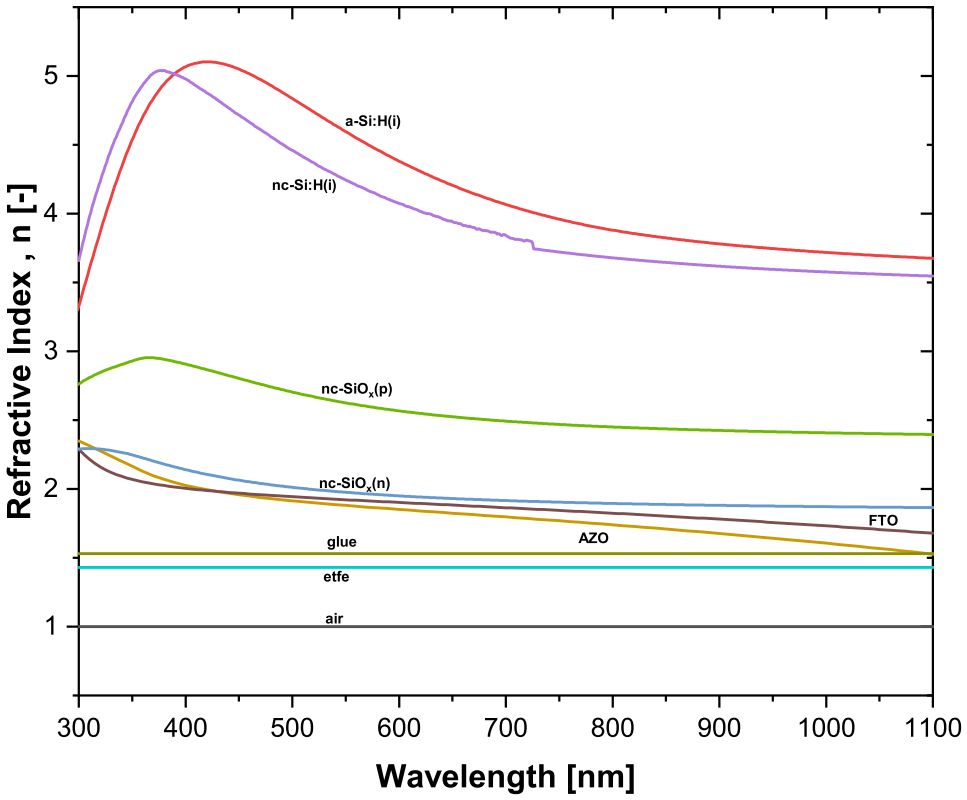

Figure G.1: Refractive index graphs for all layers for modelling.